

Cell Mechanics and Adhesion: Cell Blebbing and Malaria Parasite Invasion

Inaugural-Dissertation
zur
Erlangung des Doktorgrades
der Mathematisch-Naturwissenschaftlichen Fakultät
der Universität zu Köln

vorgelegt von

Sebastian Hillringhaus geborener Sohn
aus Schwerte

Köln, 2019

1. Berichtstatter: PD. Dr. Dmitry A. Fedosov
2. Berichtstatter: Prof. Dr. Johannes Berg

Tag der mündlichen Prüfung: 29.04.2019

Für Bettina

Abstract

Cell mechanics and adhesion play an important role in biological systems. We focus on two examples in this thesis, stress-induced cell blebbing and red blood cell deformation during the invasion by malaria parasites. To investigate both processes, simulation models are employed and their dependence on various parameters, such as membrane properties or adhesion kinetics, are studied.

A coarse-grained cell model, which includes a lipid-bilayer cell membrane and a bulk cytoskeleton, is introduced. To incorporate effects of fluid environment, we additionally present two simulation frameworks, Brownian dynamics and dissipative particle dynamics. Both methods allow for an effective formulation of fluid properties, such as viscosity and thermal fluctuations. The elastic response of the cell is studied by microplates compression and the effect of various simulation parameters on cell deformation is analyzed, e.g. the bulk Young's modulus and the stretching resistance of the cell membrane. It is shown that the total elastic response can be described by a superposition of the elastic parameters of the cytoskeleton and cell membrane.

Cell blebbing is connected to a number of cell processes such as cell death and cell motility. A membrane bleb is a protrusion formed by a cell membrane that locally detaches from an underlying cell structure such as a cytoskeleton. Stress-induced cell blebbing is studied by adding a contraction mechanism to the employed bulk cytoskeleton model. Additionally, a dynamic, bond-based adhesion between cell membrane and inner network is introduced. The model is able to reproduce cell blebbing, which occurs for a limited parameter range. By employing mean-field calculations and computer simulations, the effects of cell membrane properties and the adhesion on cell blebbing

are separated. A number of scaling laws for the onset of blebbing are derived by quantifying the effects of various simulation parameters, e.g. the membrane bending rigidity and the number of adhesion binding sites.

Today, malaria is still one of the deadliest diseases and attributes to about half a million human deaths every year. Malaria parasites reproduce by invading red blood cells in the human blood stream. Before the invasion takes place, a parasite may induce various deformations at the membrane of a targeted red blood cell. According to the passive compliance hypothesis, these deformations are a result of the adhesion of the parasite to the cell membrane and aid the malaria parasite alignment. The successful alignment of the parasite head is an important step in the invasion process. To test these assumptions, simulations of a red blood cell and a parasite are employed, in which they interact either via an attractive potential or through a bond-based, dynamic adhesion.

Both employed interaction models can reproduce red blood cell deformations comparable to those in experiments. The deformations are induced by the mechanical interaction between parasite and red blood cell. The adhesion force required for these deformations is on the same order of magnitude as measured in experiments. With the bond-based adhesion, the parasite dynamics and red blood cell deformations observed *in vitro* are reproduced. Parasite alignment is quantified by a number of parameters, such as alignment angle and alignment time, and a reliable parasite alignment through the bond-based adhesion is shown. The effect of various simulation properties on parasite alignment is studied and the egg-like parasite shape, which was measured in *in vitro* and *in vivo* experiments, is shown to lead to the highest alignment probability. Other important aspects for the parasite alignment are the average bond lifetimes and the length of bonds. Finally, the importance of the red blood cell deformations for a successful parasite is shown and it is concluded that the passive compliance hypothesis can explain a number of experimental observations of malaria parasite alignment.

Kurzzusammenfassung

Die Mechanik und Adhäsion von Zellen spielen in biologischen Systemen eine wichtige Rolle. Wir konzentrieren uns in dieser Arbeit auf zwei Beispiele, stressbedingtes *cell blebbing* (Blasenbildung der Lipidmembran) und die Deformation von roten Blutkörperchen während der Invasion durch Malariaparasiten. Zu diesem Zweck erarbeiten wir Simulationsmodelle und analysieren die Effekte von verschiedenen Parametern.

Die Untersuchungen basieren auf einem einfachen Zellmodell, welches aus einer Zellmembran und einem Cytoskelett besteht. Zusätzlich werden zwei verschiedene Arten von Flüssigkeitssimulation vorgestellt, *Brownian dynamics* und *dissipative particle dynamics*. Beide Methoden erlauben die effektive Modellierung von Flüssigkeiten, hauptsächlich deren Viskosität und thermischen Fluktuationen. Die Elastizität des Zellmodells wird mit Hilfe von Mikroplatten-Kompression studiert und der Effekt von verschiedenen Simulationsparametern, z.B. von dem Elastizitätsmodul des Cytoskeletts, analysiert. Die Ergebnisse zeigen, dass die komplette elastische Reaktion der Zelle durch Superposition der elastischen Kenngrößen der Zellmembran und des Cytoskeletts beschrieben werden kann.

Cell blebbing ist Bestandteil von verschiedenen Zellprozessen, zum Beispiel dem Zelltod oder der Bewegung von Zellen. Hierbei bilden sich Blasen, bei denen ein Teil der Membran nicht mehr mit dem Cytoskelett der Zelle verbunden ist. Wir studieren stressbedingtes *cell blebbing*, indem wir dem vorgestellten Cytoskelettmodell einen Mechanismus zur kontrollierten Kontraktion hinzufügen. Zusätzlich wird dynamische Adhäsion zwischen Zellmembrane und Cytoskelett eingeführt. Dieses erweiterte Modell erlaubt *cell blebbing* für einen beschränkten

Bereich von Simulationsparametern. Durch Mean-Field-Rechnungen und Computersimulationen werden die Effekte der Zellmembraneigenschaften und des Adhäsionsmodells separiert. Durch die Quantifizierung der Effekte von verschiedenen Simulationsparametern, wie z.B. der Biegesteifigkeit der Membran oder der Anzahl der Bindungsstellen der Adhäsion, finden wir verschiedene Skalierungsgesetze für das Einsetzen von *cell blebbing*.

Bis zum heutigen Tag ist Malaria eine der tödlichsten Krankheiten, welche für fast eine halbe Million menschliche Tode jedes Jahr verantwortlich ist. Malariaparasiten vermehren sich, indem sie in rote Blutkörperchen im menschlichen Blut eindringen. Vor dem Eindringen können die Parasiten starke Deformationen in der Membran von roten Blutkörperchen auslösen. Die "*passive compliance*" Hypothese besagt, dass diese Deformationen das Ergebnis der Adhäsion zwischen Malariaparasit und roten Blutkörperchen sind und der Ausrichtung des Malariaparasiten dienen. Die Ausrichtung des Parasitenkopfes ist ein wichtiger Bestandteil des Eindringprozesses. Simulationen von roten Blutkörperchen und Malariaparasiten werden verwendet, um diese Annahmen zu untersuchen und zu verifizieren. Dabei interagieren die beiden Zellen entweder durch ein attraktives Potential oder durch dynamische Adhäsion.

Beide Modelle können Membrandeformationen durch mechanische Wechselwirkungen erzeugen, die auch experimentell beobachtet wurden. Die benötigte Adhäsionskraft für diese Deformationen ist in derselben Größenordnung wie in den Experimenten. Mit dem dynamischen Wechselwirkungsmodell kann die Dynamik des Parasiten und die Deformation von roten Blutkörperchen in *in vitro* Experimenten dargestellt werden. Die Ausrichtung des Parasiten wird durch verschiedene Parameter, wie dem Ausrichtungswinkel und der Ausrichtungszeit, quantifiziert. Wir zeigen, dass der Parasit im Mittel senkrecht zur Membran des Blutkörperchens ausgerichtet wird. Die Effekte verschiedener Simulationsparameter auf die Qualität der Ausrichtung werden studiert. Dabei zeigen wir, dass die eiförmige Form des Parasiten, welche *in vitro* und *in vivo* gefunden wurde, für die Ausrichtung optimiert ist. Weitere wichtige Aspekte für die Qualität der Ausrichtung

sind die durchschnittliche Lebensdauer und die Länge der Interaktion zwischen Parasiten und roten Blutkörperchen. Schließlich wird die Abhängigkeit der Ausrichtungsqualität von den Deformationen der roten Blutkörperchen gezeigt. Aus den Ergebnissen schließen wir, dass das verwendete Modell für die Wechselwirkung zwischen Blutkörperchen und Parasiten eine Reihe von experimentellen Beobachtungen sehr gut erklären kann.

Note of Thanks

Writing a Ph.D. thesis is a long and challenging process, which required in this case more than three years of work. Naturally, such a process is not possible without the help of a lot of people, whom I want to thank at this point.

I thank Dmitry A. Fedosov for the opportunity to work in his group, the supervision of my thesis, his feedback, ideas and general support. I really appreciate our time working together.

I thank Gerhard Gompper for letting me do my Ph.D. in his institute, his feedback, and the possibility to present my work at various conferences.

I thank Meike Kleinen, our institute secretary, for doing a wonderful job and for the much needed small talk in breaks.

I thank the permanent scientific staff of ICS-2, Roland Winkler, Marisol Ripoll, Gerrit Vliegthart, Benedikt Sabass, Thorsten Auth, and Jens Elgeti, for answering my questions when needed and for a lot of discussions, not only regarding science.

I thank the members of IHRS BioSoft for the opportunity to learn about their interesting fields of work. I thank Thorsten Auth for the organization of the school.

Keeping up with me on day-to-day basis is no easy task, therefore I want to thank all friends and colleagues, who did this over the years. I thank Mario, Mahdi, and Sameh for being wonderful office mates, whom I could always bother with completely useless facts about everything. I thank Kseniia for being a wonderful guest student, putting up with me as a teacher. I thank Martin for being a good friend and

helping me out with LAMMPS more times than I remember. I thank Tobias for putting up with me being a supporter of Borussia Dortmund and still talking to me regularly. I thank all other former and current students and PostDocs of ICS-2 for scientific discussions as well as relaxed conversations at lunch.

I thank Cornelis, Dennis, and Manfred for being good friends and a lot of time spent playing board games.

I thank Megan and Mitch for being Megan and Mitch, two of the most wonderful people I have ever met.

I thank Marvin for being the best.

I thank Sanja for being a good listener and friend when I really needed one.

I thank my parents for supporting me my whole life. I thank my family and my in-laws for all the help I received over the years.

Lastly, I want to thank the most important person in my life. Without Bettina, I would neither have started my Ph.D. thesis nor finished it. I would not be remotely close to the point, where I am in my life without my lovely wife and I am grateful for it everyday.

Contents

| | |
|--|-------------|
| Acronyms | xvii |
| Symbols | xvii |
| List of Figures | xxi |
| List of Tables | xxv |
| 1 Introduction | 1 |
| 1.1 Cell Structure | 2 |
| 1.1.1 Lipid Bilayer Cell Membrane | 2 |
| 1.1.2 Cell Cytoskeleton | 4 |
| 1.2 Cell Deformations | 6 |
| 1.3 Thesis Structure | 8 |
| 2 Simulation Methods | 11 |
| 2.1 Dissipative Particle Dynamics | 13 |
| 2.1.1 Measurement of Fluid Viscosity | 15 |
| 2.2 Brownian Dynamics | 17 |
| 2.3 Simulation Units | 18 |
| 3 Cell Model | 21 |
| 3.1 Bulk Cytoskeleton | 22 |
| 3.1.1 Microplate Compression Setup | 23 |
| 3.1.2 Comparison Between Theory and Simulation | 25 |
| 3.2 Spherical Elastic Particles | 28 |
| 3.3 Cell Membrane | 30 |
| 3.4 Conclusions | 37 |

| | | |
|----------|---|-----------|
| 4 | Stress-Induced Cell Blebbing | 39 |
| 4.1 | Stress-Induced Blebbing in Synthetic Cells | 40 |
| 4.2 | Simulation Model of Cell Blebbing | 43 |
| 4.2.1 | Contractile Inner Network | 43 |
| 4.2.2 | Membrane-Cytoskeleton Interaction | 48 |
| 4.3 | Cell Blebbing Results | 49 |
| 4.3.1 | Theoretical Prediction of the Blebbing Onset | 54 |
| 4.3.2 | Results for Rigid Membranes | 58 |
| 4.3.3 | Results for Flexible Membranes | 62 |
| 4.3.4 | Effects of Bending Rigidity and Volume Constraint | 64 |
| 4.3.5 | The Effect of the Area Constraints | 67 |
| 4.3.6 | Theoretical Analysis of Blebbing | 71 |
| 4.4 | Conclusions | 74 |
| 5 | Malaria Parasite Alignment | 77 |
| 5.1 | The Malaria Cycle | 77 |
| 5.2 | Invasion of a Red Blood Cell | 80 |
| 5.3 | Simulation Models | 83 |
| 5.3.1 | Red Blood Cell Model | 83 |
| 5.3.2 | Parasite Model | 85 |
| 5.3.3 | Hydrodynamic Interactions | 87 |
| 5.3.4 | Potential Adhesion Interaction | 87 |
| 5.3.5 | Two-State Adhesive Bond Model | 89 |
| 5.4 | Results of the Potential Interaction Model | 90 |
| 5.4.1 | Membrane Deformations | 92 |
| 5.4.2 | Adhesive Force | 98 |
| 5.4.3 | Discussion of the Potential Interaction Model | 103 |
| 5.5 | Results of the Dynamic Bond Model | 104 |
| 5.5.1 | Surface Velocity of an Adhered Parasite | 107 |
| 5.5.2 | Parasite Alignment Characteristics | 112 |
| 5.5.3 | Effect of the Parasite Shape | 121 |
| 5.5.4 | Are Different Bond Types Required? | 127 |
| 5.5.5 | Influence of the Average Bond Lifetime | 129 |
| 5.5.6 | Rigid RBC Membrane | 130 |
| 5.5.7 | Discussion of the Dynamic Bond Model | 133 |

| | | |
|----------|--|------------|
| 5.6 | Conclusions | 134 |
| 6 | Summary, Conclusions, and Outlook | 137 |
| | Bibliography | 141 |

Acronyms

| | |
|------|-----------------------------------|
| BD | Brownian dynamics |
| DPD | dissipative particle dynamics |
| EL | long-ellipsoid parasite shape |
| ES | short-ellipsoid parasite shape |
| FEM | finite elements methods |
| LBM | Lattice Boltzmann methods |
| LJ | Lennard-Jones |
| MC | Monte Carlo |
| MD | molecular dynamics |
| MPCD | multi-particle collision dynamics |
| PA | pear-like parasite shape |
| PDE | partial differential equation |
| RBC | red blood cell |
| SP | spherical parasite shape |
| SPH | smoothed particle hydrodynamics |

Symbols

| | |
|---------|--------------------------------------|
| a | Parasite interaction gradient power. |
| A^0 | Membrane rest area. |
| A_i^0 | Membrane triangle rest area. |

| | |
|---------------------------------|--|
| a_{ij} | DPD conservative force interaction strength. |
| α | Membrane rescaling factor of $C_{\text{crit}}^{\text{theo}}$. |
| c | Spring contractile factor. |
| C | Network contraction. |
| $C_{\text{crit}}^{\text{meas}}$ | Measured critical blebbing network contraction. |
| $C_{\text{crit}}^{\text{theo}}$ | Calculated critical blebbing network contraction. |
| D_0 | Length scale, usually the average cell diameter. |
| Δt | Simulation timestep. |
| ϵ | Engineering strain. |
| ϵ_a | Interaction strength of potential adhesion model. |
| ϵ_{LJ} | Interaction strength for wall LJ potential. |
| ΔE_{rbc} | RBC deformation energy. |
| η | Fluid viscosity. |
| F_{ad} | RBC-parasite adhesion force. |
| F_B | Force sensitivity of dissociation rate. |
| F_C | Surface force of contracting network. |
| F_{compress} | Microplates compression reaction force. |
| \mathbf{F}_{ij}^C | Conservative force in DPD. |
| \mathbf{F}_{ij}^D | Dissipative force in DPD. |
| F_I | Membrane-network connection bond force. |
| \mathbf{F}_{ij}^R | Random force in DPD. |
| γ | Friction coefficient. |
| $\dot{\gamma}$ | RBC strain rate. |
| I_d | Deformation index. |
| k_{ag} | Global membrane area constraint parameter. |
| k_{al} | Local membrane area constraint parameter. |
| κ | Membrane bending rigidity. |
| $k_{\text{B}}T$ | Thermal energy. |
| k_{off} | Bond dissociation rate. |
| k_{off}^0 | Bond base dissociation rate. |
| k_{on} | Cell blebbing bond association rate. |

| | |
|-------------------------------------|---|
| k_{on}^0 | Cell blebbing bond base association rate. |
| $k_{\text{on}}^{\text{long}}$ | Parasite long bond association rate. |
| $k_{\text{on}}^{\text{short}}$ | Parasite short bond association rate. |
| k_{vg} | Global membrane volume constraint parameter. |
| λ | Spring constant of elastic network. |
| λ_{ad} | Parasite adhesion spring constant. |
| $\lambda_{\text{ad}}^{\text{type}}$ | Parasite adhesion spring constant of bonds of certain type. |
| λ_{C} | Effective spring constant of the cytoskeleton. |
| $\tilde{\lambda}_{\text{C}}$ | Spring constant of a cytokeletal bond. |
| λ_{I} | Spring constant of a bond between membrane and inner network. |
| λ_{p} | RBC spring constant. |
| l_i | Instantaneous length of bond i . |
| l_i^0 | Rest length of bond i . |
| l_{p} | RBC spring persistence length. |
| m | Particle mass. |
| μ_0 | RBC membrane shear module. |
| N' | Number of bonds connecting cell membrane and cytoskeleton. |
| N_S | Number of springs in cytoskeleton. |
| N_S^M | Number of springs in cell membrane. |
| N_T^M | Number of triangles in cell membrane. |
| N | Number of vertices in cytoskeleton. |
| N^M | Number of vertices in cell membrane. |
| ϕ | Dimensionless ratio $k_{\text{on}}^0/k_{\text{off}}^0$. |
| R | Instantaneous cytoskeleton radius. |
| r_c | Cutoff radius. |
| R_C^0 | Initial radius of contracting network. |
| ρ | DPD fluid particle number density. |
| ρ_a | Parasite agonist density. |

| | |
|----------------------|---|
| R_M | Spherical cell membrane radius. |
| σ | Length scale in LJ potentials. |
| τ | Dimensionless time tk_{off}^0 . |
| τ_{equi} | Dimensionless time before blebbing. |
| θ | Alignment angle. |
| V^0 | Membrane rest volume. |
| w^C | DPD conservative force weight function. |
| w^D | DPD dissipative force weight function. |
| w^R | DPD random force weight function. |
| Y | Cytoskeleton Young's modulus. |
| Y^M | RBC membrane Young's modulus. |
| \tilde{Y} | Effective contribution of cell membrane to total Young's modulus. |

List of Figures

| | | |
|------|---|----|
| 1.1 | Schematic sketch of a cell membrane | 3 |
| 1.2 | Image of bovine endothelial cells from pulmonary arteries | 5 |
| 1.3 | Flowing RBCs in a glass tube with a diameter of $7\ \mu\text{m}$ and in a capillary with approximately the same diameter | 7 |
| 2.1 | Overview of length- and timescales in the realm of physics | 11 |
| 2.2 | Sketch of the reverse Poiseuille flow setup | 16 |
| 3.1 | Selection of different types of models to study the prop- erties and behavior of various cells | 21 |
| 3.2 | Sketch of a microplate compression experiment for a spherical elastic particle | 24 |
| 3.3 | Poisson's ratio ν for a simulation setup with $N = 69\,051$ vertices and $N_S = 499\,779$ springs | 26 |
| 3.4 | Force and strain measured for the compression of a cu- bic elastic network | 27 |
| 3.5 | Force-strain curve for an elastic sphere for a setup with $N = 4197$ vertices and $N_S = 28\,621$ springs | 29 |
| 3.6 | Sketch of a lipid-bilayer cell membrane model | 31 |
| 3.7 | Force-strain data for a compression test with the membrane- cytoskeleton model | 33 |
| 3.8 | Contribution of the volume constraint characterized by k_{vg} to the membrane response \tilde{Y} | 34 |
| 3.9 | Contribution of the bending rigidity characterized by κ to the membrane response \tilde{Y} | 35 |
| 3.10 | Contribution of the area constraints to the membrane response \tilde{Y} | 36 |

| | | |
|------|---|----|
| 4.1 | Sketch and confocal-microscopy image of cell blebbing | 39 |
| 4.2 | Synthetic cells consisting of a lipid-bilayer membrane and an active actin network | 41 |
| 4.3 | Formation of stress-induced blebs | 42 |
| 4.4 | Schematic of the model to study cell blebbing | 44 |
| 4.5 | Measurement of the inner network radius R over the course of different simulations | 46 |
| 4.6 | Comparison between the potential energies of a contracting network | 47 |
| 4.7 | Two-dimensional sketch of the interaction between the membrane and the inner network | 48 |
| 4.8 | Time series for different values of C | 51 |
| 4.9 | Blebbing transition measured through the bleb volume | 53 |
| 4.10 | Sketch of the relevant radii within a cell model | 55 |
| 4.11 | Instantaneous radius R for contracted cells without unbinding (i.e $k_{\text{off}}^0 = 0$) as a function of the contraction C | 57 |
| 4.12 | Instantaneous radius R as a function of the simulation time τ for cells with rigid membranes and different contractions | 59 |
| 4.13 | Average equilibration time τ_{equi} as a function of applied contraction | 60 |
| 4.14 | Measured values of $C_{\text{crit}}^{\text{meas}}$ compared to their theoretically predicted values $C_{\text{crit}}^{\text{theo}}$ for rigid cell membranes . | 62 |
| 4.15 | Average equilibration time τ_{equi} as a function of the applied contraction for flexible cell membranes | 63 |
| 4.16 | Average blebbing time as a function of $C/C_{\text{crit}}^{\text{theo}}$ for different volume constraint constants k_{vg} | 64 |
| 4.17 | Example cell shapes for simulated configurations with various volume constraints | 65 |
| 4.18 | Values of τ_{equi} for different bending rigidities κ (top) and two shape examples (bottom) | 66 |
| 4.19 | $C_{\text{crit}}^{\text{meas}}$ measured against theoretical values $C_{\text{crit}}^{\text{theo}}$ for fixed ratio $\lambda_C/k_{\text{ag}} = 38.01$ | 68 |
| 4.20 | α as a function of the ratios λ_C/k_{ag} and λ_C/k_{al} | 69 |
| 4.21 | Cell shape examples for various values of the ratio λ_C/k_{ag} | 70 |

| | | |
|------|---|-----|
| 4.22 | Dependence of $C_{\text{crit}}^{\text{theo}}$ on the number of binding sites, the contraction strength λ_C , and the strength of the adhesion bonds λ_I | 72 |
| 4.23 | Dependence of $C_{\text{crit}}^{\text{theo}}$ on the number of binding sites, the binding-unbinding ratio ϕ , and the force sensitivity F_B | 73 |
| 5.1 | Schematic of the malaria cycle within humans | 78 |
| 5.2 | Schematic view of the merozoite during the blood stage | 79 |
| 5.3 | Different stages of a successful invasion event | 80 |
| 5.4 | Examples of different membrane deformations <i>in vitro</i> | 81 |
| 5.5 | Schematic of a RBC model | 84 |
| 5.6 | Sketch of the different shapes used to model the parasite | 86 |
| 5.7 | Schematic of the vectors used to calculate the interaction gradient | 88 |
| 5.8 | Example of a parasite adhering to a RBC | 92 |
| 5.9 | Deformation energies for the simulation shown in fig. 5.8 | 93 |
| 5.10 | Deformation energy for $a = 0$ and different values of ϵ_a | 94 |
| 5.11 | Examples for different deformation indices | 95 |
| 5.12 | Deformation energy for different values of a | 97 |
| 5.13 | Examples of the adhered parasite for $a = 0, 1, 2, 3$. . . | 98 |
| 5.14 | Schematic of the pulling test to measure the adhesion force | 98 |
| 5.15 | Pulling test to measure the adhesion force | 99 |
| 5.16 | Determination of the strain rate $\dot{\gamma}$ | 100 |
| 5.17 | Adhesion force as a function of the interaction strength for the different interaction models | 101 |
| 5.18 | Adhesion force as a function of the interaction strength for stiffened RBCs | 102 |
| 5.19 | Snapshots from one simulation with dynamic bond model | 106 |
| 5.20 | Surface velocity of the parasite computed by frame by frame analysis of <i>in vitro</i> experiments | 107 |
| 5.21 | Distributions of the surface velocities from experiments and simulations | 108 |
| 5.22 | Surface velocity and average number of bonds for different cases | 109 |

| | | |
|------|--|-----|
| 5.23 | Surface velocity for different parameter sets | 110 |
| 5.24 | Average number of bonds for different parameter sets . | 111 |
| 5.25 | Visualization of the head distance and angle measure- ments | 113 |
| 5.26 | Distribution of the head distance d for the reference setup | 114 |
| 5.27 | Distribution of the alignment angle θ for the reference setup | 115 |
| 5.28 | Alignment time for the reference configuration | 116 |
| 5.29 | Two dimensional probability distribution of (d_i, θ_j) . . | 118 |
| 5.30 | Distribution of the alignment times using MC simula- tions for the reference configuration | 119 |
| 5.31 | Distribution of the deformation energy for the reference configuration | 120 |
| 5.32 | Deformation energies for different shapes and different values of k_{off} | 122 |
| 5.33 | Head distance distributions for different shapes and dif- ferent values of k_{off} | 123 |
| 5.34 | Distributions of the alignment angle for the different shapes | 124 |
| 5.35 | Average relative alignment time for different shapes . . | 126 |
| 5.36 | Alignment times and deformation energies for different ratios $k_{\text{on}}^{\text{short}}/k_{\text{on}}^{\text{long}}$ for short and long bonds | 128 |
| 5.37 | Alignment time for a configuration with and without long bonds | 129 |
| 5.38 | Alignment times for different values of $k_{\text{on}}^{\text{long}}$ | 130 |
| 5.39 | Comparison of the alignment times between rigid and flexible RBCs | 131 |
| 5.40 | Head distance and alignment angle for rigid and flexible RBCs | 132 |

List of Tables

| | | |
|-----|--|-----|
| 3.1 | Overview of the main simulation parameters for microplate compression tests | 25 |
| 3.2 | Comparison of the elastic constants for different levels of mesh discretization and spring constants | 28 |
| 3.3 | Measured Youngs's modulus for different settings and spring constants of elastic spheres | 30 |
| 4.1 | Overview of the main simulation parameters for cell blebbing simulations | 50 |
| 4.2 | Measured values of C_{crit}^{meas} compared to their theoretically predicted values C_{crit}^{theo} for rigid cell membranes . | 61 |
| 4.3 | C_{crit}^{meas} measured against theoretical values C_{crit}^{theo} for fixed ratio $\lambda_C/k_{ag} = 38.01$ | 67 |
| 5.1 | Characteristic parameters of the introduced parasite shapes | 86 |
| 5.2 | Overview of the main simulation parameters | 91 |
| 5.3 | Discrete deformation index to quantify the level of deformation | 96 |
| 5.4 | Interaction parameters for the bond adhesion model . | 105 |

1 Introduction

The body is a community
made up of its innumerable
cells or inhabitants.

Thomas A. Edison (1847 -
1931)

Cells are one of the fundamental building blocks of life. Nearly any structure and function of a living organism can be connected to one or several cells fulfilling various tasks to keep organisms homeostatic. As a result, cells spark the interest of researchers all around the world since their first discovery by Robert Hooke in 1665 [1] till today. For example, in 2018, the Nobel price in physics was awarded for the invention of the optical tweezers and their application to biological systems [2].

The main difficulties in studying cells are their variety, complexity, and the huge number of them forming a living organism. For a human body, around 200 [3] different types of cells are known, their sizes ranging between 0.1 nm and 100 μm . Recent approximations suggest a total number of 3.8×10^{13} cells forming the whole body [4]. About 84% of these cells are erythrocytes, also known as red blood cells (RBCs), whose main function is the transport of oxygen from the lungs to the rest of the body. On the other side, epidermal cells, which form the skin tissue, account only for about 0.5% of the total number of cells, but without them, our live would be quite different [4].

1.1 Cell Structure

Cells are constructed in various ways to fulfill the vast number of tasks. Therefore, no generic building schemes valid for all cells exist. Nevertheless, most cells share a number of similar features. The inside of the cell is made of cytoplasm, which consists of about 80% water with various suspended biomolecules such as proteins and nucleic acids [5]. The cytoplasm is enveloped by a membrane that controls the entry and exit of fluids and other materials of the cell and maintains the electric potential of the cell. The shape of cells is mainly determined by a cytoskeleton enclosed by the membrane. Depending on the cell type, this structure can be volume spanning or may only form a two-dimensional network close to the membrane. Lastly, most cells have a full copy of the genetic information stored by the DNA in a cell nucleus. Depending on the existence of the nucleus, cells are characterized as eukaryotic (with nucleus) and prokaryotic (without nucleus) cells. [5]

1.1.1 Lipid Bilayer Cell Membrane

A cell membrane mainly consists of lipids, which are amphiphilic biomolecules with a hydrophilic head group and a hydrophobic tail. They self-organize in aqueous environments into two sheets, with their head groups pointing outwards and their tails protected from water contact, and are packed together as closely as possible (see fig. 1.1). This lipid-bilayer forms a continuous barrier between the cytoplasm and the outside of the cell, preventing a free exchange of different materials between the outside and the inside of the cell. Within this bilayer, different membrane proteins may be embedded or attached. [5]

The intra-membrane proteins may vary between different cell types and fulfill a variety of different tasks [7]. They are so important for the function of the cells that around 30% of the genes in an organism code for membrane proteins [8]. Common examples of these proteins

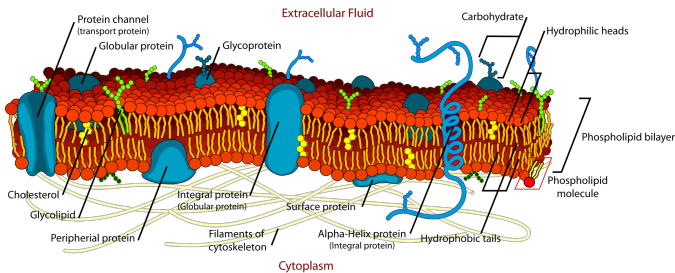


Figure 1.1: Schematic sketch of a cell membrane. The lipids self-organize into a bilayer structure to minimize the contact of their hydrophobic tail groups with the surrounding fluids. The bilayer effectively separates the outside and the inside of the cell. In the bilayer sheets, a number of proteins and other biomolecules are embedded, i.e. channels, which allow a controlled exchange of ions, or receptors, which control the interaction with the surrounding environment. Picture taken from [6] (open domain).

are channels and pumps, which allow for a controlled exchange of materials, such as proteins or ions. These materials may be used either as building blocks or as chemical signals within the cell, which guide the behavior of the cell. Other examples are membrane receptors, which can be used for the communication between the membrane and the extracellular space by binding certain transmitter proteins or other molecules.

Cell membranes play a vital role in the cell behavior. Membranes in mathematical and physical cell models are often represented as two-dimensional surfaces. This approach is useful, since a typical cell membrane has a thickness between 5 nm and 10 nm [9] and is therefore quite thin in comparison to the diameter of most eukaryotic cells. Due to the bilayer structure, cell membranes resist bending deformation,

which is usually modeled by the Helfrich Hamiltonian [10] as

$$U_{\text{Helf}} = \int_A dA \frac{1}{2} \kappa (c_1 + c_2 - c_0)^2 + \bar{\kappa} c_1 c_2, \quad (1.1)$$

where κ is the bending rigidity of the membrane, $\bar{\kappa}$ is the saddle-splay modulus, and A is the membrane surface area. The parameters c_1 and c_2 describe the principal curvatures at every membrane point and c_0 is the spontaneous curvature, determining the stress-free state of the membrane. The last term on the right-hand side is known as Gaussian curvature. The Hamiltonian describes an elastic energy cost to bend the membrane away from its original shape, such that these deformations require the application of external forces. Typical values of κ are in the range from of 1×10^{-20} N m to 1×10^{-19} N m [11].

1.1.2 Cell Cytoskeleton

The cytoskeleton of a cell consists of filaments and tubules of different lengths and stiffnesses [12] (see fig. 1.2). The cytoskeleton may span throughout the whole cell and is responsible for its general shape and the cell resistance to mechanical stresses [5]. Depending on cell type, other functions may be performed by the cytoskeleton, such as cell movement [15], cell signaling and the generation of cellular forces [15, 16].

The constituents of the cytoskeleton vary depending on cell type. In eukaryotic cells, the cytoskeleton generally consists of actin filaments, intermediate filaments, and microtubules. These filaments differ in size, rigidity, and function within the cell. Microtubules are stiff and hollow rods, which structurally start from a central organelle within the cell [17]. They have an average diameter of 24 nm with a persistence length of a couple of μm [18]. Microtubules are composed of α - and β -tubulin, which self-organize in alternating, helical structures. The incorporation of the tubulin-blocks into microtubules is dynamic and may lead to rapid growth and shrinkage behavior at the unbound

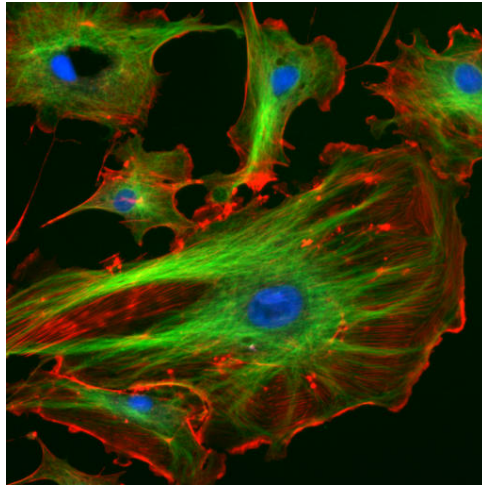


Figure 1.2: Image of bovine endothelial cells from pulmonary arteries. The red dye marks actin-filaments, the green color represents the microtubules, and the cell nuclei are stained blue. The cytoskeleton determines the shape of the cell. The organization within the cytoskeleton varies locally, as the distinct filaments are responsible for different functions in the cell. Picture taken from ImageJ project [13, 14].

end [19]. Within the cell, microtubules function as paths for cargo transport and molecular motors [20]. They also play a vital role in the separation of chromosomes during cell division [21].

Intermediate filaments provide stability for the cell by forming a network, which absorbs mechanical stress [18, 22]. Depending on the cell type and the required functions, various kinds of structures may be formed by the filaments. Intermediate filaments are composed of protofilaments, which are bundled together forming the filament structure. They usually have a diameter of around 10 nm and a persistence length on the order of hundreds of nm [18].

The structure of cells is mainly controlled by an actin cortex, a

thin network layer beneath the cell membrane (see fig. 1.2, red dye). This layer is formed of actin filaments [16], which are built from actin monomers (G-actin) and form F-actin filaments. Actin filaments are polarized and have a double helical structure. The typical diameter is between 5 nm and 9 nm and the persistence length is on the order of tens of μm [18]. Similar to microtubules, actin incorporates its monomers by the polymerization at one end, but it also loses building blocks at the other end. This leads to a highly dynamic tread-milling behavior of the actin filaments [18]. Actin together with the molecular motor myosin plays a vital role in the generation of contraction forces, as the myosin protein is able to slide along the polarized actin filaments and generate contractile forces on the order of 3 pN to 4 pN [23, 24].

While the cytoskeleton and the cell membrane consist of different molecules and form distinct structures, they also interact. This membrane-cytoskeleton adhesion is usually mediated by various linker molecules, which form bonds between the constituents of both parts. The connection is loose, such that the cell membrane is still able to move and shows membrane flickering. Additionally, the stability of the connection is sensitive to various biochemical components and mechanical stresses, which allows for structural reorganization during various cell processes. [25]

Different approaches exist for modeling of the function and mechanical effects of the cytoskeleton. These models range from detailed descriptions at the level of single protein filaments [26] to the continuous description of the cell as an elastic material [27]. Which model should be used depends on the involved lengthscales and the questions to be addressed.

1.2 Cell Deformations

One way to describe mechanical properties of cells is to use elastic constants, such as the three-dimensional Young's modulus. For cells, typical values are in the range of 1 kPa and 100 kPa [28], which is

many orders of magnitudes smaller than e.g. steel with values around 200 GPa [29]. The Young's modulus characterizes the deformability of cells, which is important for many cell functions.

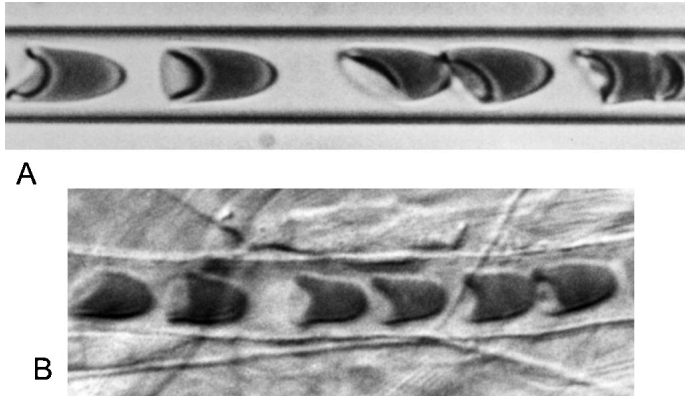


Figure 1.3: Flowing RBCs in a glass tube with a diameter of $7\ \mu\text{m}$ (A) and in a capillary with approximately the same diameter (B). While passing through the narrow channel, the cells deform drastically in comparison to their rest shape. Picture taken from [30] with permission.

One example for the effect of cell deformations is the transport of oxygen by RBCs through the vascular system. The vascular system of humans consists of a large variety of vessels ranging from big arteries with a diameter on the order of a couple of mm to small capillaries with a diameter between $3\ \mu\text{m}$ and $10\ \mu\text{m}$. The average size of RBCs is about $8\ \mu\text{m}$, such that they can easily travel through large vessels. When the cells reach small capillaries, the RBCs need to deform dramatically, as shown in fig. 1.3. When the cells return to large arteries and veins again, their cytoskeletal network restores their original shape. This dynamic transition allows every cell to pass the blood circle numerous times before it is sorted out by the spleen [31].

The example of RBCs demonstrates the importance of the cell's

mechanical properties and a number of techniques are available to measure quantities such as Young's modulus and other mechanical characteristics. These techniques can be divided into two classes: direct force application and force sensing methods [32].

Force application techniques exert external stresses to deform cells and derive their elastic properties by interpreting the cell reaction. The applied forces can be of various types, e.g. mechanical stress using atomic force microscopy [33–37]. Other methods utilize optical techniques (optical tweezers [38–42], optical stretcher [43–46]), magnetic and/or electric stimulation (magnetic tweezers [47–50], electric field stimulation [51, 52]), or acoustic approaches (acoustic tweezers [53–55]). To study cells in flow environments, a number of flow techniques are available [56–64]. For example, in microfluidic devices, cells are deformed by flow stresses and through the interaction with geometrical boundaries such as shown in fig. 1.3.

Force sensing techniques focus on forces that are a result of internal cell processes. Examples are cell motility and reorganization during cell division. A number of methods such as optical tweezers and atomic force microscopy may also be applied within the force sensing context [32].

The interpretation of experimental results often requires models to quantify the elastic properties. Experimental measurements of cell mechanics may be too complex to be reliably quantified by analytical models, such that computer models and simulations are required for interpretation. The resulting field of computational physics can be placed between the experimental and theoretical branches of physics and plays an important role in ongoing research.

1.3 Thesis Structure

In this thesis, a number of *in silico* models are employed to study various aspects of cell-membrane deformations and adhesion. In particular, we identify the physical mechanisms leading to stress-induced cell

blebbing and the RBC deformations through the adhesion of malaria parasites.

In chapter 2, a short introduction into the broad field of computational physics is given. We present two simulation frameworks, dissipative particle dynamics [65] and Brownian dynamics, which allow the modeling of hydrodynamic interactions and cell mechanics.

A cell model is introduced in chapter 3. Cells are described by a number of simulation particles, which represent a volume-spanning cytoskeletal network and a lipid-bilayer cell membrane. The elastic properties of the cell are quantified by simulating cell compression by microplates [66]. We investigate the effect of different membrane and cytoskeleton parameters on the total cell deformation and show that the elastic response of the cell is a superposition of the inner network and membrane responses.

Cell blebbing is a common cell phenomenon occurring in various processes such as cell motility and cell death [67–73]. A bleb is a cell membrane protrusion, which appears when membrane and cytoskeleton disconnect locally. Blebbing may occur due to different mechanisms, one of which is stress-induced cell blebbing. Here, the active contraction of an actin network by myosin motors leads to blebbing [74]. In chapter 4, stress-induced cell blebbing is studied. We extend the cell model by adding network contraction and a dynamic membrane-cytoskeleton adhesion [25, 75]. By quantifying the effects of various parameters, we obtain criteria for the existence of stress-induced cell blebbing.

Another biological process considered in this thesis is the adhesion of malaria parasites to RBCs. Malaria is caused by parasites, which employ RBCs to progress through various stages of a complex life cycle and ensure their survival [76]. The invasion of human RBCs by parasites is an important step in this cycle. Before the invasion, parasites interact with a targeted RBC and induce various levels of deformation of the cell membrane [77–86]. We study the pre-invasion stage of malaria parasites with a cell membrane model of a healthy RBC in chapter 5. The RBC interacts with a parasite through an ad-

hesive interaction, which is either represented by an attractive potential interaction model or by a bond-based, dynamic adhesion model. The models are used to investigate the passive compliance hypothesis, which explains the membrane deformations purely by mechanical interactions [86].

2 Simulation Methods

Physics is a broad field that aims to explain a wide range of phenomena, starting from the movement of the stars and planets within the universe to the mechanics of the smallest particles that form this universe. Clearly, these problems have different length- and timescales

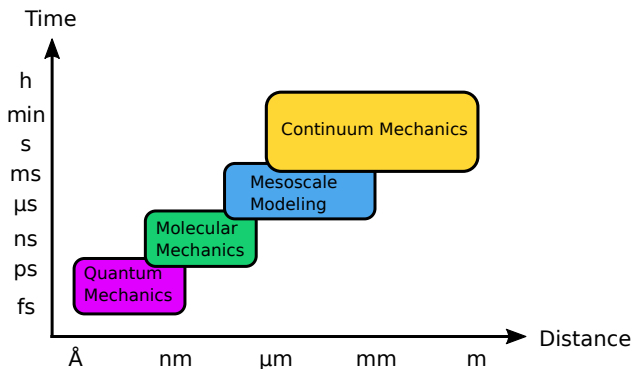


Figure 2.1: Overview of length- and timescales in the realm of physics. Over the last decades, a number of different theoretical and computational descriptions and methods have been developed to tackle the problems involving the various scales.

and their investigation requires different approaches (see fig. 2.1). Therefore, a multitude of different methods have been developed to tackle them. One type of approach are numerical simulations, where

complex mathematical models employ the capabilities of modern computers.

For solving different mathematical problems, a variety of computational methods exists, e.g. finding roots of an equation or solving large systems of linear equations. In this thesis, we focus on advanced computer simulations, which are used to study complex systems with a large number of components, e.g. the number of elements in a cell membrane or a fluid. These simulations are generally classified into particle-based and continuum-based simulation techniques. In particle-based simulations, the studied system is discretized into a number of particles that interact with each other. These particles may e.g. represent molecules or small molecular structures, leading to the method of molecular dynamics (MD) simulations. The complexity of MD simulations results from the large number of degrees of freedom representing atomic and molecular structures and therefore MD simulations are often used to study relatively small length- and timescales. Several examples of MD simulations can be found in references [87–93].

Problems at large scales are generally studied with continuum simulation methods. Such methods, e.g. finite elements methods (FEM), utilize partial differential equations (PDEs), such as the Navier-Stokes equation for fluid flow. PDEs are usually discretized by dividing the space into small elements (finite elements) and approximating the equation locally at these elements resulting in a numerical solution for the studied system. Examples of continuum methods can be found in [94–98].

Biophysical problems mostly evolve around cells, their constituents and the networks they form. Cells have different shapes and sizes in the range from $1\ \mu\text{m}$ to $100\ \mu\text{m}$; thus they are best described by mesoscopic models. At cellular lengthscales, physical models have to address an interesting mix of different problems. On the one hand, the number of atoms, which form a single cell, is too high to model cells with atomistic representation using molecular dynamics. Therefore, one has to average out a large number of these atoms to obtain

manageable systems, which reproduce the properties of cells. This process, known as coarse-graining, is a vital step in the establishment of mesoscopic models. On the other hand, supra-molecular, cellular structures such as membranes are important to capture cell mechanics. Therefore, we need to be careful while averaging, such that this essential information is not lost during coarse-graining. Hence, the level of coarse-graining generally depends on the problem of interest and questions addressed.

Cell cytosol is generally represented by a fluid environment. At the same time, cells are suspended into some fluid medium. Therefore, a typical cell simulation includes required structural elements of a cell to represent cell mechanics and two fluids (i.e. cytosol and suspending medium) separated by the cell membrane. A number of simulation techniques have been established to study this type of system, such as multi-particle collision dynamics (MPCD) [99, 100]), smoothed particle hydrodynamics (SPH) [101–104], and Lattice Boltzmann methods (LBM) [105–108]. In this chapter, we introduce the dissipative particle dynamics (DPD) framework, where hydrodynamic effects are modeled by fluid particles, and the Brownian dynamics (BD) framework, which incorporates fluid interactions implicitly. In the following chapters, a number of different cell models are presented, which employ these fluid methods.

2.1 Dissipative Particle Dynamics

To model hydrodynamic interactions, the framework of DPD is used. In DPD, the fluid is modeled by a number of particles and each particle is described by its position \mathbf{r}_i , velocity \mathbf{v}_i , and mass m_i . These particles represent small volumes of the fluid; thus the number of particles is much smaller than the number of molecules. The amount of simulation particles is described by the number density ρ . The fluid particles interact by a pairwise force

$$\mathbf{F}_{ij} = \mathbf{F}_{ij}^C + \mathbf{F}_{ij}^D + \mathbf{F}_{ij}^R \quad (2.1)$$

which conserves the linear and the angular momentum of the fluid [109]. We follow the standard implementation by Español [65] to describe these forces.

The term \mathbf{F}_{ij}^C is a soft, repulsive conservation force that prevents particle overlapping and is given by the relation

$$\mathbf{F}_{ij}^C = w^C(r_{ij}) \mathbf{e}_{ij}, \quad (2.2)$$

where $\mathbf{r}_{ij} = \mathbf{r}_i - \mathbf{r}_j$ is the distance vector between the particles i and j , $r_{ij} = |\mathbf{r}_i - \mathbf{r}_j|$ and $\mathbf{e}_{ij} = \mathbf{r}_{ij}/r_{ij}$. The function w^C is a weight function and is modeled as a decaying function

$$w^C(r_{ij}) = \begin{cases} a_{ij} \left(1 - \frac{r_{ij}}{r_c}\right) & r_{ij} \leq r_c \\ 0 & r_{ij} > r_c \end{cases}, \quad (2.3)$$

where a_{ij} is the interaction strength and r_c is the cutoff radius of the interaction. Their values are chosen to ensure incompressibility of the modeled fluid. They depend on the number density ρ and the thermal energy $k_B T$ of the system.

The force \mathbf{F}_{ij}^D models the fluid viscosity η by introducing a dissipative force and the term \mathbf{F}_{ij}^R models the effects of thermal fluctuations. They are given by

$$\mathbf{F}_{ij}^D = -\gamma w^D(r_{ij}) [\mathbf{v}_{ij} \cdot \mathbf{e}_{ij}] \mathbf{e}_{ij}, \quad (2.4)$$

$$\mathbf{F}_{ij}^R = \sigma w^R(r_{ij}) \theta_{ij} \mathbf{e}_{ij}, \quad (2.5)$$

where γ is a friction constant and σ is the coefficient of the random force. The vector $\mathbf{v}_{ij} = \mathbf{v}_i - \mathbf{v}_j$ is the velocity difference between the particles. The random component of \mathbf{F}_{ij}^R is θ_{ij} . It models Gaussian white noise that is symmetric in i and j to ensure momentum conservation. It fulfills the relations

$$\langle \theta_{ij}(t) \rangle = 0, \quad (2.6)$$

$$\langle \theta_{ij}(t) \theta_{kl}(t') \rangle = (\delta_{ik} \delta_{jl} + \delta_{il} \delta_{jk}) \delta(t - t'). \quad (2.7)$$

To obtain detailed balance, the weight functions need to satisfy

$$w^D(r) = [w^R(r)]^2. \quad (2.8)$$

Then the version of the fluctuation-dissipation-theorem in DPD becomes

$$\sigma^2 = 2\gamma k_B T / m, \quad (2.9)$$

which connects the friction and random contributions to the thermal energy $k_B T$. The weight function is given by

$$w^D(r_{ij}) = [w^R(r_{ij})]^2 = \begin{cases} \left(1 - \frac{r_{ij}}{r_c}\right)^k & r_{ij} \leq r_c \\ 0 & r_{ij} > r_c, \end{cases} \quad (2.10)$$

similar to the weight function of the conservative force. The additional exponent k is used to control the viscosity of the fluid, where $k = 1$ reproduces the original DPD algorithm [110].

The time evolution of one DPD particle \mathbf{x} is determined by Newton's second law of motion $m\ddot{\mathbf{x}} = \mathbf{F}$, where \mathbf{F} is the sum of all forces acting on the particle. Since each particle is influenced by its neighbors, the particle trajectory is obtained by numerical integration using the verlet algorithm, which is given by the equations

$$\mathbf{x}(t + \Delta t) = \mathbf{x}(t) + \dot{\mathbf{x}}(t) \Delta t + \frac{1}{2} \ddot{\mathbf{x}}(t) \Delta t^2, \quad (2.11)$$

$$\dot{\mathbf{x}}(t + \Delta t) = \dot{\mathbf{x}}(t) + \frac{1}{2} [\ddot{\mathbf{x}}(t) + \ddot{\mathbf{x}}(t + \Delta t)] \Delta t, \quad (2.12)$$

where the timestep Δt is selected.

2.1.1 Measurement of Fluid Viscosity

An important property of a fluid is the viscosity η . In the DPD framework, it depends on the interaction parameters γ , a , k , the thermal

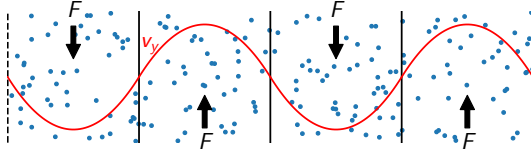


Figure 2.2: Sketch of the reverse Poiseuille flow setup. The simulation box is divided into four parts. A constant force is applied to each particle, the direction of the force alternating between the parts. The resulting parabolic flow profile is sketched by the red line. The dash line indicates periodic boundary conditions.

energy $k_{\text{B}}T$, and the number density ρ of DPD particles. η is measured using a Poiseuille flow setup, as shown in fig. 2.2. The simulation box is divided into four parts in the x -direction. A constant force is exerted on all particles, but its direction alternates between the four simulation parts, as indicated by the arrows in fig. 2.2. We choose a division into four parts to guarantee the development of the flow profile at the inner lines without interference of the applied boundary conditions.

The resulting flow profile for each of the four parts is derived from the Navier-Stokes equations and is given by

$$v_y = \frac{F\rho}{2\eta}x(H-x), \quad (2.13)$$

where v_y is the velocity in the direction of the applied force, x is the position within the box, and H is the width of each of the four simulation parts. To reduce effects of the applied boundary conditions, the profile is only measured in the two boxes in the middle of the setup. [111]

2.2 Brownian Dynamics

The DPD framework allows a high level of coarse-graining, therefore reducing the computational cost to model a fluid dramatically in comparison to a fully atomistic description. Nevertheless, the amount of computational cost might still be very high for a hydrodynamic representation. Therefore the BD method is introduced. It incorporates friction and thermal effects implicitly without explicitly modeling the fluid particles, thus significantly reducing the computational effort at the cost of losing the effects of momentum transfer within the fluid.

At the core of the BD method is again Newton's second law of motion for the simulation of particles. These particles may represent e.g. the constituting particles of cell membranes, which will be introduced in the next chapters. For a particle with position \mathbf{x} , the equation of motion is given by

$$m\ddot{\mathbf{x}} = -\gamma\dot{\mathbf{x}} + \sqrt{2\gamma k_B T}\mathbf{R}(t) + \mathbf{F}_I. \quad (2.14)$$

This equation is known as the Langevin equation. The first term on the right-hand side introduces a dissipative force with the friction coefficient γ . The second term models thermal fluctuations governed by the thermal energy $k_B T$. The random component $R(t)$ models Gaussian white noise, which fulfills the relations

$$\langle \mathbf{R}(t) \rangle = \mathbf{0}, \quad (2.15)$$

$$\langle \mathbf{R}(t) \mathbf{R}(t') \rangle = \delta(t - t'). \quad (2.16)$$

In contrast to the DPD method, the random contribution is orientated arbitrary in space and not parallel to the distance vector between two particles. The last term \mathbf{F}_I represents all other interactions that act on the simulation particles.

To obtain the BD method from the Langevin equation, we can assume the overdamped limit i.e. $m\ddot{\mathbf{x}} = \mathbf{0}$, which is a realistic assumption in biological systems. The obtained dynamics becomes

purely diffusive, if no other interactions are introduced. The Einstein-Smoluchowski relation defines the diffusion constant of a particle as

$$D = k_{\text{B}}T/\gamma. \quad (2.17)$$

Furthermore, the friction coefficient is connected to the viscosity of the implicitly modeled fluid through the Stokes equation as

$$\gamma = 6\pi\eta a, \quad (2.18)$$

where η is the viscosity and a is the effective radius of the simulated particles. To obtain the dynamics of the particles, these equations of motion are integrated in time by the Verlet algorithm.

The BD framework can be used for simulations, in which the dissipation within the fluid plays a vital role, but other hydrodynamic effects can be neglected.

2.3 Simulation Units

Parameters in numerical simulations are selected in simulation units. A number of scales may be defined, allowing to connect the simulation values to the physical parameters. In general, energy-, length- and timescales are required.

Let E be a simulation parameter with the dimension of energy. For soft matter problems, a well established energyscale is the thermal energy $k_{\text{B}}T$. The connection of the simulation parameters to the physical values is done through the dimensionless quantity

$$\frac{E^M}{(k_{\text{B}}T)^M} = \frac{E^P}{(k_{\text{B}}T)^P}, \quad (2.19)$$

where the superscript M denotes a simulation parameter and P the physical values. The physical value of E is then obtained by

$$E^P = \frac{(k_{\text{B}}T)^P}{(k_{\text{B}}T)^M} E^M \quad (2.20)$$

where only the physical quantity $(k_B T)^P$ needs to be known. For example $(k_B T)^P = 4.282 \text{ pN nm}$ for experiments at room temperature.

In the same way, lengthscaling is established as

$$x^P = \frac{D_0^P}{D_0^M} x^M, \quad (2.21)$$

where x is a value with the dimension of length and D_0 is a characteristic lengthscale. For cell simulations, the average cell diameter can be used for this purpose. Timescaling may be achieved by combining energyscale, lengthscale, and the viscosity η of surrounding fluid to obtain

$$t^P = \frac{\eta^P (D_0^P)^3 (k_B T)^M}{\eta^M (D_0^M)^3 (k_B T)^P} t^M. \quad (2.22)$$

Using the fundamental scales of energy, length, and time, other quantities can be calculated. The physical values of a force F are found as

$$\frac{F^M D_0^M}{(k_B T)^M} = \frac{F^P D_0^P}{(k_B T)^P}, \quad (2.23)$$

$$F^P = \frac{D_0^M}{D_0^P} \frac{(k_B T)^P}{(k_B T)^M} F^M. \quad (2.24)$$

This scheme is easily adapted for other quantities of interest.

In this thesis, both simulation and physical values will be used. If not stated otherwise, a quantity given in physical units refers to a transformed value as described above. If a value is given without physical dimension, it refers to a simulation or model value.

3 Cell Model

Cells fulfill a variety of tasks within any living body. Consequently, this diversity of functions and environments requires a similar amount of models to study cells (see fig. 3.1). Cell models may be divided into two major categories, which depend on the required resolution of the studied cell. Micro- and nanostructure models focus on the cytoskele-

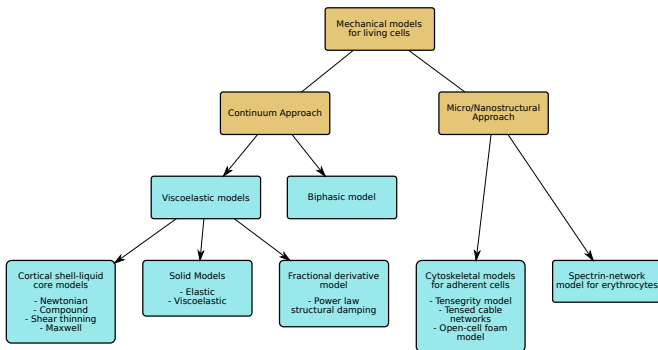


Figure 3.1: Selection of different types of models to study the properties and behavior of various cells [112–118].

tal and single filament contributions toward the cell mechanics. The developed models have been used extensively to study the mechanics of adherent cells (see [112–116]). Continuum models neglect these characteristics and treat cells as comprised material with continuous mechanical properties such as Young’s modulus and Poisson’s ratio.

These properties are derived using experimental methods and allow an effective description of bigger cell systems [118].

The particle-based cell model introduced in this chapter may be counted as a continuous cell model, where we coarse-grain the studied biological system to obtain a tractable model, that can represent whole cells on available computers. Thus, in the introduced systems, each particle does not represent single molecules or filaments, but models a discrete area or volume of a cell with homogeneous average properties of that area or volume. A drawback of the coarse-graining process is the loss of information at smaller scales. Therefore, effective potentials need to be introduced to mimic cell properties.

The aim of this chapter is to derive a coarse-grained cell model that incorporates properties of a bulk cytoskeleton and a lipid-bilayer membrane with underlying cell cortex. The model is used to study how applied mechanical stresses induce deformations of complex, cellular structures. To this end, the deformation of different structural elements of the cell is studied using a microplate compression setup. The results supply information about the interaction between cell membrane and bulk cytoskeleton.

3.1 Bulk Cytoskeleton

The usage of a coarse-grained modeling approach allows us to neglect the details of different fibers, which form a cytoskeleton and model it as an elastic, random mesh network. This network consists of a number of vertices N that are distributed within a volume V . The vertices are connected by N_S springs, which are established between direct neighbors. The network templates used in our simulations are created using TetGen [119].

The springs correspond to a harmonic potential that is given by

$$U_{\text{network}}(\{l_i\}) = \sum_{i=1}^{N_S} \frac{\lambda}{2} (l_i - l_i^0)^2, \quad (3.1)$$

where l_i is the instantaneous length of the spring i and l_i^0 is the corresponding rest length. The value λ is the spring constant, characterizing the strength of each spring. The model is implemented within the BD framework, which represents thermal fluctuations and dissipation from an implicit fluid.

The cytoskeletal material is assumed to be isotropic and its mechanic properties are described by two elastic constants. Using elastic theory, the values of Poisson's ratio ν and the bulk modulus K are established as

$$\nu = 1/4, \quad (3.2)$$

$$K = \frac{1}{9} \frac{N_S}{V} \langle \lambda (l_i^0)^2 \rangle. \quad (3.3)$$

The value of ν shows that the elastic network is compressible. Other elastic constants can be derived from ν and K . For example, the elastic or Young's modulus is given by

$$Y = \frac{1}{6} \frac{N_S}{V} \langle \lambda (l_i^0)^2 \rangle. \quad (3.4)$$

All mechanical properties can be calculated through the properties of the mesh as well as the spring constant. [120, 121]

3.1.1 Microplate Compression Setup

The elastic material properties are measured by performing microplate compression tests *in silico* [66, 122]. The modeled material is put between two rigid plates, as sketched in fig. 3.2. The upper plate is moved down toward the material with a constant velocity, leading to deformation. The engineering strain ϵ is used to quantify the deformation. It measures the relative change in height ΔD with respect to the initial height D_0 :

$$\epsilon = \frac{\Delta D}{D} = \frac{D_0 - D}{D_0}. \quad (3.5)$$

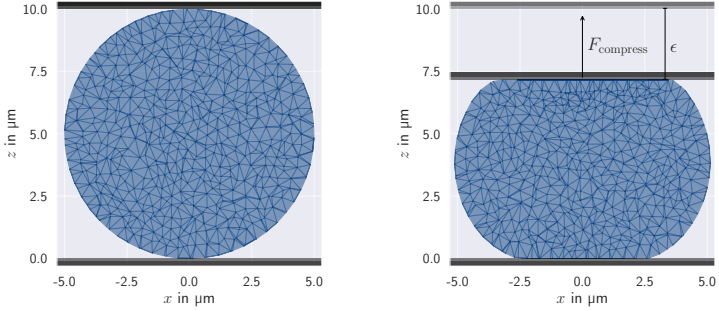


Figure 3.2: Sketch of a microplate compression experiment for a spherical elastic particle. The particle is put between two plates and the upper plate is moved down with a constant velocity. The induced deformation of the network is quantified by the engineering strain ϵ . Due to the elasticity of the material, the reaction force F_{compress} is obtained.

The microplates are represented by rigid walls, which interact with the deformed particle using the repulsive part of the Lennard-Jones (LJ) potential:

$$U_{\text{wall}}(r) = 4\epsilon_{\text{LJ}} \left[\left(\frac{\sigma}{r} \right)^{12} - \left(\frac{\sigma}{r} \right)^6 \right], \quad r \leq \sqrt[6]{2}\sigma. \quad (3.6)$$

The potential acts between the wall and the vertices of the network. A large value for the interaction energy ϵ_{LJ} and a small value for the characteristic length σ are chosen to ensure a hard wall approximation.

The LJ potential is also used to measure the reaction force F_{compress} , as the particle resists the induced deformation. The force is calculated by summing all force contributions in the compression direction from the vertices within interaction range. To overcome the effects of thermal noise, the simulation is divided into compression and measurement parts. During the first part, the cell is compressed, while during

the second part, the strain ϵ and the force F_{compress} are measured. This allows averaging over a long enough time period, leading to reliable results. At the same time, the information about time evolution is not considered, so that no timescales are used in the simulations.

3.1.2 Comparison Between Theory and Simulation

A number of simulation parameters are required to perform the microplate compression tests. The main parameters, that are constant for all simulations performed in this chapter, are summarized in table 3.1.

| Parameter | Simulation Value | Physical Value |
|-----------------|------------------|-----------------------------------|
| $k_{\text{B}}T$ | 0.0001 | $4.282 \times 10^{-21} \text{ J}$ |
| D_0 | 10 | $10 \times 10^{-6} \text{ m}$ |
| γ | 50 | |
| Δt | 0.005 | |

Table 3.1: Overview of the main simulation parameters for microplate compression tests. The thermal energy $k_{\text{B}}T$ and the average size of a particle D_0 are used as energy- and lengthscales. γ and $k_{\text{B}}T$ are required to use the BD framework. A timescale is not used on the simulations, as only quasi-static deformations are studied.

The compression tests are performed for a cubic volume of the elastic material with an initial side length of $D_0 = 10 \mu\text{m}$.

To measure Poisson's ratio ν , the strain ϵ in the compression direction as well as strains in the other directions are monitored. ν is calculated as

$$\nu = -\frac{\epsilon_x + \epsilon_y}{2\epsilon}. \quad (3.7)$$

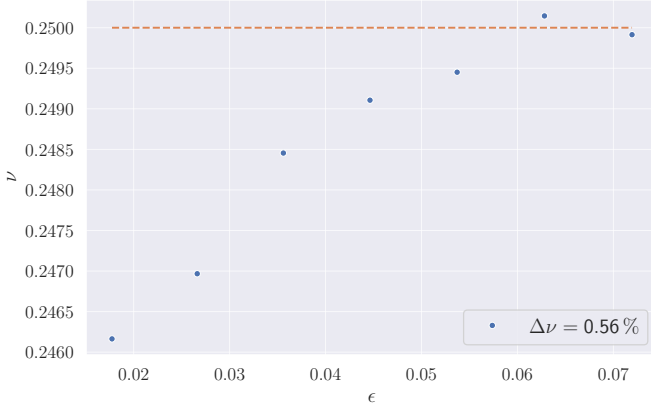


Figure 3.3: Poisson's ratio ν for a simulation setup with $N = 69\,051$ vertices and $N_S = 499\,779$ springs. The simulated values agree well with the theoretical prediction, marked by the dashed line. The deviations are a result of surface effects.

For the simulation parameters in table 3.1, the measured values of ν are shown in fig. 3.3. The average relative deviation

$$\Delta\nu = \left\langle \frac{\nu - 1/4}{1/4} \right\rangle \quad (3.8)$$

is calculated and a good agreement between the theoretical value and the simulation results is observed. The small deviations from the theoretical values are a result of surface effects, as the cubic material does not stay in the cuboid shape due to small buckling at the surface. For this reason, the applied strain needs to be lower than $\epsilon \leq 0.1$ to obtain reliable results.

Additionally, the values of the reaction force F_{compress} are computed. Young's modulus is obtained by fitting the relationship

$$F_{\text{compress}} = Y A \epsilon, \quad (3.9)$$

to the simulation data, where A is the surface area of one side of the cube. The data and the fit are shown in fig. 3.4. The relative deviation ΔY of the fitting parameter from the expected value is calculated and a good agreement between theory and simulation is observed.

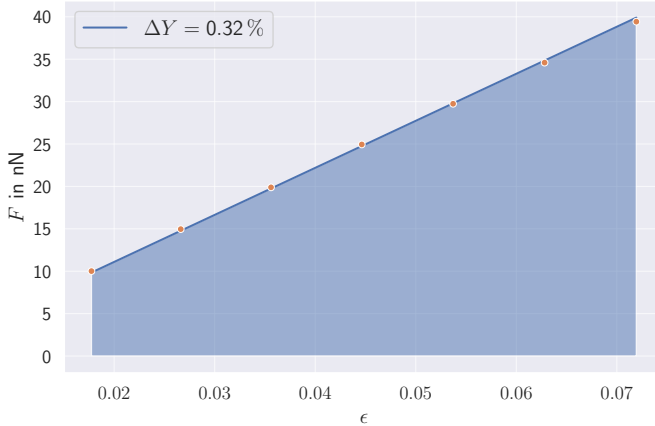


Figure 3.4: Force and strain measured for the compression of a cubic elastic network. Equation (3.9) is fitted to the data to establish Young’s modulus. A good agreement between theory and simulation is observed. As the material buckles in x - and y -direction under large stresses, only strain values of $\epsilon \leq 0.1$ can be used to obtain reliable results.

In table 3.2, the results for different levels of discretization and different values of the spring constant λ are summarized. A good agreement between simulations and theory is shown for the tested levels of discretization. For setups with less vertices, surface effects become more prominent, leading to deviations of up to 10%. However, the computational time for these setups is reduced dramatically. Choosing the best level of mesh discretization is therefore a trade off between simulation time and the correspondence of elastic properties

to the theoretical values. Additionally, smaller values of λ may have a significant effect on the quality of the results, as the network is not able to stay in its initial structure under pressure and can partially collapse.

| N | N_S | $V/\mu\text{m}^3$ | $\langle l_i^{02} \rangle / \mu\text{m}^2$ | $\lambda / \text{pN} \mu\text{m}^{-1}$ | $\Delta\nu$ | ΔY |
|--------|---------|-------------------|--|--|-------------|------------|
| 8044 | 59 943 | 1000 | 0.346 | 85.64 | 10.9 % | 10.5 % |
| 8044 | 59 943 | 1000 | 0.346 | 856.40 | 0.5 % | 9.4 % |
| 8044 | 59 943 | 1000 | 0.346 | 8564.00 | 2.0 % | 10.2 % |
| 15 625 | 115 041 | 1000 | 0.222 | 8564.00 | 0.7 % | 6.8 % |
| 29 791 | 218 050 | 1000 | 0.146 | 8564.00 | 2.0 % | 3.2 % |
| 69 051 | 499 779 | 1000 | 0.083 | 856.40 | 0.6 % | 0.3 % |
| 69 051 | 499 779 | 1000 | 0.083 | 8564.00 | 1.2 % | 0.8 % |

Table 3.2: Comparison of the elastic constants for different levels of mesh discretization and spring constants. A good agreement between simulation and theory is obtained for all listed values. Using a larger number of vertices improves the quality of the mesh but significantly increases the computational cost. For lower values of λ , the quality of the network may become poor, as the modeled material is not able to stay in cuboid shape under high pressure.

3.2 Spherical Elastic Particles

Cell shapes may differ, depending on cell type, environment, and current function. For many cells and similar constructs such as vesicles, a spherical shape is a good approximation. Therefore, we create spherical elastic particles with an initial diameter of $D_0 = 10 \mu\text{m}$ and perform compression tests.

While the geometry has no influence on the calculation of the elastic constants, it does alter the interaction between the cell and the

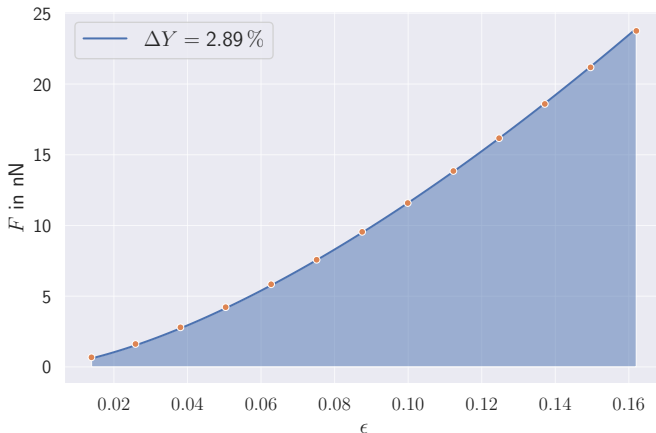


Figure 3.5: Force-strain curve for an elastic sphere for a setup with $N = 4197$ vertices and $N_S = 28\,621$ springs. The relation is non-linear and fitted with eq. (3.10), showing a good agreement between theory and simulation.

walls. To derive the relationship between strain, force and the elastic material constants, we use the ideas of the field of contact mechanics [121]. The obtained relation, known as Hertz law, is derived for the contact between an elastic sphere and two rigid, non-deformable half spaces. The force has a characteristic dependence of $\epsilon^{3/2}$ on the strain

$$F_{\text{compress}} = \frac{4Y}{3(1-\nu^2)} R_M^2 \epsilon^{3/2}, \quad (3.10)$$

where R_M is the initial radius of the sphere. This solution is only valid for small deformations, limiting the range of applicable strains for the spherical geometry.

For the parameter set in table 3.1, the measured simulation data points are shown in fig. 3.5. The simulated values are fitted with eq. (3.10), where the theoretical value of $\nu = 1/4$ is used. A good

agreement between theory and simulations is obtained for Young's modulus.

| N | N_S | $V/\mu\text{m}^3$ | $\langle(l_i^0)^2\rangle/\mu\text{m}^2$ | $\lambda/\text{pN}\mu\text{m}^{-1}$ | ΔY |
|------|--------|-------------------|---|-------------------------------------|------------|
| 4197 | 28 621 | 521 | 0.418 | 277.47 | 2.7 % |
| 4197 | 28 621 | 521 | 0.418 | 2774.74 | 2.9 % |
| 4197 | 28 621 | 521 | 0.418 | 27 747.36 | 2.7 % |
| 9608 | 63 920 | 523 | 0.244 | 277.47 | 1.2 % |
| 9608 | 63 920 | 523 | 0.244 | 2774.74 | 1.0 % |
| 9608 | 63 920 | 523 | 0.244 | 27 747.36 | 2.1 % |

Table 3.3: Measured Young's modulus for different settings and spring constants of elastic spheres. The good agreement between theory and simulation is less dependent on the discretization level than for the cubic particle, as surface effects are less critical for the spherical geometry.

We also test two different meshes and a number of spring constants λ and find a good agreement between simulations and theory. The data in table 3.3 show that the discretization level is not as important as for the cuboid, since the surface effects are partly taken into account by eq. (3.10). This allows us to use spherical cell setups with less vertices than those for cubic geometry.

3.3 Cell Membrane

The introduced elastic network models the effect of a bulk cytoskeleton. Another important building block of cells is a lipid-bilayer membrane. This membrane consists of two leaflets of lipids, that self-organize to form a thin sheet surrounding the cell (see fig. 1.1).

The membrane is modeled as a two-dimensional, spherical shell, that surrounds an elastic network. To form the membrane, a number

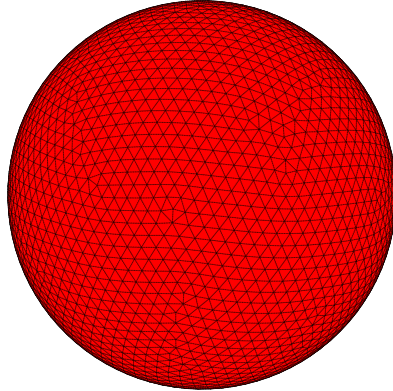


Figure 3.6: Sketch of a lipid-bilayer cell membrane model. The membrane model is a two-dimensional spherical shell, on which N^M vertices are distributed in a regular pattern. They are connected by N_S^M springs that form N_T^M triangles. The mechanics of the membrane is determined by an area constraint, a volume constraint and the bending rigidity.

of vertices N^M are distributed on this surface using a regular triangulation. These vertices are connected by N_S^M springs, that form N_T^M triangles, as depicted in fig. 3.6.

The potential energy of the membrane is given by

$$U_{\text{membrane}} = U_{\text{bending}} + U_{\text{area}} + U_{\text{volume}}, \quad (3.11)$$

where U_{area} and U_{volume} are the area and volume constraints. U_{area} penalizes a change in the surface area of the lipid bilayer, while U_{volume} ensures a constant volume within the cell. The volume constraint models an effect of an enclosed fluid, which prevents rapid volume changes. Both potentials utilize the triangles of the membrane and

are given by

$$U_{\text{area}} = k_{\text{ag}} \frac{(A - A^0)^2}{2A^0} + \sum_{i=1}^{N_T^M} k_{\text{al}} \frac{(A_i - A_i^0)^2}{2A_i^0}, \quad (3.12)$$

$$U_{\text{volume}} = k_{\text{vg}} \frac{(V - V^0)^2}{2V^0}. \quad (3.13)$$

In these equations, A and V are the instantaneous total surface area and enclosed volume of the membrane. They are obtained by summing the area and volume contributions of each triangle. The corresponding values A^0 and V^0 are targeted values of these quantities. The variable A_i represents the area of triangle i with A_i^0 being the corresponding rest value. The three constants k_{ag} , k_{al} and k_{vg} define the strength of the global area and local area constraints as well as the volume constraint.

The term U_{bending} describes the resistance of the lipid bilayer to bending of flexural deformation. It is described through the Helfrich Hamiltonian [10] whose discrete version used in the simulation model is given by

$$U_{\text{bending}} = \frac{\kappa}{2} \sum_i^{N^M} \frac{1}{\sigma_i} \left\{ \sum_{j(i)} \frac{\sigma_{i,j} \mathbf{r}_{i,j}}{r_{i,j}} \right\}^2. \quad (3.14)$$

Here, the first sum runs over all membrane vertices i , while the second sum iterates over the bonded neighbors j of i . The vector $\mathbf{r}_{i,j}$ is the bond vector between vertices i and j , with $r_{i,j} = |\mathbf{r}_{i,j}|$. The variable $\sigma_{i,j} = r_{i,j} [\cot(\theta_1) + \cot(\theta_2)]/2$ is the length of the bond vector in the dual space, with θ_1 and θ_2 being the angles of the two triangles opposite to the shared bond vector $\mathbf{r}_{i,j}$. Lastly, the factor $\sigma_i = 0.25 \sum_{j(i)} \sigma_{i,j} r_{i,j}$ is the total area of the dual cell around vertex i [123]. The parameter κ is called the bending resistance of the membrane and determines its strength.

Microplate compression tests are performed for the membrane cytoskeleton model. The force-strain data points are shown shown in

fig. 3.7. To mimic a realistic situation, the values of the cytoskeletal Young's modulus are chosen to be in a range of 1 kPa and 100 kPa, while the parameters for the membrane are chosen according to previous simulations of RBCs [124]. A fit using the Hertz Law in eq. (3.10) shows some disagreement, since the membrane contribution is not properly included.

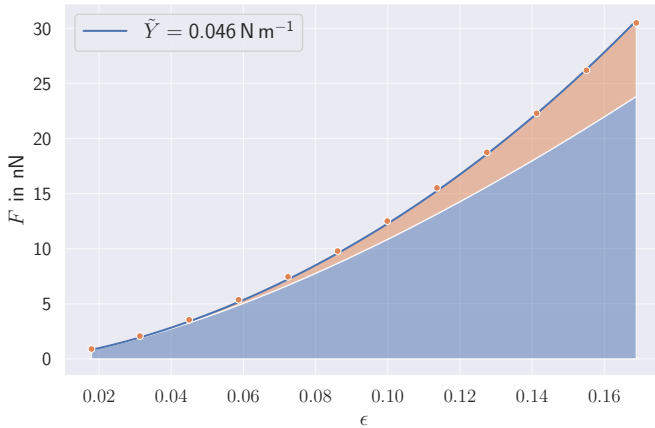


Figure 3.7: Force-strain data for a compression test with the membrane-cytoskeleton model. The data points are fitted by the sum of expressions from eq. (3.10) and eq. (3.15). This leads to a good agreement between theory and simulation. The blue-shaded area shows the contribution of the cytoskeleton, while the orange area marks the influence of the membrane. The simulation parameters for the inner network and the membrane are $Y = 9.7$ kPa, $\kappa = 70$ k_BT, $k_{\text{ag}} = 9 \times 10^{-2}$ N m⁻¹, $k_{\text{al}} = 1.8 \times 10^{-3}$ N m⁻¹ and $k_{\text{vg}} = 6 \times 10^6$ N m⁻².

The effect of the membrane to the elastic response can be described by a balloon shell, which is filled with an incompressible fluid [66, 125]. The relation is given by

$$F_{\text{compress}} = 2\pi\tilde{Y}R_M\epsilon^3, \quad (3.15)$$

where \tilde{Y} , the effective two dimensional contribution to the Young's modulus, is introduced. Fitting the data with the sum of the two expressions from eq. (3.10) and eq. (3.15) leads to a good agreement between simulated data and fit function. The blue area in fig. 3.7 marks the contribution of the bulk cytoskeleton, while the orange-shaded area gives the contribution of the membrane. The values of Y are consistent with the theoretical values given by eq. (3.9).

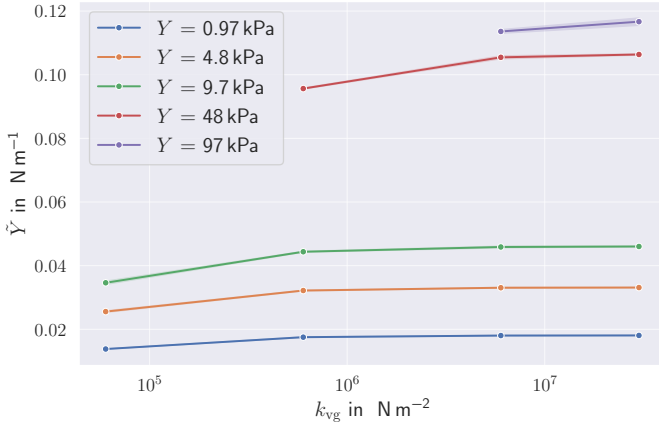


Figure 3.8: Contribution of the volume constraint characterized by k_{vg} to the membrane response \tilde{Y} . Different values of Y are marked by various colors and lead to different values of \tilde{Y} . This is an effect of the area constraint. A stable plateau is observed for high values of k_{vg} , as the volume constraint has no effect on the deformation of the cell if the cell volume is conserved. Except for k_{vg} and Y , all parameters are chosen equal to those in fig. 3.7.

The various potentials in eq. (3.11) affect the value of \tilde{Y} differently. Their effects are studied systematically by changing one value while keeping the others constant. Additionally, different values for the Young's modulus Y of the inner network are used. For all parameter sets, the value \tilde{Y} is established by combined fitting from both

eq. (3.10) and eq. (3.15).

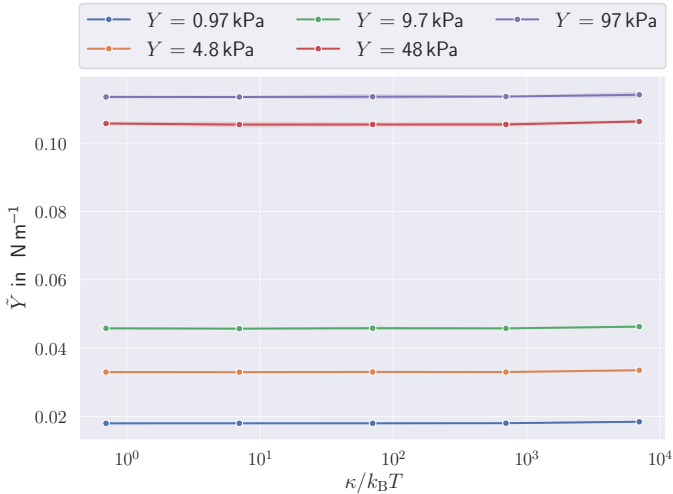


Figure 3.9: Contribution of the bending rigidity characterized by κ to the membrane response \tilde{Y} . The bending rigidity has no visible effect on the elastic response, as the deformations of the bulk cytoskeleton and the stretching of the membrane lead to significantly higher contributions. Performing simulations with values of $Y \ll 1$ kPa leads to a non-negligible effect of κ , which is not considered further. The simulation values are chosen as in fig. 3.7, except for κ and Y .

Figure 3.8 presents the results for different values of k_{vg} , where each color corresponds to a different value of Y . The distinct levels for \tilde{Y} are a result of the area constraint, as will be discussed later in this chapter. For high values of k_{vg} , \tilde{Y} reaches a stable plateau and the onset of this plateau depends on Y . This demonstrates the complex interaction between membrane and cytoskeleton. While the volume constraint tries to conserve the volume of the cell, the elastic network acts against it. For high k_{vg} , the membrane contribution dominates this relation, leading to constant values of \tilde{Y} . We conclude

that large values of k_{vg} do not affect cell deformation and ensure volume conservation of the cell.

The effect of κ on cell deformation is shown in fig. 3.9. The influence of the bending rigidity is negligible for the elastic response, which is consistent with the discussion around the derivation of eq. (3.15) in Lulevich et al. [66].

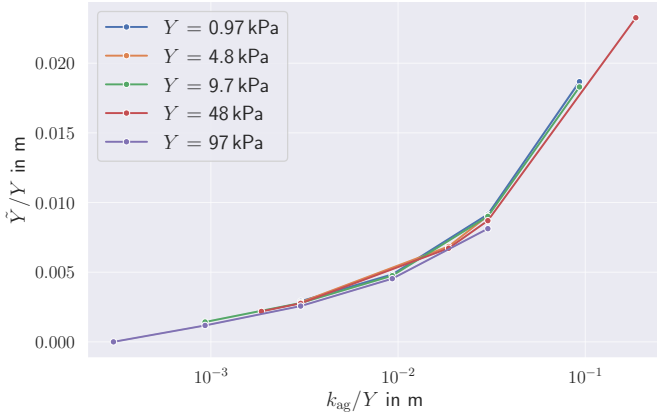


Figure 3.10: Contribution of the area constraints to the membrane response \tilde{Y} . In contrast to the volume constraint and the bending rigidity, the strength of the area constraints influences the elastic response. By rescaling both \tilde{Y} and k_{ag} by Y , all curves fall onto a master curve, showing that the relative mechanical response depends only on the ratio of area constraint contribution and the strength of the inner network.

For testing the effect of the area constraint, both parameters k_{ag} and k_{al} need to be considered. As their effect on deformation is similar, we focus on a fixed ratio of $k_{ag} = 50k_{al}$ and only vary k_{ag} in fig. 3.10. The effect of k_{ag} is significant for all shown values. By rescaling the values of \tilde{Y} and k_{ag} , the measured curves collapse onto one master curve, shown in fig. 3.10. This shows a complex interaction between

membrane and cytoskeleton, where the relative contribution of both parts is dependent on the ratio k_{ag}/Y .

3.4 Conclusions

In this chapter, we have introduced a coarse-grained, spherical model of a cell that includes elastic volume-filling cytoskeleton and a thin membrane shell. By performing microplate compression tests, we determine the contributions of both parts toward the total elastic response. We show that the inner network contributes purely elastically, while the membrane acts as a thin balloon shell.

By studying the influence of the membrane parameters on cell deformation, we determine that the volume constraint has no effect for high values of k_{vg} and the bending rigidity contribution is neglectable for cells with Young's moduli between 1 kPa and 100 kPa. Therefore, we can choose arbitrary values for these parameters without altering the mechanical properties of the cell. In contrast, the area compression moduli k_{ag} and k_{al} strongly influence the elastic response. By rescaling the data for cell deformation we show that the relative contributions of the cytoskeleton and the membrane are dependent only on the ratios k_{ag}/Y and k_{al}/Y .

The investigated effects of the different membrane potentials on cell deformations are used as a starting point for studying cell blebbing in the next chapter.

The studied model focuses on the contribution of an elastic inner network. For eukaryotic cells, the cell nucleus will effect the elastic response as well. It may be incorporated by introducing an elastic sphere within the network, which models different elastic properties (usually stiffer than the cytoskeleton). Depending on the position within the cell volume, the resulting contributions to the elastic response may differ.

The cell model incorporates the cytoskeletal contribution through a homogeneous elastic network, which is a simplification of reality.

To study the effects of various filaments and structures contributing to the elastic cell response, we need to incorporate their differences in more detail and study an inhomogeneous system. Additionally, we ignored the possibility of dynamic reorganization of the cell under pressure. This may lead to local stiffening by increasing the concentration of filaments or to a different cell-membrane-network interaction through a local change in binding. In the next chapter, we introduce a mechanism to model this interaction in more detail.

4 Stress-Induced Cell Blebbing

The adhesion between a cell membrane and the underlying structures, such as the cytoskeleton or the cortex, plays an important role for the stability and function of cells. In most cases, the adhesion between

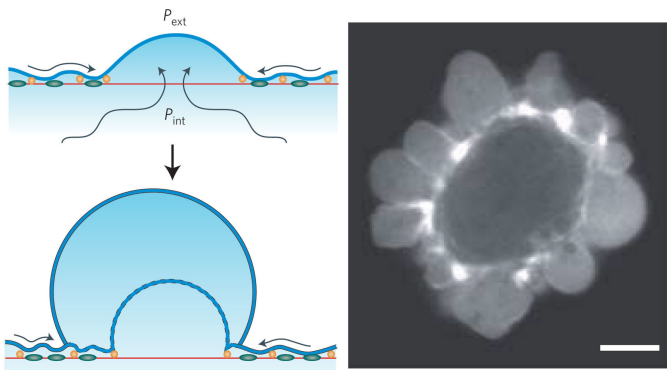


Figure 4.1: Sketch and confocal-microscopy image of cell blebbing. Left: The formation of a bleb after the cortex is ruptured locally. A pressure difference between inside and outside of the membrane generates the protrusion. Right: The shape of the membrane may be altered by such protrusions as shown in the confocal-microscopy image. Picture taken from [126] with permission and modified.

membrane and inner network is established by a number of linker molecules [127]. Depending on the type of molecules, they may have

complex kinetics of binding and unbinding over the lifetime of the cell. This dynamics can be influenced by exerted stresses due to e.g. osmotic pressure or active forces generated by molecular motors [128]. As a result, some cell membranes may form blebs, which are membrane protrusions that occur when the membrane locally detaches from the underlying network, as shown in fig. 4.1. These blebs are connected to a number of processes, such as apoptosis [67, 68], cell spreading [69], cytokinesis [70], and cell motility [71–73].

In this chapter, we discuss the mechanics of stress-induced blebbing in a complex synthetic cell, which has been observed in experiments [74]. To understand the mechanisms of blebbing, we adapt the cell model introduced in chapter 3 by allowing contraction of the cytoskeleton and a dynamic, bond-based adhesion between the membrane and the inner network. We quantify the effects of the introduced bond model as well as the membrane parameters on cell blebbing and compare simulation predictions with the experimental results.

4.1 Stress-Induced Blebbing in Synthetic Cells

Since blebbing is connected to various cell processes, different mechanisms may lead to the formation of a bleb. One example is stress-induced blebbing, which results from mechanical stress acting on the linkers between membrane and cytoskeleton. This has been observed in recent experiments with synthetic cells. These cells consist of a spherically-shaped lipid-bilayer membrane, that encapsulates a mixture of actin filaments, the cross-linking protein anillin, and the molecular motor protein myosin. Under the right conditions, the constituents of the cell self-assemble into a volume spanning actin network within the membrane as shown in fig. 4.2, where anillin provides the stability of the network by cross-linking the actin filaments.

The cytoskeletal network is anchored to the lipid-bilayer membrane through the interaction between the anillin cross-linker and *Ni-NTA*

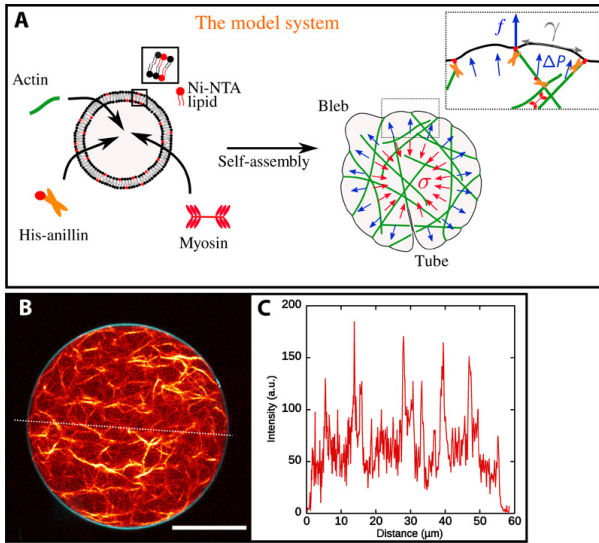


Figure 4.2: Synthetic cells consisting of a lipid-bilayer membrane and an active actin network. (A) Sketch of the model system. As a result of activity, blebs can be induced by network contraction. (B) For the right conditions and concentrations of network components, the actin and other constituents self-assemble into a volume spanning network, tightly bound to the membrane. (C) The actin is distributed over the whole diameter of the cell. Picture taken from [74] (open access) and modified.

lipids. A number of these lipids are immersed into the membrane and depending on the concentration, they allow a tight or loose binding between the inner network and the membrane. It has been shown by single-molecule experiments that the resulting connection becomes unstable under a force of a few pN [129, 130], leading to a stress-sensitive binding between the inner network and the membrane.

Due to the addition of myosin motors to the network, it may contract when the system's temperature is increased. The resulting forces

4 Stress-Induced Cell Blebbing

exerted on the membrane-cytoskeleton connection can lead to the formation of blebs, as shown in fig. 4.3. The occurrence of this effect depends on different aspects of the cells, such as the contraction strength of the network controlled by the myosin motor concentration and the number of *Ni-NTA* lipids within in the membrane.

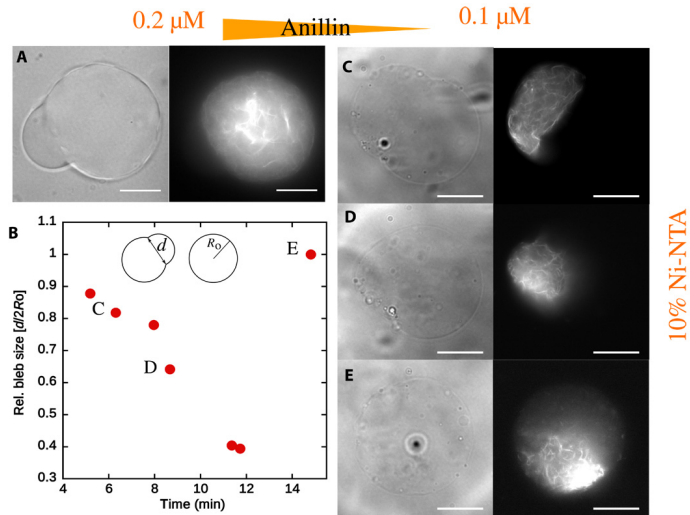


Figure 4.3: Formation of stress-induced blebs. (A) For a large anillin to myosin ratio, a stable protrusion forms. This bleb is stable over time. (B-E) For lower anillin to myosin ratios, the contractility of the network is stronger and the network shrinks until it detaches completely from the membrane, restoring its spherical shape. Picture taken from [74] (open access) and modified.

When blebbing is observed, different dynamics can emerge, moderated by e.g. the cross-linker anillin. Depending on its concentration, the stability of the inner network is altered. For a large concentration, a stable and permanent bleb is formed, since the cytoskeleton cannot shrink below a certain size (see fig. 4.3, (A)). For lower values

of the anillin concentration, the network may disassemble completely, leading to a permanently growing bleb over time (see fig. 4.3, (B-E)). [74]

In this chapter, we investigate the formation of the observed blebbing using a simulation approach based on the cell model introduced in the previous chapter. The main aim is to quantify the effects of different building blocks of the synthetic cells, such as the number of binding sites and the strength of the contracting network, on the blebbing process.

4.2 Simulation Model of Cell Blebbing

We start with the cell model introduced in chapter 3 and add the ability of the inner network to contract as well as a dynamic adhesion between the inner network and the cell membrane. This adhesion is mediated by a number of bonds, as sketched in fig. 4.4. These bonds can form and dissociate dynamically and are sensitive to stress, allowing the formation of blebs. The model is immersed in the BD framework that accounts for the viscous damping effects and thermal fluctuations from a surrounding fluid.

4.2.1 Contractile Inner Network

The elastic network is modeled through a number of vertices N , which are connected by N_S springs. To add contractile behavior, the potential energy of these springs is given by

$$U_{\text{network}}(l_1, \dots, l_{N_S}) = \sum_{i=1}^{N_S} \frac{\tilde{\lambda}_C}{2} (l_i - cl_i^0)^2, \quad (4.1)$$

where $\tilde{\lambda}_C$ is the spring constant for a single bond and c is the contractile factor. This factor is within the range $c \in [0, 1]$ and allows to shorten the rest length of each network spring. If $c = 1$, the network

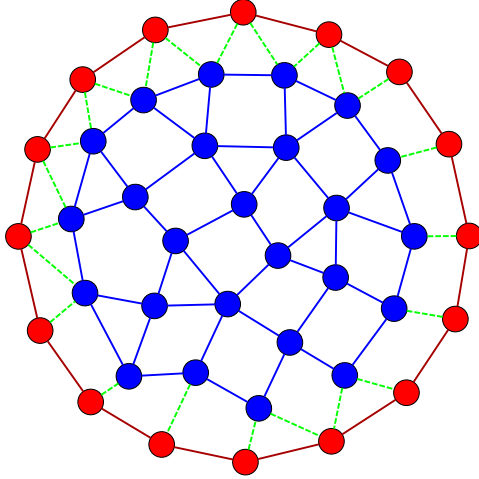


Figure 4.4: Schematic of the model to study cell blebbing. The membrane (red) behaves as described in the previous chapter, while the inner network can contract to mimic the effect of myosin motors. The membrane and inner network are not permanently bound to each other, but interact through a number of bonds (green) that can form and dissociate dynamically.

shows no contraction, but for $c < 1$, a contractile force is applied, as the springs contract toward their new rest lengths.

To quantify the effect of contraction on the whole network, we replace eq. (4.1) by a potential that is dependent only on network variables. As the employed geometry is spherical, a radius dependent potential,

$$U_{\text{network}}(R) = \frac{\lambda_C}{2} (R - cR_C^0)^2, \quad (4.2)$$

is chosen as ansatz, where R is the instantaneous radius of the network and R_C^0 is the initial radius. We introduce λ_C to be the total

spring constant of the spherical network. A coordinate transformation cannot alter the potential energy, so that

$$U_{\text{network}}(R) \stackrel{!}{=} U_{\text{network}}(l_1, \dots, l_{N_S}) \quad (4.3)$$

must hold. Assuming $R = R_C^0$ and $l_i = l_i^0$ for all springs, which is true at the beginning of the contraction process, eq. (4.3) becomes

$$\frac{\lambda_C}{2} (1-c)^2 (R_C^0)^2 = \frac{\tilde{\lambda}_C}{2} (1-c)^2 \sum_{i=1}^{N_S} (l_i^0)^2 \quad (4.4)$$

$$\Leftrightarrow \lambda_C = \tilde{\lambda}_C \sum_{i=1}^{N_S} (l_i^0)^2 / (R_C^0)^2 \quad (4.5)$$

$$\Leftrightarrow \lambda_C = \tilde{\lambda}_C N_S \langle (l_i^0)^2 \rangle / (R_C^0)^2, \quad (4.6)$$

where the effective spring constant is dependent on details of the network simulation setup as well as on the spring constant $\tilde{\lambda}_C$. With the volume of the network given by

$$V = \frac{4}{3}\pi (R_C^0)^3 \quad (4.7)$$

and eq. (3.9), the spring constant λ_C can be related to the previously discussed Young's modulus Y as

$$\lambda_C = 8\pi R_C^0 Y. \quad (4.8)$$

The entire elastic network reacts to the shortening of the springs by the contraction factor c through reducing its rest radius R_C^0 by the same factor. Therefore, we obtain a controllable contraction mechanism for the inner network. From the potential energy, we establish the surface force as $F = -\partial/\partial R U$:

$$F_C(R) = -\lambda_C (R - cR_C^0). \quad (4.9)$$

This force is directed from the surface of the inner network to its core.

While c is well defined by eq. (4.1), its interpretation is counterintuitive, since a value of $c = 1$ corresponds to a stress-free system, while $c = 0$ results in a system, which contracts toward a single point. We therefore redefine the contraction C as

$$C := 1 - c, \quad (4.10)$$

for this scale to be reversed.

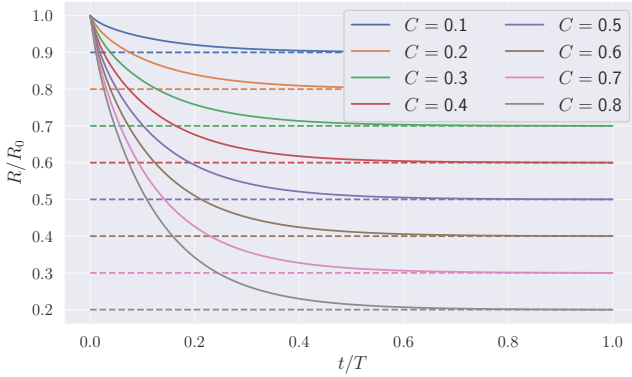


Figure 4.5: Measurement of the inner network radius R over the course of different simulations. As a result of the large amount of bonds, the dynamics of the spherical surface is complex, but it converges to the predicted rest state $R = (1 - C)R_C^0$.

Simulations are performed using the elastic network contracted by various values of C . The main simulation parameters are summarized in table 3.1. The data in fig. 4.5 show the instantaneous cytoskeleton radius R over the simulation time T . As the dynamics of network vertices is complex due to the large number of coupled springs, the time evolution may only be obtained numerically. For each value of C , the radius approaches the rest state given by $R = (1 - C)R_C^0$, as predicted by the potential energy.

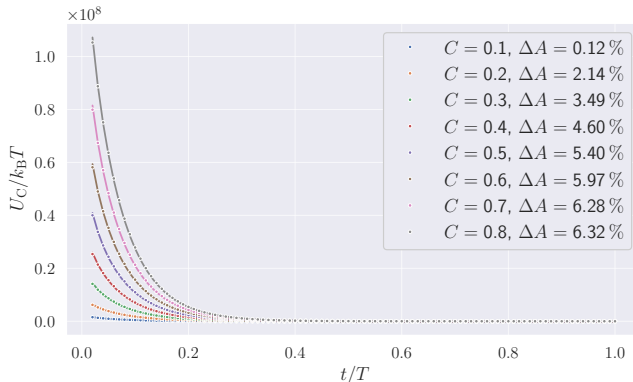


Figure 4.6: Comparison between the potential energies of a contracting network calculated by eq. (4.1) (points) and eq. (4.2) (lines). We observe a good agreement between both equations, which confirms the generality of the derived effective spring constant λ_C .

The established relation for λ_C is verified by measuring the potential energy stored in the inner network over the course of a simulation using eq. (4.1). Using the following constant

$$A = \lambda_C / \tilde{\lambda}_C, \quad (4.11)$$

eq. (4.2) is fitted to the simulated data and the fitting parameter is compared to the theoretical value of A given by eq. (4.6). A good agreement between theory and simulations is obtained, but it depends on the contraction level C . For large values of C , small defects in the network are more pronounced due to the high forces whose effect does not fully disappear through the applied averaging of the total network.

Both measurements confirm that the introduced mechanism contracts the network in a controllable way. This is an important aspect for the remainder of this chapter, as it permits a further theoretical analysis of the cell blebbing problem.

4.2.2 Membrane-Cytoskeleton Interaction

For stress-induced cell blebbing, the membrane locally detaches from the inner network as a result of the applied tension. To model this adhesion between the membrane and the inner network, they are connected via dynamic harmonic springs, as depicted in fig. 4.7. These

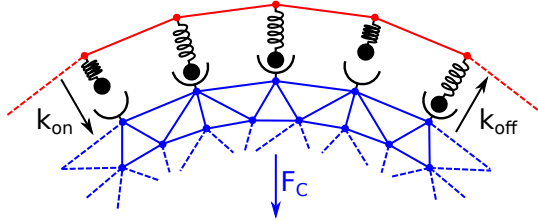


Figure 4.7: Two-dimensional sketch of the interaction between the membrane (red) and the inner network (blue). They interact through harmonic springs which can associate and dissociate. This process is stochastic and depends on the rates k_{on} and k_{off} . To model slip-bond behavior, k_{off} increases with an increase of tension. Therefore, the connection is sensitive to the applied contraction force F_C .

bonds can associate and dissociate dynamically between the vertices of the membrane and the inner network over the course of a simulation. Note that the bonds are force sensitive.

The potential energy and the force of each spring are given by

$$U_I(l) = \frac{\lambda_I}{2} (l_0 - l)^2, \quad (4.12)$$

$$F_I(l) = \lambda_I (l - l_0), \quad (4.13)$$

where λ_I is the spring constant of a bond, l_0 is the rest length and l is the instantaneous length.

To model association and dissociation, each bond can have two states: bound and unbound. Bonds can only be formed between a

vertex on the membrane surface and a vertex of the inner network, as depicted in fig. 4.7. The transition between the two states is governed by the association- or on-rate k_{on} and the dissociation- or off-rate k_{off} , that determine the number of events per unit time:

$$k_{\text{on}} = k_{\text{on}}^0, \quad (4.14)$$

$$k_{\text{off}} = k_{\text{off}}^0 \exp\left(\frac{F_I}{F_B}\right). \quad (4.15)$$

While the on-rate is chosen to be constant, the off-rate is used to model slip behavior. Hence, the lifetime $\tau = 1/k_{\text{off}}$ of a formed bond decreases with increasing tension. The tension is measured by the internal force F_I of the spring and the lifetime decreases exponentially, depending on the force scale F_B . This phenomenological ansatz used by Bell [75] has been justified by the theoretical treatment [131–133] of modeling thermally assisted escape from a metastable state [25]. As these transition rates break detailed balance, the resulting system becomes an active system.

4.3 Cell Blebbing Results

Simulations are performed using the introduced cell model. While a number of parameters are varied to study the effects of the membrane properties and the bond model on cell blebbing throughout this chapter, several main parameters are kept constant. They are summarized in table 4.1, top part.

For a general impression about the simulated blebbing process, we choose a simulation setup with $N = 1000$ membrane vertices and fixed values of λ_I , λ_C , k_{on}^0 , k_{off}^0 , F_B , and of the membrane parameters κ , k_{vg} , k_{ag} , and k_{al} . Their values are summarized in table 4.1. For this parameter set, simulations are performed with various values of C . Figure 4.8 shows snapshots from three simulations at different times

| Parameter | Simulation Value | Physical Value |
|--------------------|------------------|--|
| $k_B T$ | 0.0001 | 4.282×10^{-21} J |
| D_0 | 10 | 10×10^{-6} m |
| γ | 5 | |
| Δt | 0.001 | |
| λ_C | 1293.24 | 5.53×10^4 pN μm^{-1} |
| λ_I | 1.62 | 69 pN μm^{-1} |
| k_{on}^0 | 10.0 | |
| k_{off}^0 | 0.01 | |
| F_B | 0.333 | 14 pN |
| κ | $35 k_B T$ | 1.5×10^{-19} N m |
| k_{ag} | 34.02 | 1.46×10^{-3} N m $^{-1}$ |
| k_{al} | 0.68 | 2.9×10^{-5} N m $^{-1}$ |
| k_{vg} | 14000 | 6×10^5 N m $^{-2}$ |

Table 4.1: Overview of the main simulation parameters for cell blebbing simulations. The thermal energy $k_B T$ and the average diameter of a RBC D_0 are used as energy- and lengthscales. γ and $k_B T$ are required for the use of the BD framework. The dimensionless timescale $\tau = tk_{\text{off}}^0$ is introduced later in the chapter. The second part of the table summarizes the parameters relevant to the adhesion process, while the last part of the table summarizes the cell membrane parameters.

characterized by the dimensionless time τ , given by

$$\tau = tk_{\text{off}}^0. \quad (4.16)$$

As it will become clear later in this section, τ is the appropriate timescale for the cell blebbing problem. To visualize the interior of the cell, the snapshots in fig. 4.8 are two-dimensional slices through the three-dimensional cells. For a better visual comparison of different snapshots, the cells are rotated using the gyration tensor, such that a bleb is aligned along the x -direction.

The shown time series are representative examples of three possible

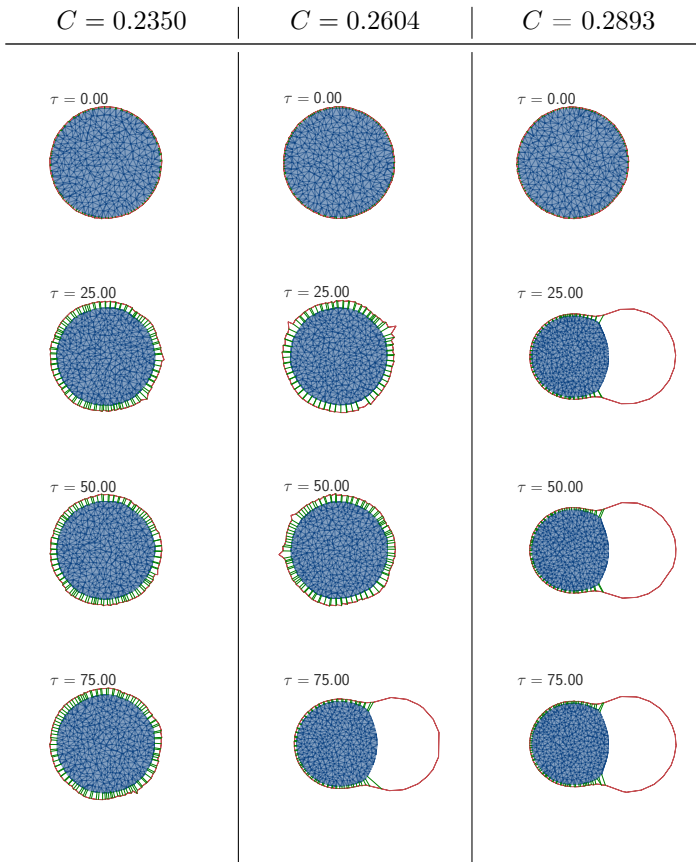


Figure 4.8: Time series for different values of C . Depending on the level of contraction, the cell can show a stable behavior (left row), blebbing with a late onset (middle), or nearly instantaneous blebbing (right).

systems. For $C = 0.2350$, the connection between the membrane and cytoskeleton does not rupture during the simulation time. This type of configuration is referred to as stable or unblebbed further in the text.

While the overall connection is stable, local deformations may be seen at the membrane surface. These result from thermal fluctuations, the applied stress, as well as from stochastic transitions between bound and unbound states for the connection bonds.

The second example in fig. 4.8 shows a blebbing transition, as the membrane disconnects from the inner network for a larger value of $C = 0.2604$. The transition is not instantaneous and occurs during the last quarter of the simulation. Before this transition, the bonds between the inner network and the membrane balance the applied contraction stress, resulting in stronger deformations of the membrane than for $C = 0.2350$. The sharp spikes are due to the two-dimensional representation and the discrete, particle-based cell model. In three dimensions, the deformations are smoother due to the applied bending rigidity.

For a value of $C = 0.2893$, the blebbing transition occurs very fast and the cell remains in the blebbed state for the rest of the simulation time. Here, the applied tension is released through the blebbing and the inner network relaxes to its minimum energy state.

Each of the configurations in fig. 4.8 is the result of one simulation. To obtain reliable information about the onset of blebbing, a number of simulations, usually between 10 and 20, are performed for every parameter set. While these simulations may differ slightly, e.g. in the blebbing time, they generally show quite similar behavior and shapes.

To identify a blebbed configuration, the bleb volume V_{bleb} is introduced as an order parameter. It is defined as

$$V_{\text{bleb}} = V_{\text{mem}} - V_{\text{cyto}}, \quad (4.17)$$

where V_{mem} is the volume of the membrane and V_{cyto} is the volume of the cytoskeleton. The bleb volume is zero in the unblebbed case and greater than zero when the cell is blebbed. For the parameter set in table 4.1, the bleb volume is measured as a function of C in fig. 4.9, where every data point corresponds to the average of all simulations performed. The shadow indicates the 95% confidence interval of the measurements.

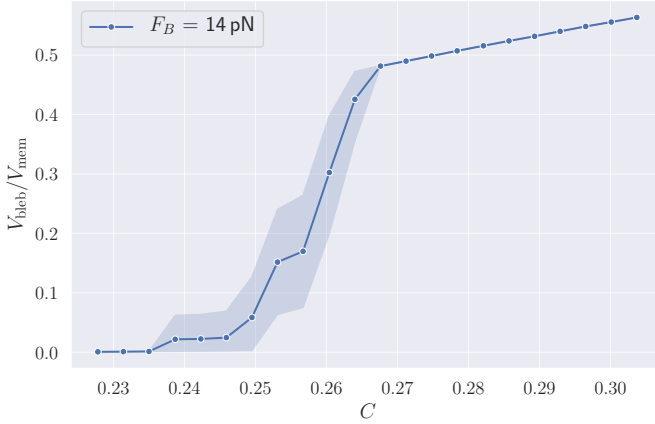


Figure 4.9: Blebbing transition measured through the bleb volume. To characterize the blebbing transition, the bleb volume is measured for each independent simulation and a number of simulations are averaged. The transition between non-blebbed and blebbed states is fast and corresponds to a contraction value that depends on the simulation parameters, especially on those of the interaction model.

The data indicate that the transition between non-blebbed and blebbed states is nearly instantaneous when the contraction value is larger than a critical value $C_{\text{crit}}^{\text{meas}}$. Beyond this critical value, blebbing is possible but is not always guaranteed, as shown by the confidence interval. This situation refers to the second case shown in fig. 4.8, as in this case the average waiting time before blebbing varies. For high enough values of C , the blebbing transition always occurs, leading to stable values for the bleb volume.

The results in fig. 4.9 show the transition for one parameter set. Clearly, the blebbing transition may occur at different contraction values when simulations are performed with various parameter sets. In the next section, we derive a theoretical prediction for the blebbing

transition depending on the simulation parameters.

4.3.1 Theoretical Prediction of the Blebbing Onset

We use a mean-field approach to predict the onset of the blebbing transition. This approach has been used extensively to study the adhesion between cells, where the cells are modeled as two rigid surfaces which are separated by a constant force [75, 134].

We start with the following rate equation

$$\frac{dN'}{dt} = -N'k_{\text{off}}^0 \exp\left(\frac{F_{\text{I}}}{F_B N'}\right) + k_{\text{on}}^0 (N^M - N'), \quad (4.18)$$

where N' is the instantaneous number of bonds which are formed between the membrane and cytoskeleton and F_{I} is the total force acting on N' bonds. The other variables are the parameters of the bond interaction as introduced before. The first term on the right hand side gives the rate of bond reductions as a result of the off rate and the applied stress, while the second term describes the growth of bonds being formed. We limit the number of bonds for every vertex to 1. Thus, only N^M bonds can be formed in total.

Dividing eq. (4.18) by k_{off}^0 gives us a dimensionless rate equation with the dimensionless timescale τ , which is used in this chapter. Furthermore, the dimensionless value $\phi = k_{\text{on}}^0/k_{\text{off}}^0$ appears, representing the binding-unbinding ratio without applied stress.

Before blebbing occurs, we observe a stable tug-of-war process between the contracting inner network and the connecting bonds. Thus, we are interested in the steady state, simplifying the equation to

$$0 = -N' \exp\left(\frac{F_{\text{I}}}{F_B N'}\right) + \phi (N^M - N'). \quad (4.19)$$

The total force acting on the bonds is given by summing up the

contributions from all formed bonds

$$F_I = \lambda_I \sum_{i=1}^{N'} (l_i - l_i^0) \quad (4.20)$$

$$= \lambda_I N' (\langle l_i \rangle - \langle l_i^0 \rangle), \quad (4.21)$$

where the sum over all bonds is replaced by the average. To obtain an equation that depends only on the radius of the inner network R , $\langle l_i \rangle$ needs to be expressed in terms of this radius. In fig. 4.10, all radii, which describe the (spherical) cell, are sketched. The membrane

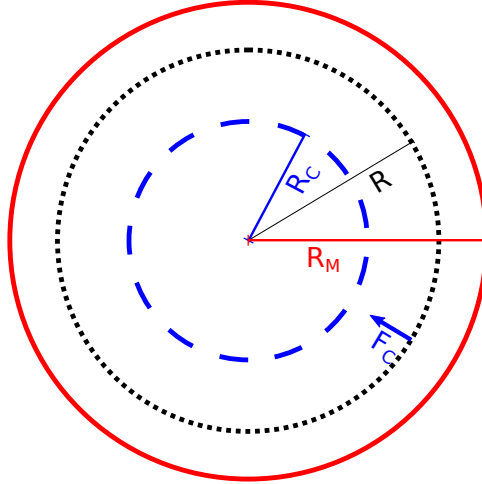


Figure 4.10: Sketch of the relevant radii within a cell model. R is the instantaneous radius of the inner network, R_C is the target radius of the inner network, depending on C . R_M is the radius of the membrane. As a result of a strong volume constraint, R_M remains constant as long as the cell is spherical.

radius is constant as a result of the applied volume constraint, as long

as the cell remains spherical. Since bonds are formed between the membrane and the inner network, the average bond length can be replaced by

$$\langle l_i \rangle = R_M - R, \quad (4.22)$$

which leads to the relation

$$F_I(R) = \lambda_I N' (R_M - R - \langle l_i^0 \rangle) \quad (4.23)$$

$$= \lambda_I N' (R_C^0 - R), \quad (4.24)$$

where we find the initial radius of the cytoskeleton R_C^0 again. Using this equation, we can express the total force applied to the connection bonds as a function of the instantaneous number of bonds N' , the instantaneous radius R of the cytoskeleton and other simulation parameters.

To obtain an equilibrium state of force balance, the contraction force F_C and the force exerted on the connection bonds F_I need to cancel each other:

$$F_I + F_C = 0 \quad (4.25)$$

$$\Leftrightarrow \lambda_I N' (R_C^0 - R) = \lambda_C (R_C^0 (1 - C) - R) \quad (4.26)$$

$$\Leftrightarrow R = R_C^0 \frac{\lambda_C (1 - C) + \lambda_I N'}{\lambda_C + \lambda_I N'}. \quad (4.27)$$

Note that the radius R depends on the instantaneous number of bonds N' , which is governed by the rate equation (4.19). To test eq. (4.27), simulations are performed without unbinding with $k_{\text{off}}^0 = 0$, so that $N' = N^M$ is guaranteed. For different ratios of $\lambda_I N^M / \lambda_C$, the resulting radius R is shown in fig. 4.11 as a function of the applied contraction C .

Without any free parameters, a good agreement between the simulation data and the theoretically predicted radii is observed, so that

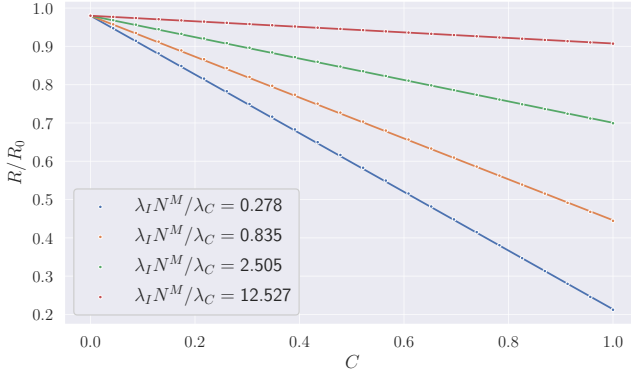


Figure 4.11: Instantaneous radius R for contracted cells without unbinding (i.e. $k_{\text{off}}^0 = 0$) as a function of the contraction C . The data points are obtained by simulations, while the solid lines are given by eq. (4.27). A very good agreement is observed without any free parameters, justifying the assumptions made.

we can use eq. (4.27) to obtain the two forces

$$F_I = \lambda_I R_C^0 N \left(1 - \frac{\lambda_C (1 - C) + \lambda_I N'}{\lambda_C + \lambda_I N'} \right), \quad (4.28)$$

$$F_C = \lambda_C R_C^0 \left((1 - C) - \frac{\lambda_C (1 - C) + \lambda_I N'}{\lambda_C + \lambda_I N'} \right). \quad (4.29)$$

If eq. (4.28) is inserted into eq. (4.19), the resulting equation still involves two variables, namely the contraction C and the number of bonds N' . If we know the contraction, we can obtain the average number of bonds. Additionally, for the case of two rigid plates, which are separated by a constant force, a critical force was derived by Bell

[75] at which the connection develops a cascading instability:

$$F_{\text{crit}} = F_B N^M \text{pln}(\phi/e). \quad (4.30)$$

Here, the product logarithm $\text{pln}(a)$ is the solution of $x \exp x = a$, similar to the definition of the natural logarithm $\ln a$ as the solution of $\exp x = a$.

To use this relation, the constant separating force needs to be replaced by the contractile force F_C that shrinks the inner network. It leads to a second relation

$$F_{\text{crit}} = F_C \quad (4.31)$$

$$\Leftrightarrow F_{\text{crit}} = \lambda_C R_C^0 \left((1 - C_{\text{crit}}) - \frac{\lambda_C (1 - C_{\text{crit}}) + \lambda_I N'_{\text{crit}}}{\lambda_C + \lambda_I N'_{\text{crit}}} \right) \quad (4.32)$$

$$\Leftrightarrow N'_{\text{crit}} = \frac{\lambda_C F_{\text{crit}}}{\lambda_I \lambda_C R_C^0 C_{\text{crit}} - \lambda_I F_{\text{crit}}} \quad (4.33)$$

between C_{crit} and N'_{crit} that is plugged into eq. (4.19). The resulting equation is non-linear and cannot be solved analytically. Therefore, we use Sympy [135] and its implementation of the secant method to solve the equation for the critical contraction $C_{\text{crit}}^{\text{theo}}$. This solution gives us the predicted contraction, at which we expect the blebbing transition to take place. For a fixed geometry, as used in this chapter, $C_{\text{crit}}^{\text{theo}}$ is dependent only on the parameters of the bond model:

$$C_{\text{crit}}^{\text{theo}} = C_{\text{crit}}^{\text{theo}}(N^M, R_C^0, \lambda_C, \lambda_I, \phi, F_B). \quad (4.34)$$

4.3.2 Results for Rigid Membranes

To verify the theoretical arguments for $C_{\text{crit}}^{\text{theo}}$, simulations are performed with a rigid spherical shell which neither moves nor fluctuates, preventing any contribution of the outer shell to the detachment of the inner network. The inner network and the connection bonds are

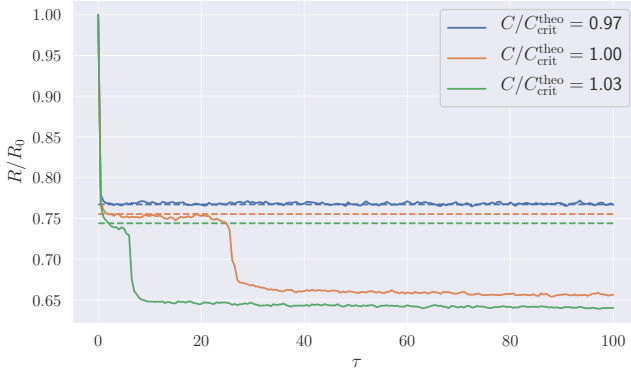


Figure 4.12: Instantaneous radius R as a function of the simulation time τ for cells with rigid membranes and different contractions. Solid lines are the results of the simulations, while dashed lines correspond to the equilibration radius as calculated by eq. (4.27) for the applied contraction. Different colors mark different values of C , normalized by $C_{\text{crit}}^{\text{theo}}$. The stability of the simulated configurations is quantified by the equilibration time τ_{equi} that measures how long the simulated radius and its theoretical value match. If $\tau_{\text{equi}} \approx \tau_{\text{max}}$ (i.e. maximum simulation time), the system is considered stable.

modeled as introduced. For the parameter set in table 4.1, the instantaneous radius R as a function of the simulation time τ is shown in fig. 4.12 for different values of C . The contraction values are normalized by $C_{\text{crit}}^{\text{theo}}$, such that blebbing is expected for $C/C_{\text{crit}}^{\text{theo}} \geq 1$ which is the case for the data in fig. 4.12. Furthermore, a good agreement between the simulation data and the theoretical equilibrium radius given by eq. (4.27) is observed for the case of no blebbing.

To quantify the blebbing behavior, the equilibration time τ_{equi} is introduced as an order parameter. It measures the timespan, during which R is equal to the theoretical value. For $\tau_{\text{equi}} \approx \tau_{\text{max}}$ (i.e.

maximum simulation time), the system is stable and does not show blebbing over the course of the simulation. For lower values, the blebbing transition is observed. We measure τ_{equi} in each simulation and average it for configurations with the same parameters. In fig. 4.13, the blebbing results are shown for the parameters given in table 4.1 but three different values of F_B . To compare the results, the values of C are normalized by the respective value of $C_{\text{crit}}^{\text{theo}}$ and the expected blebbing transition is marked by the dashed line.

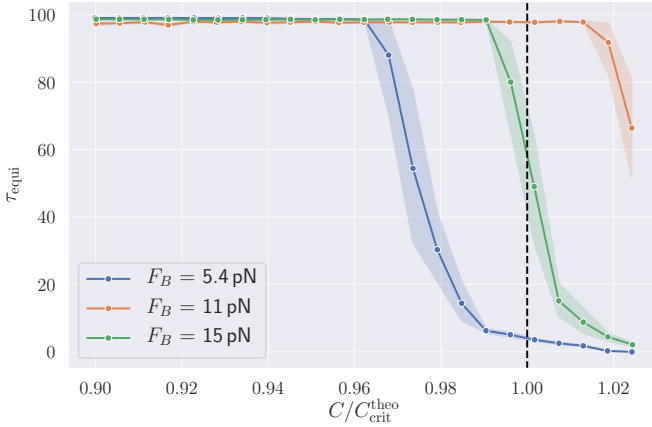


Figure 4.13: Average equilibration time τ_{equi} as a function of applied contraction. For the comparison of the results, the contractions are normalized by the corresponding values of $C_{\text{crit}}^{\text{theo}}$. Blebbing is expected to happen for $C/C_{\text{crit}}^{\text{theo}} = 1.0$, which is a good approximation for all shown configurations. Small deviations for the blebbing onset from the theoretical results are mostly due to the sensitivity of the connecting bonds to various fluctuations.

We define a blebbing transition point $C_{\text{crit}}^{\text{meas}}$ as the contraction value, at which blebbing occurs, i.e. $\tau_{\text{equi}} < \tau_{\text{max}}$. In general, a good agreement between the predicted and simulated transition points is ob-

served. Depending on the parameter set, small deviations from the theoretically predicted values are observed. These deviations are the result of fluctuations (thermal, binding-unbinding) and other perturbations such as mesh errors, which are emphasized differently depending on the simulation parameters. To average out these differences, a number of parameter sets are simulated, summarized in the top part of fig. 4.14. The values of $C_{\text{crit}}^{\text{meas}}$ are measured and plotted against the theoretical values of $C_{\text{crit}}^{\text{theo}}$ in the bottom part of fig. 4.14.

| N^M | $\lambda_C/\text{pN } \mu\text{m}^{-1}$ | $\lambda_I/\text{pN } \mu\text{m}^{-1}$ | ϕ | F_B/pN | $C_{\text{crit}}^{\text{theo}}$ | $C_{\text{crit}}^{\text{meas}}$ |
|-------|---|---|--------|-----------------|---------------------------------|---------------------------------|
| 1000 | 5.54×10^4 | 69.4 | 1000 | 14.27 | 0.460 | 0.440 |
| 1000 | 5.54×10^4 | 69.4 | 1000 | 8.56 | 0.276 | 0.266 |
| 1000 | 1.11×10^5 | 69.4 | 1000 | 15.29 | 0.369 | 0.367 |
| 1000 | 1.11×10^5 | 69.4 | 1000 | 12.23 | 0.295 | 0.299 |
| 1000 | 1.11×10^5 | 69.4 | 1000 | 10.70 | 0.258 | 0.263 |
| 1000 | 1.11×10^5 | 104.1 | 1000 | 10.70 | 0.201 | 0.199 |
| 1000 | 1.11×10^5 | 104.1 | 1000 | 8.56 | 0.161 | 0.158 |
| 1000 | 1.11×10^5 | 104.1 | 1000 | 7.14 | 0.134 | 0.132 |
| 1000 | 1.11×10^5 | 138.7 | 1000 | 28.55 | 0.460 | 0.440 |
| 1000 | 1.11×10^5 | 138.7 | 1000 | 23.79 | 0.384 | 0.367 |
| 1000 | 1.11×10^5 | 138.7 | 1000 | 21.41 | 0.345 | 0.330 |
| 3000 | 8.89×10^4 | 69.4 | 1000 | 5.35 | 0.248 | 0.240 |
| 3000 | 1.78×10^5 | 104.1 | 1000 | 14.27 | 0.369 | 0.357 |
| 3000 | 1.78×10^5 | 104.1 | 1000 | 7.14 | 0.185 | 0.183 |

Table 4.2: Measured values of $C_{\text{crit}}^{\text{meas}}$ compared to their theoretically predicted values $C_{\text{crit}}^{\text{theo}}$ for rigid cell membranes. The simulation parameters shown above as well as parameters in table 4.1 are used.

The data points are fitted with the proportionality relationship

$$C_{\text{crit}}^{\text{meas}} = \alpha C_{\text{crit}}^{\text{theo}}, \quad (4.35)$$

in which α represents the correspondence between simulations and theory. For the simulations with a rigid membrane, α deviates by 2.2 %

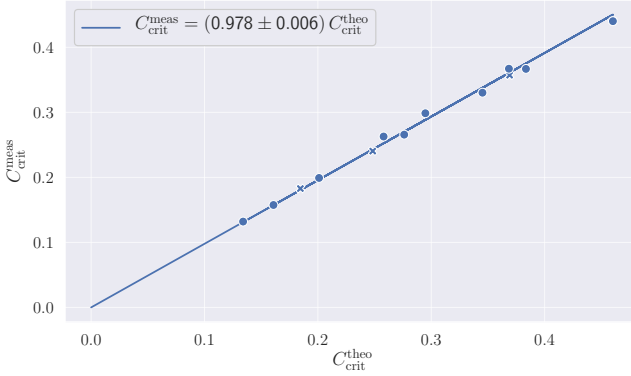


Figure 4.14: Measured values of C_{crit}^{meas} compared to their theoretically predicted values C_{crit}^{theo} for rigid cell membranes. The data points in table 4.2 are fitted using eq. (4.35), where α defines the correspondence between simulations and theory. α differs from the expected value by 2.2%, which is a good agreement. The simulation parameters shown above as well as parameters in table 4.1 are used.

from the theoretical prediction, indicating a very good agreement. Therefore, we conclude that the proposed theoretical prediction for C_{crit}^{theo} works well for rigid spherical membranes.

4.3.3 Results for Flexible Membranes

A similar analysis is performed for cells using the full membrane model from eq. (3.11), which includes bending rigidity as well as the area and volume constraints. In fig. 4.15, the results for τ_{equi} are shown for three configurations with different values of F_B , and otherwise for the same simulation parameters given in table 4.1. The values of C are normalized by corresponding values of C_{crit}^{theo} for every set.

The curves in fig. 4.15 are grouped together in a similar way as the results for a rigid membrane in fig. 4.13 using the same normalization. Simulations with flexible membranes also show that the instability of the bond connections leads to the onset of blebbing. However, the results in fig. 4.15 are not grouped around $C/C_{\text{crit}}^{\text{theo}} = 1$ due to effects of the membrane on the blebbing transition, since the membrane properties are not captured by eq. (4.34).

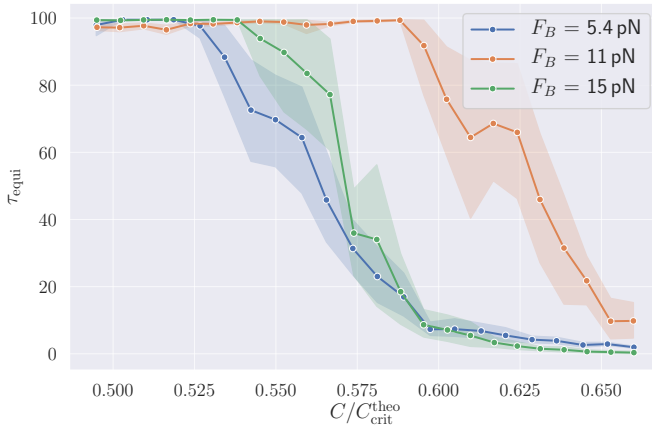


Figure 4.15: Average equilibration time τ_{equi} as a function of the applied contraction for flexible cell membranes. As a result of the normalization by the corresponding $C_{\text{crit}}^{\text{theo}}$, the curves are grouped together. In contrast to the results of rigid cell membranes, the grouping is not around $C/C_{\text{crit}}^{\text{theo}} = 1.0$, as the flexible membrane also contributes to the blebbing onset.

Further, we discuss the effects of various membrane potentials on the blebbing onset. From the results in chapter 3, a negligible effect of the volume constraint and bending rigidity on blebbing is expected, while the area constraints and the resistance of the membrane to stretching play an important role.

4.3.4 Effects of Bending Rigidity and Volume Constraint

The fixed parameter set in table 4.1 is used to test the influence of k_{vg} on the blebbing onset. The value of k_{vg} is varied by several orders of magnitude to study whether this parameter affects blebbing. The measured values of τ_{equi} are shown in fig. 4.16. For values $k_{\text{vg}} \geq 6 \times 10^3 \text{ N m}^{-2}$, the curves show the same blebbing behavior within the limits of stochasticity in the system.

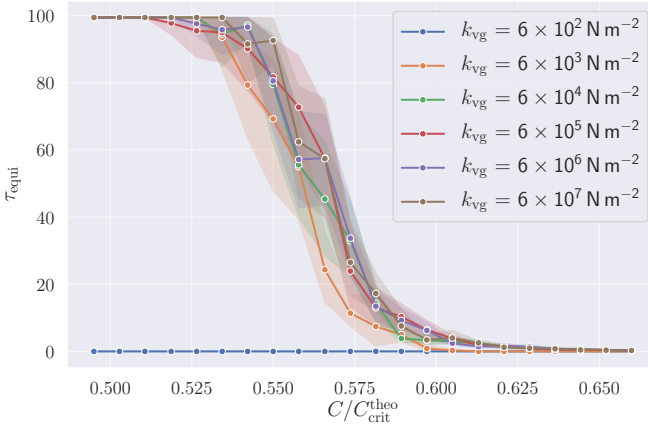


Figure 4.16: Average blebbing time as a function of $C/C_{\text{crit}}^{\text{theo}}$ for different volume constraint constants k_{vg} . The measured times are within an acceptable error margin for all configurations with $k_{\text{vg}} \geq 6 \times 10^3 \text{ N m}^{-2}$, indicating no significant dependence of blebbing on the volume constraint. For smaller values of k_{vg} , τ_{equi} cannot be established in a reliable way, as the volume constraint is not able to resist the applied tension through the contraction.

For small values of k_{vg} , τ_{equi} becomes zero. To better understand this, we take a look at some example shapes in fig. 4.17, corresponding

to the three lowest and the highest value of k_{vg} in fig. 4.16. The simulations are performed with a contraction $C = 0.2821$ and fig. 4.17 shows the final state from each simulation. For high values of k_{vg} , the shapes are very similar within an acceptable error margin, but for $k_{vg} = 6 \times 10^2 \text{ N m}^{-2}$, the volume constraint is too weak and is not able to keep the targeted spherical shape of the membrane under the contractile stress, resulting in spikes at the membrane surface and other non-physical shapes. Since the resulting network radius does

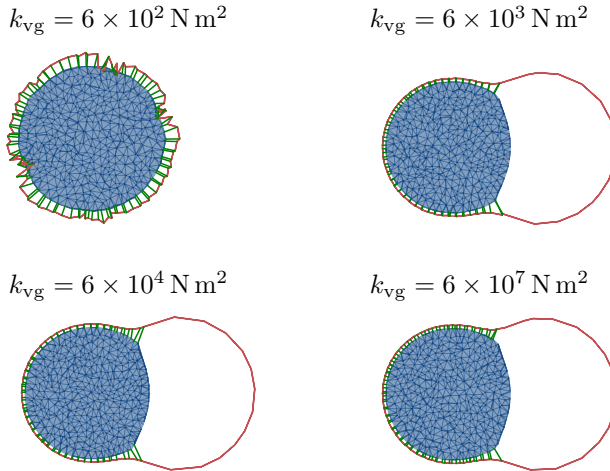
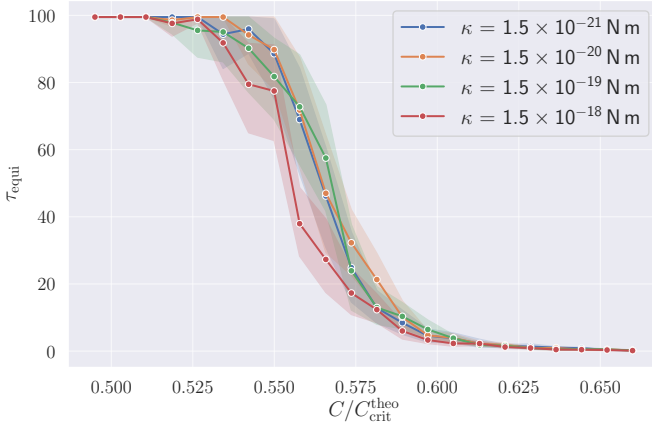
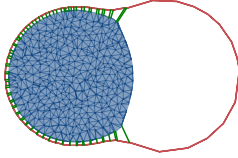


Figure 4.17: Example cell shapes for simulated configurations with various volume constraints. All simulations are performed with $C = 0.2821$ and the final cell shape of each simulation is shown. For high enough values of k_{vg} , the observed shapes are similar, as the influence of the volume constraint on blebbing is negligible. For smaller values of k_{vg} , the resulting shapes become non-physical as the volume constraint cannot resist the applied stress.

not match the predicted equilibrium state given by eq. (4.27), τ_{equi} cannot be established.



$\kappa = 1.5 \times 10^{-21} \text{ N m}$



$\kappa = 1.5 \times 10^{-18} \text{ N m}$

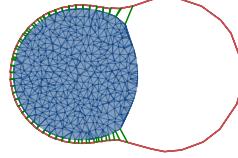


Figure 4.18: Values of τ_{equi} for different bending rigidities κ (top) and two shape examples (bottom). Similar to the volume constraint, no significant dependence of blebbing on κ is visible for both τ_{equi} and the obtained shapes, as the contribution of the bending energy is too small in comparison to the applied stress through the contraction.

In agreement with the results in chapter 3, the influence of the volume constraint parameter k_{vg} on blebbing onset can be neglected, when the constraint is strong enough to conserve the cell volume. Therefore, we choose $k_{\text{vg}} = 6 \times 10^5 \text{ N m}^{-2}$ for the rest of this chapter.

Similar tests are performed using values of the bending rigidity κ varying between 1.5×10^{-21} N m and 1.5×10^{-18} N m. The measured values of τ_{equi} and two shape examples are shown in fig. 4.18. No effect of κ on blebbing is observed for both τ_{equi} and the resulting shapes, since the contribution of the bending energy is too small in comparison to the applied stress.

Even though the bending rigidity has no effect on the blebbing onset, it facilitates realistic cell shapes with a smooth membrane surface (no sharp spikes). This is true even if κ becomes small. Therefore, $\kappa = 1.5 \times 10^{-19}$ N m is used in all further simulations.

4.3.5 The Effect of the Area Constraints

In contrast to the bending rigidity κ and the volume constraint coefficient k_{vg} , the effect of both area constraints is significant. We measure

| N^M | $\lambda_C/\text{pN } \mu\text{m}^{-1}$ | $\lambda_I/\text{pN } \mu\text{m}^{-1}$ | ϕ | F_B/pN | $C_{\text{crit}}^{\text{theo}}$ | $C_{\text{crit}}^{\text{meas}}$ |
|-------|---|---|--------|-----------------|---------------------------------|---------------------------------|
| 1000 | 5.54×10^4 | 69.4 | 1000 | 14.27 | 0.460 | 0.249 |
| 1000 | 5.54×10^4 | 69.4 | 1000 | 8.56 | 0.276 | 0.158 |
| 1000 | 5.54×10^4 | 69.4 | 1000 | 5.35 | 0.173 | 0.092 |
| 1000 | 1.11×10^5 | 69.4 | 1000 | 15.29 | 0.369 | 0.201 |
| 1000 | 1.11×10^5 | 69.4 | 1000 | 12.23 | 0.295 | 0.171 |
| 1000 | 1.11×10^5 | 69.4 | 1000 | 10.70 | 0.258 | 0.154 |
| 1000 | 1.11×10^5 | 104.1 | 1000 | 10.70 | 0.201 | 0.107 |
| 1000 | 1.11×10^5 | 104.1 | 1000 | 7.14 | 0.134 | 0.067 |

Table 4.3: $C_{\text{crit}}^{\text{meas}}$ measured against theoretical values $C_{\text{crit}}^{\text{theo}}$ for fixed ratio $\lambda_C/k_{\text{ag}} = 38.01$. The simulation parameters shown above as well as parameters in table 4.1 are used.

the parameter α from eq. (4.35) depending on the ratio between the strength of the inner network λ_C and the area constraints k_{ag} and k_{vg} . In fig. 4.19, α is shown for the ratio $\lambda_C/k_{\text{ag}} = 38.01$ and a fixed value

of k_{al} . The different types of symbols correspond to different inner network strengths λ_C , indicating that only the relative contribution λ_C/k_{ag} plays a role. Since the data show a linear dependence between C_{crit}^{theo} and C_{crit}^{meas} , we can find $\alpha = 0.551 \pm 0.011$ for $\lambda_C/k_{ag} = 38.01$.

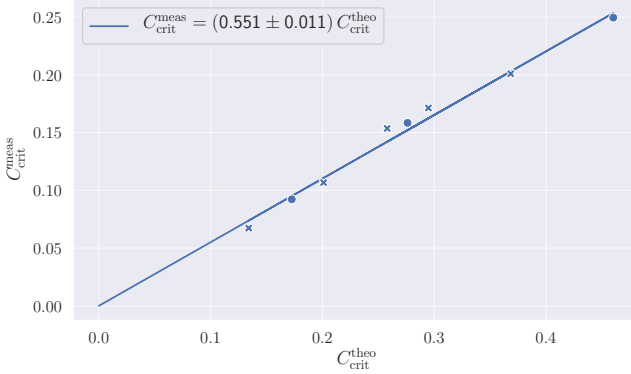


Figure 4.19: α is established by fitting the data in fig. 4.19 using eq. (4.35). The obtained rescaling factor shows the importance of the calculated bond instability, but rescaling is needed to incorporate membrane properties.

Performing simulations for other values of the ratio λ_C/k_{ag} with a constant k_{al} and for the ratio λ_C/k_{al} with a constant k_{ag} allows us to establish α for various configurations. Figure 4.20 summarizes these results, where the red dot marks α for the rigid membrane case, while the other points are measured for flexible membranes. We observe that an increase in k_{ag} and k_{al} leads to larger values of α , as the area constraint penalizes the expansion of the membrane area. For a very strong area constraint, we expect to obtain the same α as that for the rigid membrane in the previous section.

While both area constraint influence the blebbing onset, they also

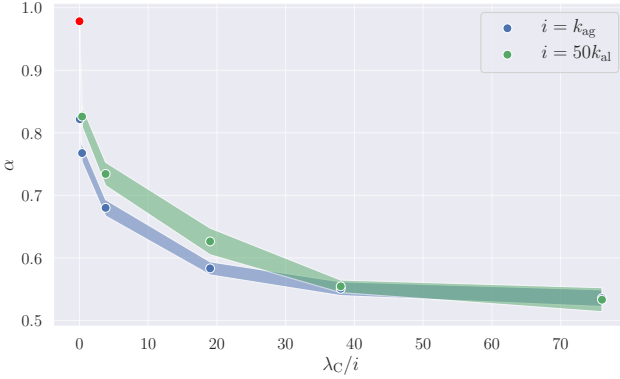


Figure 4.20: α as a function of the ratios λ_C/k_{ag} and λ_C/k_{al} . For both curves, a strong increase in α is observed when the area constraints are increased. For very strong area constraints, which do not allow any change in the membrane area, the results for the rigid membrane should be reproduced. For lower values of the area constraint, the dependence of α starts to level off, indicating that the resulting cell shapes become nearly independent on the values of k_{ag} and k_{al} .

have a significant effect on the resulting shapes. In fig. 4.21, simulated cell shape for various ratios λ_C/k_{ag} are shown. All setups are performed with simulation parameters given in table 4.1, $F_B = 8.56$ pN, and $C = 0.2400$, so that only the value of k_{ag} is varied. In addition, the relative area change $\Delta A = (A - A_0)/A_0$ is calculated for these configurations to quantify the expansion of the membrane.

For large values of k_{ag} , the resulting cell shapes stay nearly spherical after the blebbing transition. These spherical shapes do not agree well with the experimental shapes shown in fig. 4.1. Note that even small changes in ΔA already result in a strong increase of α from about $\alpha = 0.76$ to $\alpha = 0.82$. This confirms the pronounced dependence of α on the membrane stiffness close to a perfect area conservation.

$$\lambda_C/k_{ag} = 76.03, \Delta A = 5.16\% \quad \lambda_C/k_{ag} = 38.01, \Delta A = 4.23\%$$



$$\lambda_C/k_{ag} = 19.01, \Delta A = 3.32\% \quad \lambda_C/k_{ag} = 3.80, \Delta A = 1.60\%$$



$$\lambda_C/k_{ag} = 0.38, \Delta A = 0.10\% \quad \lambda_C/k_{ag} = 0.04, \Delta A = 0.09\%$$



Figure 4.21: Cell shape examples for various values of the ratio λ_C/k_{ag} .

All simulations are performed with the same parameter set shown in table 4.1, with $F_B = 8.56$ pN, $C = 0.2400$, and variable k_{ag} . The resulting blebbed shapes become more spherical for an increased value of k_{ag} , as a sphere requires less amount of extra membrane area than non-spherical shapes. For lower values of k_{ag} , the shapes show features, which are comparable to the experimental results.

For lower strengths of the area constraint, its effect on the shape

and of α is not that strong. While the cell shapes still differ, they show similar features for lower values of k_{ag} . Additionally, the average value of ΔA is within a realistic range of area change for membranes [41]. By comparing the simulated shapes to the experimental observations, we find a good correspondence between simulations and experiments for $\alpha \in [0.5, 0.6]$.

4.3.6 Theoretical Analysis of Blebbing

We have shown that the dependence of the blebbing onset on membrane properties can be described well by the pre-factor α . Since this is a purely linear rescaling of $C_{\text{crit}}^{\text{theo}}$ and the effects of the membrane parameters have been already discussed, we can focus now on the parameters given in eq. (4.34). To this end, we assume $\alpha = 1$.

In the experiments by Loiseau et al. [74], the number of membrane binding sites is controlled by the concentration of binding lipids within the lipid-bilayer membrane. Blebbing is observed only for certain values of this concentration. In simulations, the number of binding sites is limited, as the computational cost scales non-linearly with a change in N^M . Therefore, all performed simulations have employed $N^M = 1000$ or $N^M = 3000$ vertices. Assuming binding site densities up to $\rho_0 = 120 \mu\text{m}^{-2}$ [136] and an average cell size between $R_M = 5 \mu\text{m}$ and $R_M = 30 \mu\text{m}$ [74, 136], we obtain a number of binding sites up to $N^M \approx 1.3 \times 10^7$. Thus, we need to systematically analyze the influence of the number of binding sites on the blebbing process.

An increase in the number of binding sites stabilizes the connection linearly, as shown by eq. (4.30). More binding sites also result in an increased force needed for the unbinding event, which can be achieved by a larger pulling strength of the inner network λ_C . In fig. 4.22, the values of $C_{\text{crit}}^{\text{theo}}$ are plotted as a function of the spring constant λ_C and the number of bonds is indicated by various colors. The area below the curves corresponds to a stable configuration where no blebbing occurs, and above the curves, blebbing is expected. We observe a linear scaling between λ_I and N^M , because the resulting values of $C_{\text{crit}}^{\text{theo}}$ depend only

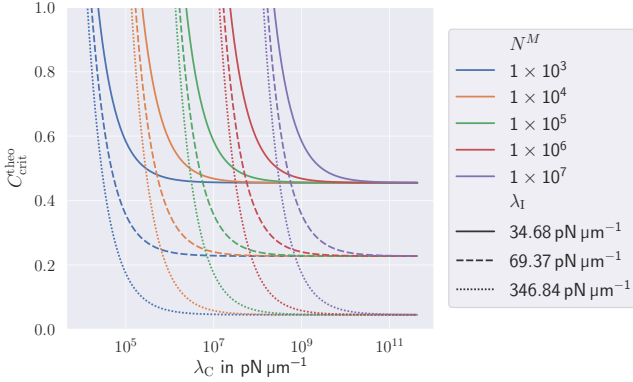


Figure 4.22: Dependence of $C_{\text{crit}}^{\text{theo}}$ on the number of binding sites, the contraction strength λ_C , and the strength of the adhesion bonds λ_I . An increase in the number of binding sites can be counteracted by the same increase in λ_C , such that blebbing transition is dependent only on the ratio N^M/λ_C . For low values of λ_I , the system relaxes before blebbing occurs, leading to a relatively large value of $C_{\text{crit}}^{\text{theo}}$ required for blebbing.

on their ratio. Therefore, an increase in the number of binding sites has to be counteracted by the same increase in the stress of the inner network, which may not be possible *in vitro*, since an increase in the number of myosin motor proteins leads to an unstable cytoskeletal network. This explains the experimental observation that blebbing is only possible for certain *Ni-NTA* lipid concentrations.

Another important factor for the onset of blebbing is the strength λ_I of the connections between membrane and cytoskeleton since it controls the equilibrium radius of the inner network. For small values of λ_I and C , the inner network relaxes to a configuration where the applied forces on the membrane are small. In this state, the onset of blebbing becomes independent of the contraction strength of the

inner network. The curves in fig. 4.22 show that the minimum value of $C_{\text{crit}}^{\text{theo}}$ is independent of the strength of the inner network as well as the number of bonds. This demonstrates how different binding interactions between cell membrane and inner network may not result in blebbing, since the single-bond dissociation can require much stronger contractions.

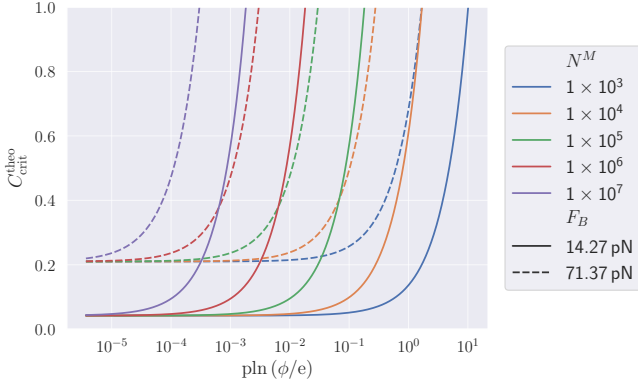


Figure 4.23: Dependence of $C_{\text{crit}}^{\text{theo}}$ on the number of binding sites, the binding-unbinding ratio ϕ and the force sensitivity F_B . If too many bonds are formed in comparison to the dissociation of bonds, blebbing becomes not possible since no cascading catastrophe can occur. The value of F_B has a similar effect as the bond strength on the minimal value of $C_{\text{crit}}^{\text{theo}}$ required for blebbing, since F_B shifts the required energy barrier for the catastrophe.

In fig. 4.23, the values of $C_{\text{crit}}^{\text{theo}}$ are shown as a function of $\text{pln}(\phi/e)$, where ϕ corresponds to the binding to unbinding ratio. A large value of ϕ stabilizes the connection between membrane and inner network for all configurations. In contrast to the results in fig. 4.22, we observe a non-linear dependence between N^M and $\text{pln}(\phi/e)$. Nevertheless, for all configurations, a large value of ϕ leads to no blebbing transition,

since not enough bonds can be broken.

In fig. 4.23, we also observe that a minimum value of $C_{\text{crit}}^{\text{theo}}$ for the blebbing onset is independent of N^M and ϕ but can be shifted by the bond sensitivity F_B . This shift can be explained by the resulting equilibrium states determined through the spring constants. If the applied stress in the equilibrium state is too low to unbind enough bonds, blebbing is not possible. This energy barrier is determined by the force sensitivity F_B .

In summary, our results show that blebbing is possible only for a small range of parameter sets, as the transition is sensitive to all bond interaction parameters. We observe that the minimum $C_{\text{crit}}^{\text{theo}}$ is determined by the strength of connection bonds λ_I and the force sensitivity F_B , as they determine, whether the applied stress in the equilibrium configuration is large enough to allow blebbing. Furthermore, an increase in the number of membrane binding sites has to be counteracted either by an increase in the strength of the contracting network λ_C or by a reduction of the binding-unbinding ratio ϕ . This explains why blebbing is observed only for a small parameter range *in vitro*, as the two mentioned options are not easily achievable.

4.4 Conclusions

In this chapter, we have introduced a model, which reproduces cell blebbing as a result of a contractile inner network. In this model, a lipid bilayer membrane is connected by stochastic bonds to an elastic network, which is able to contract in a controllable way. Using this model, blebbing behavior can be simulated and the model parameters can be adapted such that the resulting configurations are similar to experimental observations of blebbing. The simulation parameters possess realistic values with the Young's moduli of the relaxed inner network on the order of several kPa and the sensitivity of the connecting bonds in the range of a few pN. We observe the existence of a critical contraction value for the blebbing transition, below which no blebbing is observed.

Using a mean-field approach, we are able to predict the blebbing transition characterized by the critical contraction $C_{\text{crit}}^{\text{theo}}$ for the bond-based interaction model. We verify this theoretical prediction for rigid membranes, where the cell membrane is not able to deform. In the case of flexible membranes, we observe a proportionality scaling of the measured blebbing transition values $C_{\text{crit}}^{\text{meas}}$ and $C_{\text{crit}}^{\text{theo}}$ with the pre-factor α . Using the theory and simulations, we can separate the effects of the membrane properties and the bond adhesion model on cell blebbing, allowing us to study various parameters in more detail.

By probing the effects of different membrane parameters on blebbing, we observe that bending rigidity and volume constraint have no significant effects on the blebbing onset as well as the final cell shapes. In contrast, a strong dependence of blebbing on the local and global area constraints is observed, since blebbing is possible only through an increase in the membrane area. By comparing the simulation results with experimental observations of blebbed vesicles, we conclude that realistic bleb models are obtained for $\alpha \in [0.5, 0.6]$.

By calculating $C_{\text{crit}}^{\text{theo}}$ for various sets of the bond interaction parameters, we obtain boundaries for the existence of blebbing. The number of binding sites plays a vital role, since it stabilizes the connection between the membrane and the inner network. An increase in N^M can be counteracted by the same increase in the contraction strength of the inner network λ_C . An increase in the number of binding events in comparison to the number of unbinding events also stabilizes the connection between membrane and inner network, leading to stable cell systems. Lastly, the strength of the connection bonds between membrane and inner network and the sensitivity of the slip bonds control the barrier under which blebbing is not possible, since the applied stresses relax instantly. This effect may explain how different cells prevent cell blebbing by using different types of membrane-cytoskeletal connections.

In summary, the proposed cell model and theoretical analysis are able to reproduce stress-induced cell blebbing and to quantify several key scaling laws required for the existence of blebbing.

To use the introduced coarse-grained model for the quantification of experiments, more experimental data regarding some of the discussed parameters are required. By precisely measuring e.g. the number of binding sites within the membrane, other parameters of blebbing may be quantified using the simulation model. Similarly, we can predict main membrane properties by knowing the details about adhesion between the membrane and cytoskeleton.

The employed model has been driven by the experiments with synthetic vesicles. To extend it to complex biological cells, additional features, such as different types of interaction bonds, might be required, i.e. the addition of catch-bond-interactions with increasing bond lifetimes under stress.

5 Malaria Parasite Alignment

Malaria still remains one of the most devastating diseases around the world and accounts for about 500 000 deaths every year [76, 137]. While this number is slowly but steadily decreasing thanks to advancements in treating and preventing malaria, a better understanding of the infection process has still a high priority. This research is largely motivated by the search for new therapies, but in recent years, a new focus on the biophysical mechanics of the disease is observed [138–140].

This chapter focuses on a critical stage for the survival of the malaria parasite in a human host, the so called pre-invasion- or alignment-stage. First we introduce the general malaria cycle and discuss the importance of this stage. Then we introduce two simulation models that focus on open key questions for the mechanics of this stage. Both models are discussed in detail in the subsequent parts of this chapter and their results are compared to a number of experimental observations.

5.1 The Malaria Cycle

Malaria is caused by a parasite from the *Plasmodium* genus, in most cases by *Plasmodium falciparum*. To ensure its own survival, the parasite follows a certain number of events to multiply, see fig. 5.1. This closed malaria cycle starts with a bite of a female *Anopheles* mosquito, by which the malaria parasite is introduced into the skin of the human host. During the human part of the blood cycle, the parasite exists in

different forms, which are named sporozoites, merozoites, and gametocytes. The transitions between these stages occur between various steps of the malaria cycle.

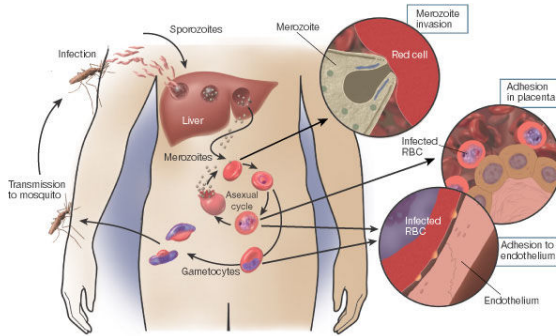


Figure 5.1: Schematic of the malaria cycle within humans. The host is infected via a mosquito bite, that introduces sporozoites into the skin. These sporozoites travel to the liver, where they multiply and are released into the blood stream as merozoites. Then RBCs are invaded by the merozoites, resulting in the common malaria symptoms. Some gametocytes are picked up by another mosquito during blood meal and, after a number of stages within the animal, can infect further hosts. Picture taken from [76] with permission.

Once introduced into the skin [141], sporozoites find the nearest bloodstream and are transported by blood flow via the vascular system to the liver of the host. Within the liver, each sporozoite can produce thousands of merozoites that are released from the liver into the blood stream [142, 143].

While the sporozoite has a long and thin shape, which is optimized for movement during the skin stage [145–149], the merozoite adapts a pear- or egg-like shape, as depicted in fig. 5.2. To ensure the survival of the parasite, the merozoite has to reproduce by invading red blood cells (RBCs) in the bloodstream. After around 48 hours past invasion,

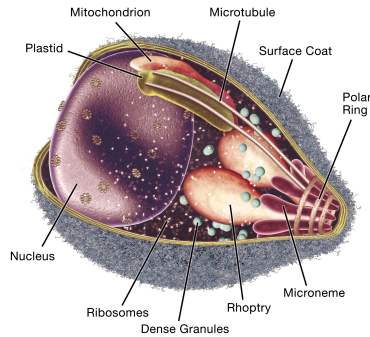


Figure 5.2: Schematic view of the merozoite during the blood stage. Its average shape is pear- or egg-like with an average size between $1\ \mu\text{m}$ and $2\ \mu\text{m}$. It contains a distinct apex structure that needs to be aligned head-first perpendicular to a RBC membrane to successfully invade it. Once within the RBC, it reproduces asexually and then bursts the infected cell, releasing about 20 new merozoites to invade further RBCs. Picture taken from [144] with permission.

the membrane of the infected RBC bursts open, releasing around 20 new merozoites into the bloodstream. This repeating process within the full malaria cycle in fig. 5.1 is called the blood stage or blood cycle. The common symptoms of a malaria infection such as fever, tiredness, vomiting and headaches [150] can be observed during the blood stage since changes in the elastic properties and the bursting of the infected RBCs occur, altering the behavior of blood in the vascular system. The human part of the malaria cycle is completed by turning a number of parasites into gametocytes. These can be picked up by another mosquito blood meal and after several stages within the mosquito, new humans can be infected as described above. [76]

5.2 Invasion of a Red Blood Cell

The successful invasion of a RBC by a merozoite is the key aspect during the blood stage, as the malaria parasite can only survive within the host if enough merozoites are able to reproduce [144, 151, 152]. There are two stages in the invasion process. In the first stage called parasite alignment, the merozoite aligns itself on the surface of a RBC. After a successful alignment, the actual invasion takes place. The alignment stage is short and takes between 2 s and 50 s, as the merozoite loses its ability to invade a RBC after about 3 min [77]. To date the alignment period is poorly understood, even though a number of experiments have pointed out several key aspects of the alignment [78–86, 144].

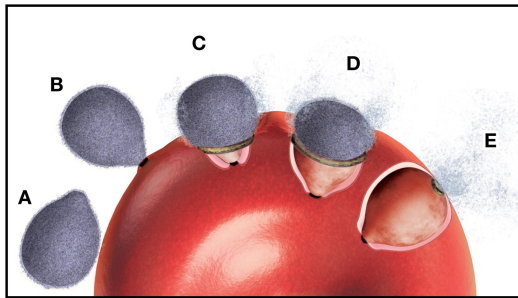


Figure 5.3: Different stages of a successful invasion event. At the first contact of the parasite, the head is aligned arbitrarily to the surface of the RBC (A). Through a yet unknown mechanism, the parasite aligns its head perpendicular to the RBC (B). This process is often accompanied by strong deformation as a result of the interaction of the membrane with the parasite. After alignment, the apex structure forms a tight junction complex, which allows the penetration of the membrane (C-E). Picture taken from [144] with permission.

The merozoite has a pear-like shape with an average size of around $1\ \mu\text{m}$ to $2\ \mu\text{m}$ and a distinct head or apex structure (see fig. 5.2) [144, 153]. For a successful invasion, this structure needs to be aligned

head-first perpendicular to the membrane surface (see fig. 5.3) [84, 144]. This alignment is controlled by the parasite, as its first contact with a potential invasion target is random and the orientation of the apex toward the membrane is arbitrary. After the first contact, several agonists, that coat the parasite, can form bindings between the two cells. These bounds are of various lengths between 20 nm and 150 nm [79] and are reversible, leading to strong movement of the parasite during alignment.

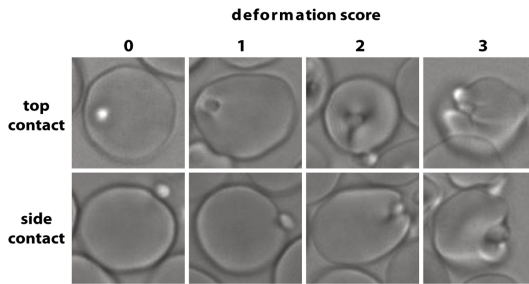


Figure 5.4: Examples of different membrane deformations *in vitro*. The deformations range from not visually detectable to a complete loss of the biconcave shape of the RBC. Based on the visible deformation, a deformation index can be assigned. Different experiments show a positive correlation between this score and the probability for a successful invasion event [85, 86]. Picture taken from [85] (open access).

The pre-invasion stage is often accompanied by membrane fluctuations of various intensity, as depicted in fig. 5.4 [82]. The induced deformation ranges from small indentations at the RBC surface to a total loss of the original RBC biconcave shape. To quantify the deformation in experiments, a discrete deformation index I_d is introduced [85]. It is divided into four categories, which can be summarized as

$I_d = 0$ No visible deformation.

$I_d = 1$ Small and local deformation.

$I_d = 2$ Partial wrapping of the parasite by a membrane with local deformation.

$I_d = 3$ Strong wrapping of the parasite, such that the RBC shape is globally deformed.

Several experiments show a positive correlation between this deformation index and the probability for a successful invasion event [85, 86], implying that the deformation is actively introduced by the parasite to enhance its chance of alignment and invasion.

The current working hypothesis based on available information suggests that local changes in calcium mediate membrane deformation. In this scenario, the parasite can induce a local change in the calcium concentration within the RBC, leading to the softening of the membrane. This mechanical change then leads to a more successful alignment and subsequently to a higher chance of invasion.

In most recent experiments however, no increased calcium concentrations were detected [86], indicating that the response of the RBC is rather passive than active. This leads to the passive compliance hypothesis [86], which suggests that the deformation is aiding the alignment of the parasite, but instead of an active reaction of the membrane to calcium concentration changes, the membrane reacts to mechanical stress induced by the parasite. To this end, the observed parasite adhesion applies forces onto the membrane, leading to the deformation of the RBC membrane [154]. A number of early observations support this hypothesis, for example the experiments in ref. [79].

While the experiments point toward the direction of a mechanical approach, a number of fundamental questions still remain unanswered, for example:

1. Is the parasite able to induce the observed deformation purely by mechanical interaction? Is the required interaction strength in accordance with experimental measurements?
2. Does the described mechanism represent a suitable and realistic way to align the parasite?

3. Is the observed deformation facilitating the alignment of the parasite?

In this chapter, we address these questions using two simulation models, which implement the fundamental idea of the passive compliance hypothesis, and compare simulation results to the experimental observations.

5.3 Simulation Models

To study the alignment process, we introduce two models. Both models contain a RBC and a merozoite, but they differ in the type of interaction between the two cells. The first model utilizes an interaction potential and is used to assess the general feasibility of the passive compliance hypothesis, focusing on the membrane deformation and the adhesion forces.

The second model represents an active interaction between the parasite and RBC by using a two-state bond model. These bonds can form and break, leading to a stochastic dynamics of the parasite on its targeted cell. We discuss the observed dynamics, the achievable deformations, the importance of the parasite shape, as well as the contribution of different types of bonds to a successful parasite alignment.

5.3.1 Red Blood Cell Model

Similar to the membrane model introduced in chapter 3, the RBC is represented by a two dimensional surface mesh, where N^M vertices are distributed. The typical shape of a healthy RBC is a discocyte, biconcave shape as shown in fig. 5.5. Most of the interactions, which govern the behavior of the RBC, were introduced in chapter 3. The full potential is given by

$$U_{\text{membrane}} = U_{\text{bending}} + U_{\text{area}} + U_{\text{volume}} + U_{\text{spec}}, \quad (5.1)$$

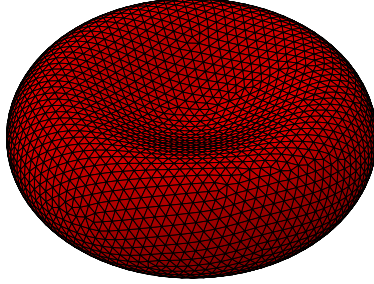


Figure 5.5: Schematic of a RBC model. The typical discocyte shape is modeled by N^M vertices that are distributed on the membrane surface. The vertices are connected by bonds, providing elastic properties of a RBC.

where the bending energy, the area and the volume constraints are given by eqs. (3.12) to (3.14), respectively. The last term models an elastic contribution of the spectrin network of the RBC. Its potential energy is given by

$$U_{\text{spec}} = \sum_{i=1}^{N_S^M} \left[\frac{k_B T l_m (3x_i^2 - 2x_i^3)}{4l_p (1 - x_i)} + \frac{\lambda_p}{l_i} \right], \quad (5.2)$$

where N_S^M is the number of bonds within the triangulated network, l_i is the length of the i -th spring, and l_m is the maximum spring extension. The ratio $x_i = l_i/l_m$ gives the maximum length ratio for each spring. The other parameters are the persistence length l_p and the spring constant λ_p . To set a stress free state for the elastic network, a non-zero equilibrium length l_i^0 is assigned to each bond such that

l_i^0 is set individually for each bond according to the initial triangulated shape [124]. For a regular hexagonal triangulation, this potential corresponds to the membrane shear modulus given by

$$\mu_0 = \frac{\sqrt{3}k_B T}{4l_p l_m x_0} \left(\frac{x_0}{2(1-x_0)^3} - \frac{1}{4(1-x_0)^2} + \frac{1}{4} \right) + \frac{\sqrt{3}\lambda_p}{2l_0^3}, \quad (5.3)$$

where l_0 is the average equilibrium spring length and $x_0 = l_0/l_m$ [110]. Combining the elastic energy and the area constraints given by eq. (3.12), the area-compression module is given by

$$K = 2\mu_0 + k_{ag} + k_{al} \quad (5.4)$$

and the two-dimensional Young's modulus can be calculated as

$$Y^M = \frac{4K\mu_0}{K + \mu_0} \quad (5.5)$$

and is used to quantify the membrane elasticity throughout this chapter.

5.3.2 Parasite Model

Similar to the RBC, the parasite is modeled by a two-dimensional shell. The shape of a parasite is similar to an egg or a pear, which can be described by the shape equation

$$\mathbf{r}^4 = R_a r_x^3 + (R_a - R_b) r_x (r_y^2 + r_z^2), \quad (5.6)$$

where $R_a = 1 \mu\text{m}$ and $R_b = 0.7 \mu\text{m}$ provide a good match for the average parasite shape [153]. To analyze the influence of the parasite shape, different ellipsoids are used, with their shapes given by

$$\frac{r_x^2}{a^2} + \frac{r_y^2}{b^2} + \frac{r_z^2}{c^2} = 1, \quad (5.7)$$

where a, b, c are characteristic lengths to control the shape of the parasite. They are chosen in such a way, that the surface area of different

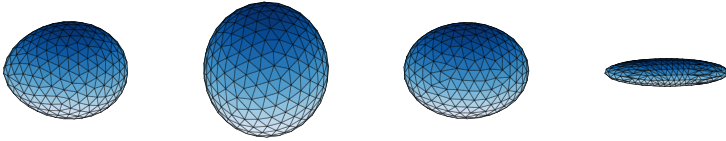


Figure 5.6: Sketch of the different shapes used to model the parasite.

The left, egg-like, shape is given by the eq. (5.6) and represents the best shape of real parasites. To test the influence of the parasite shape, a sphere and two ellipsoids are introduced, such that all shapes share the same surface area and roughly the same number of vertices.

| Name | Type of shape | Characteristic lengths | N_{para} |
|------|-----------------|--|-------------------|
| PA | egg-like | $R_a = 1 \mu\text{m}, R_b = 0.7 \mu\text{m}$ | 310 |
| SP | sphere | $a = b = c = 0.4 \mu\text{m}$ | 312 |
| ES | short ellipsoid | $a = 0.5 \mu\text{m}, b = c = 0.356 \mu\text{m}$ | 306 |
| EL | long ellipsoid | $a = 1.0 \mu\text{m}, b = c = 0.205 \mu\text{m}$ | 306 |

Table 5.1: Characteristic parameters of the introduced parasite shapes.

shapes is similar as well as the number of vertices used to discretize the surface. The shapes used in this chapter are shown in fig. 5.6 and their characteristic parameters are summarized in table 5.1.

From experimental videos, we observe that the parasite does not deform itself while interacting with the RBC. Therefore, the parasite is modeled as a rigid body. The parasite dynamics is therefore established by the following algorithm:

1. The forces on all parasite vertices are calculated.
2. All forces are applied to the center of mass of the parasite. The resulting translational force and torque are calculated and the equations of motion are integrated.

3. The parasite vertices are moved accordingly to model the dynamics of the whole parasite.

5.3.3 Hydrodynamic Interactions

The simulations are performed within the DPD framework, which represents hydrodynamic interactions and was introduced in section 2.1. The modeled viscosity is established as discussed in section 2.1 and the viscosity of water is chosen as reference value.

5.3.4 Potential Adhesion Interaction

To model the interaction between the merozoite and the RBC, we introduce an adhesive LJ potential. We assume that the agonists on the membrane surface contribute an average amount of energy to the interaction, approximated by an average potential. The interaction is defined between every vertex on the RBC membrane \mathbf{r}_{rbc} and the corresponding vertices on the parasite surface \mathbf{r}_{para} as

$$U_{\text{adh}}(\mathbf{r}_{\text{rbc}}, \mathbf{r}_{\text{para}}) = 4\epsilon(\mathbf{r}_{\text{para}}) \left[\left(\frac{\sigma}{r} \right)^{12} - \left(\frac{\sigma}{r} \right)^6 \right] \quad r \leq r_{\text{cutoff}}. \quad (5.8)$$

$r = |\mathbf{r}_{\text{rbc}} - \mathbf{r}_{\text{para}}|$ is the distance between the particles, while r_{cutoff} is the maximum interaction length, ϵ is the effective strength of the interaction and σ characterizes the length scale of the interaction. The minimal energy of the LJ potential is at $r_{\text{size}} = \sqrt[6]{2}\sigma$, such that below this value the potential is repulsive and above attractive. We attribute the length r_{size} to the effective size of the parasite. For the simulations, $\sigma = 0.15 \mu\text{m}$ and a cutoff of $r_{\text{cutoff}} = 0.4 \mu\text{m}$ are chosen, which lead to a maximal attractive interaction range of $r_{\text{cutoff}} - r_{\text{size}} = 0.23 \mu\text{m}$.

Another possibility discussed in the literature is the existence of an interaction gradient, where the number of agonists is higher around the head of the parasite than at the back. To study the impact of such

a gradient, we describe the density of the agonists by the relation

$$\rho(\mathbf{r}_{\text{para}}) = \rho_a \xi(\mathbf{r}_{\text{para}})^a, \quad (5.9)$$

where ρ_a is the overall density of the agonists and $\xi(\mathbf{r}_{\text{para}})^a$ models the dependence at the position on the parasite surface. The exponent a leads to different interaction models, where $a = 0$ reproduces the classical LJ interaction which is the same everywhere on the surface of the parasite. The value ξ is chosen in such a way that for $a = 1$,

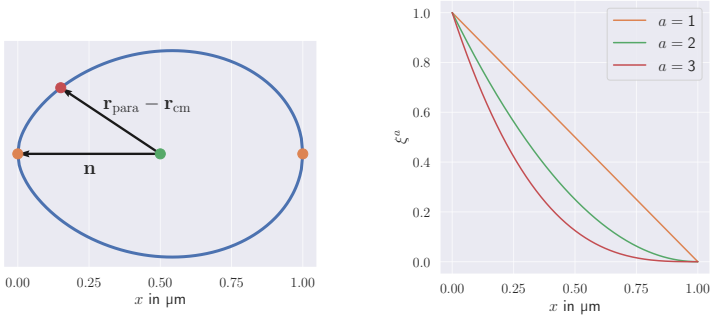


Figure 5.7: Schematic of the vectors used to calculate the interaction gradient. The directional vector \mathbf{n} of the parasite is orientated from its back to its head. Depending on the position of a vertex \mathbf{r}_{para} , the strength of the interaction between parasite and membrane is calculated using eq. (5.10). This equation is chosen in such a way that the interaction for $a = 1$ decreases linearly from a maximum at the head to zero at the back. By using higher values of a , head-dominated interactions are established and should improve head alignment.

the interaction strength decreases linearly from its maximum at the head to zero at the back of the parasite:

$$\xi(\mathbf{r}_{\text{para}}) = \frac{\mathbf{n} \cdot (\mathbf{r}_{\text{para}} - \mathbf{r}_{\text{cm}})}{2\mathbf{n}^2} + 0.5. \quad (5.10)$$

\mathbf{n} is the directional vector of the parasite, pointing from its back to its head and \mathbf{r}_{cm} is the position of its center of mass. The vectors and the resulting gradients are shown in fig. 5.7. For values $a \geq 1$, the interaction is strongly localized around the head of the parasite, which will lead to a better alignment of the parasite.

In the employed coarse-grained, discrete description of the parasite, each vertex represents a surface patch A_c and therefore an effective number of agonists $A_c \rho(\mathbf{r}_{\text{para}})$. We assume that on average, each of the agonists contributes the same amount of energy ϵ to the effective interaction, so that the total strength is given by

$$\epsilon(\mathbf{r}_{\text{para}}) = \epsilon A_c \rho_a \xi(\mathbf{r}_{\text{para}})^a = \epsilon_a \xi(\mathbf{r}_{\text{para}})^a \quad (5.11)$$

with the interaction strength ϵ_a . Depending on this strength and the exponent a , the parasite will adhere differently to the membrane.

5.3.5 Two-State Adhesive Bond Model

The second model focuses on an interaction that cannot be described by an average potential. It has two major components. The first one models the size of the parasite, using the repulsive part of the LJ potential. It ensures that the parasite and the RBC cannot overlap. The second part of the attractive interaction is modeled through a reversible, bond based two-state model. A number of bonds can form and dissociate between the vertices of the RBC membrane and the merozoite surface. These bonds, which represent the interactions between the two cell, have two types: long bonds with a maximum length of 200 nm and short bonds of 20 nm. They are described by elastic springs with the potential energy

$$U_{\text{ad}}(l) = \frac{\lambda_{\text{ad}}^{\text{type}}}{2} (l_0 - l)^2, \quad (5.12)$$

where l is the instantaneous length and l_0 is the spring length at rest. The rest length is chosen as $l_0 = \sqrt[6]{2}\sigma$, corresponding to the effective

surface of the parasite. The constant $\lambda_{\text{ad}}^{\text{type}}$ is the strength of the elastic bonds of a given type.

To model the dynamic interaction, we introduce constant on- and off-rates

$$k_{\text{on}}^{\text{type}}(l) = k_{\text{on}}^{\text{type}}, \quad (5.13)$$

$$k_{\text{off}}^{\text{type}}(l) = k_{\text{off}}^{\text{type}} \quad (5.14)$$

to simplify the model behavior and reduce the number of parameters. The bonds can form between the particles on the RBC and the parasite surface if the distance between them is short enough, but their number is limited to one bond per vertex for every bond type. To reduce the amount of parameters, we choose the same spring constant and the same off-rate for both bond types. Therefore, we refer to them as λ_{ad} and k_{off} further in this text.

5.4 Results of the Potential Interaction Model

One key aspect of the passive compliance hypothesis is the ability of the parasite to deform the membrane of a RBC through the mechanical interactions of the agonists on the parasite surface. This section focuses on this process by using the potential adhesive model. We compare the simulation results to experiments, introduce the deformation energy to quantify deformations, and measure the adhesion forces in order to check whether the membrane deformations are induced by realistic interaction forces. Lastly, the interaction gradients are investigated.

The simulation setup contains one RBC and one parasite, both emersed in the DPD fluid. We investigate the effects of the strength of the adhesive potential and the type of the interaction in regard to the questions mentioned in the beginning of this chapter. A number

| Parameter | Simulation Value | Physical Value |
|---------------------|--|-----------------------------------|
| $k_{\text{B}}T$ | 0.01 | 4.282×10^{-21} J |
| D_0 | 6.5 | 6.5×10^{-6} m |
| η | 1.85 | 1×10^{-3} Pa s |
| Δt | 0.005 | 6.31 μ s |
| N_{para}^M | 310 | |
| N_{rbc}^M | 3000 | |
| κ | 70 $k_{\text{B}}T$ | 3.0×10^{-19} J |
| Y^M | $1.82 \times 10^5 k_{\text{B}}T/D_0^2$ | 1.84×10^{-5} N m $^{-1}$ |

Table 5.2: Overview of the main simulation parameters. The thermal energy $k_{\text{B}}T$, the average diameter of a RBC D_0 , and the viscosity of the fluid are used to define the energy-, length-, and timescales. The number of vertices for the parasite and RBC are constant in all simulations. The parameters for the RBC model are chosen to model a healthy RBC under physiological conditions.

of general parameters, which are kept constant in all simulations, are summarized in table 5.2. The membrane parameters are chosen to model a healthy RBC under physiological conditions [110].

To establish the energyscale, the thermal energy $k_{\text{B}}T$ is used as a reference value as described in section 2.3. Similarly, we introduce the diameter of the RBC $D_0 = \sqrt{A/\pi}$, where A is the area of the cell, as lengthscale. On average, this size is found to be $6.5 \mu\text{m}$ for a real RBC. To define the timescale of our simulations, the viscosity η of the modeled DPD fluid is combined with the length- and energyscale to obtain the relation

$$t^P = \frac{\eta^P (D_0^P)^3 (k_{\text{B}}T)^M}{\eta^M (D_0^M)^3 (k_{\text{B}}T)^P} t^M \quad (5.15)$$

for the physical time. The viscosity of water $\eta = 1 \text{ mPa s}$ is used as a reference.

For each simulation, the merozoite is brought directly into its interaction range with the RBC, as we focus on the mechanical aspects of the adhesion and neglect other aspects like the probability for a first contact. To study a worst case scenario, the head of the parasite points away from the membrane at the beginning of the simulation. During the simulation, the parasite is let to adhere to the membrane of the RBC. Depending on the starting configuration, this adhesion

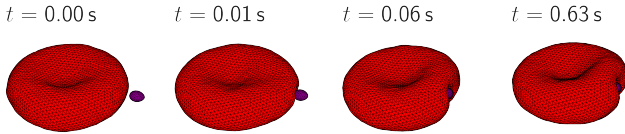


Figure 5.8: Example of a parasite adhering to a RBC. At the beginning, the parasite is brought into interaction range with the membrane, so that it adheres to the membrane surface. This adhesion is strong enough to suppress further diffusion of the parasite, therefore the final configuration is stable over the course of a simulation.

occurs either at the side or top of the RBC. As the interaction potential is permanent, the adhesion suppresses the diffusion of the parasite. Therefore, the system comes to a stable configuration over the course of each simulation. In fig. 5.8, a short time series of one simulation is shown.

5.4.1 Membrane Deformations

The snapshots in fig. 5.8 show that the RBC deforms as a result of the interaction with the parasite. To quantify the deformation, we introduce the deformation energy

$$\Delta E_{\text{rbc}} = U_{\text{membrane}}(\text{deformed}) - U_{\text{membrane}}(\text{equilibrium}) \quad (5.16)$$

as the energy difference of the RBC energy given by eq. (5.1) between the equilibrium state and the deformed state. Through the interaction with the fluid, the membrane exhibits thermal fluctuations which affect this energy. The energy measurements are therefore averaged

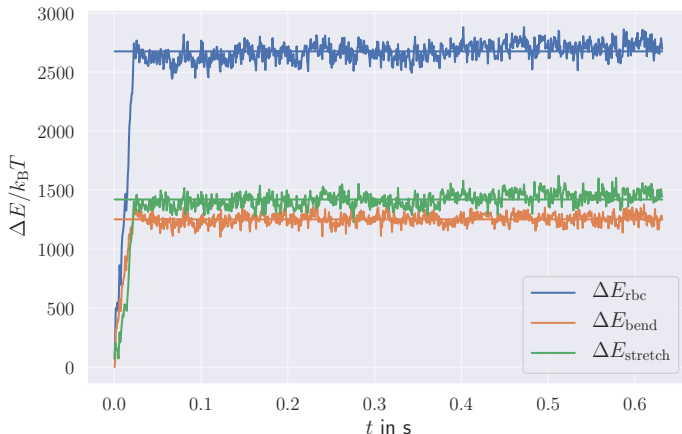


Figure 5.9: Deformation energies for the simulation shown in fig. 5.8.

Reliable results are obtained by averaging over the time of the simulation, once the parasite has tightly adhered to the RBC surface. From the four parts of the deformation energy, only the bending and elastic energies contribute a non-negligible amount to the total deformation energy, as shown by the orange and and green lines.

over the equilibration and interaction stage. The latter is possible, because the deformed configurations are stable over time, as shown in fig. 5.9. Additionally, we see that the time between the beginning of the simulation and reaching the stable and adhered configuration is with $t \ll 0.1$ s much shorter than the experimentally observed times. This result is similar for all simulations performed in this section.

The main significant contributions to the deformation energy are the bending and elastic energies, illustrated in fig. 5.9. The volume

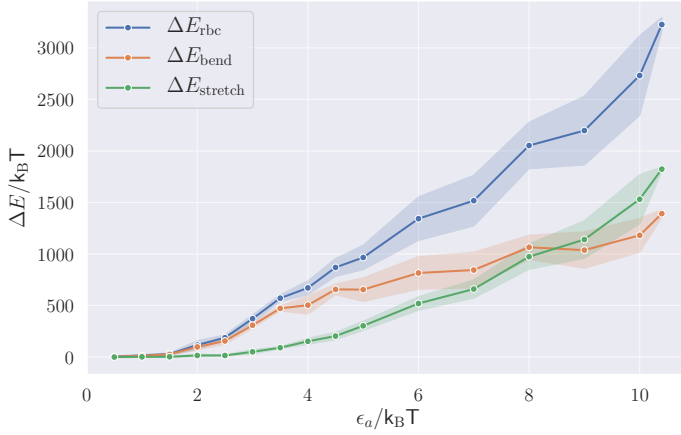


Figure 5.10: Deformation energy for $a = 0$ and different values of ϵ_a .

The total energy grows with increasing interaction strength. The two main contributions are the bending and stretching energies. For small interaction strengths, both contributions remain small. For small membrane deformations, the bending energy dominates, while the stretching energy stays negligible. For strong adhesion, the stretching energy starts to dominate the deformation energy.

and area constraints are chosen in such a way that they maintain the shape of a RBC, but do not strongly contribute to the energy and dynamics.

To study the effect of the adhesion strength on deformations and the deformation energy, we vary ϵ_a and the point of initial contact, which can be at the side or on the top of the RBC. The deformation energies shown in fig. 5.10 are the averaged values from multiple simulations with the same cell parameters and $a = 0$. In fig. 5.11, several examples of final configurations are presented. In the top row, the first contact is at the side of the RBC, while in the lower row, the parasite adheres at the top.

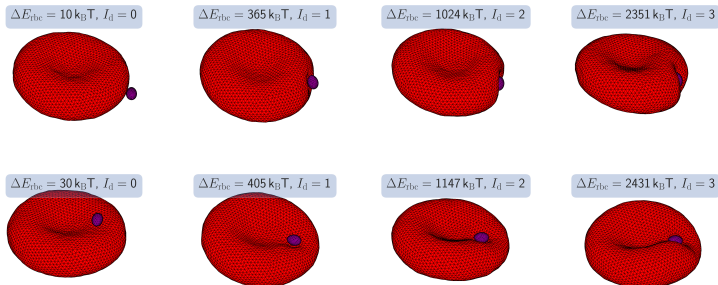


Figure 5.11: Examples for different deformation indices. By increasing the interaction strength, different levels of deformation are obtained. In experiments, these are classified by the discrete deformation index I_d , which is assigned by eye, while in the simulations, we use the deformation energy to assign this score. The criteria for both are summarized in table 5.3. The exact value of the deformation energy depends on the point of contact, e.g. at the top or side of the RBC. A stable average value is observed for all simulations.

Both the visible deformation and the energy grow with an increased adhesion strength, whereas the total energy increases nearly linearly with ϵ_a . The contributions of the bending and stretching energies have a different dependence. For weak interactions, both energies do not show significant contributions and there are no visible deformations at the surface of the membrane. The first visible deformation can be connected to a rise in bending energy while the elastic contribution stays small. When the membrane begins to partially wrap the parasite, the elastic energy can contribute on a similar level as the bending energy. Strong wrapping and the resulting considerable deformations correlate with a dominating elastic energy. Interestingly, these four deformation categories correlate well with the discrete deformation index I_d introduced to quantify the experimental deformations, which in our simulations were assigned to judge the visible deformations.

Therefore, we can define energy barriers for the four scores which are summarized in table 5.3. The values for the barriers have to be considered with care as a discrete score was assigned by visual assessment of membrane deformation, but they provide a convenient way to quantify the deformations of the RBC.

| I_d | Level of deformations | $\Delta E_{\text{rbc}}/k_B T$ |
|-------|---|-------------------------------|
| 0 | No visible deformations. | $[0, 150)$ |
| 1 | Small and local deformations. | $[150, 800)$ |
| 2 | Partial wrapping of the parasite, local deformations. | $[800, 2000)$ |
| 3 | Strong wrapping of the parasite, RBC shape globally deformed. | ≥ 2000 |

Table 5.3: Discrete deformation index to quantify the level of deformation. To quantify deformations, the discrete deformation index I_d is introduced. It is assigned by eye in the experiments. In the simulations, we use the deformation energy ΔE_{rbc} to quantify the results. The energy barriers are defined by assigning the scores according to the visible deformations.

Next, different interaction gradients $a \in [0, 1, 2, 3]$ are used. We perform a number of simulations and the corresponding deformation energies are shown in fig. 5.12. In general, all interaction models behave similar, as the deformation of the RBC increases with increasing strength of the adhesion. The defined deformation scales, marked by the dashed lines in fig. 5.13, are used to assign the deformation indices for all configurations. The major difference between the models is the slope of nearly linear curves. Higher values of a lead to lower slope values, as the effective area of the parasite interacting with the membrane becomes smaller. This is due to the interaction being centered around the head of the parasite.

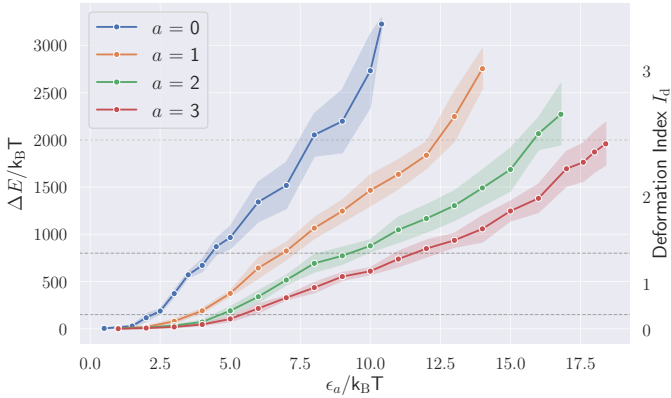


Figure 5.12: Deformation energy for different values of $a = 0$. For all interaction models, the energy increases when the interaction strength ϵ_a grows and we obtain similar energy levels. For higher values of a , the slope of the curve becomes smaller. This is due to the interaction being localized at the parasite head, resulting in a smaller interaction area between parasite and membrane.

The main purpose of a gradient pointing toward the head of the parasite is to facilitate its aligning. In fig. 5.13, several configurations are shown in order to compare different interaction models with roughly the same deformation energy. The gradient is indicated on the parasite surface by the color, where purple marks the maximum interaction strength and green corresponds to the minimal values. The main difference between $a = 0$ and the other values is the preferred orientation of the parasite. For $a = 0$, the parasite lies sideways, as it maximizes its interaction area in this position. However, for all gradients, the parasite will align perfectly by pointing its head toward the membrane. This occurs for all values of ϵ_a and all models with $a > 0$. By comparing the simulated configurations with the experiments by Crick et al. [77], we establish that configurations for $a = 0$ generally look more realistic.

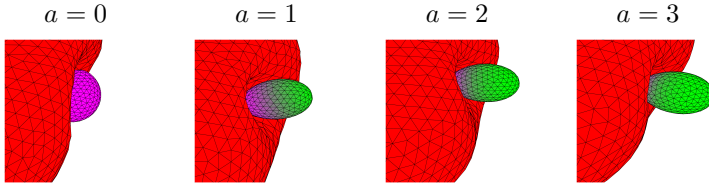


Figure 5.13: Examples of the adhered parasite for $a = 0, 1, 2, 3$ (left to right). The color at the parasite surface indicates the strength of the interaction given by $\xi(\mathbf{r}_{\text{para}})$ in eq. (5.10) where purple indicates the maximum interaction strength and green the minimum strength. The important difference between $a = 0$ and the other models is, that whenever there is an interaction gradient, the parasite aligns itself perfectly at the membrane surface.

5.4.2 Adhesive Force

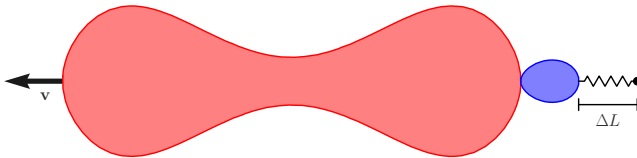


Figure 5.14: Schematic of the pulling test to measure the adhesion force. The center of mass of the adhered parasite is tethered to a spring at the beginning. The RBC is pulled away from the parasite with a constant velocity \mathbf{v} . As a result, both the RBC and the spring extend as long as the parasite stays adhered to the membrane. The adhesion force is measured through the elongation of the spring when the connection ruptures.

So far, we have shown that the parasite is able to deform the membrane similar to observed deformation in the experiments, using the

adhesive potential model. So verify that these deformations are associated with realistic adhesion strengths, the adhesion force is measured. To this end, pulling tests inspired by the work of Crick et al. [77] are performed, where a non-active parasite was adhered to two RBCs. Due to little or no activity of the parasite, the setup remains stable. Then one of the RBCs is pulled away with a constant velocity by optical tweezers, resulting in stretching of the RBCs until the connection between the parasite and one of the cells ruptures. The adhesion force is measured through the elongation of the RBC, as the cell can be interpreted as a spring for small enough pulling velocities. The obtained range of rupture forces is between 10 pN and 40 pN.

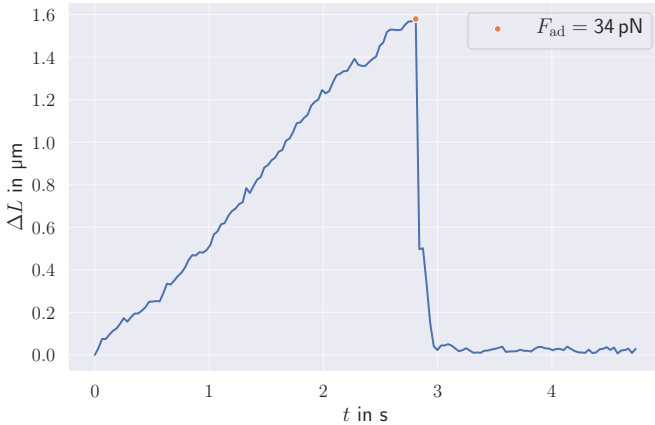


Figure 5.15: Pulling test to measure the adhesion force. The center of mass of the parasite is tethered by a spring. As a result of the RBC being pulled away, the length of the spring increases by ΔL . The adhesion force is measured when the connection between parasite and membrane ruptures, indicated by a sudden drop in the spring elongation.

To perform similar tests *in silico*, one of the RBCs is replaced by a spring that is tethered to the center of mass of the merozoite. The

other RBC is pulled away from the adhered parasite with a constant velocity \mathbf{v} , as shown in fig. 5.14. The adhesion force is calculated through the elongation ΔL of the spring, when the connection between the parasite and membrane ruptures, as

$$F_{\text{ad}} = k\Delta L, \quad (5.17)$$

where k is the spring constant chosen to be $k = 20 \text{ pN } \mu\text{m}^{-1}$ to approximate the RBC that has been replaced by the spring [77]. In fig. 5.15, an example of such a measurement shows that the maximum elongation of the spring can be found easily when the parasite detaches from the RBC membrane.

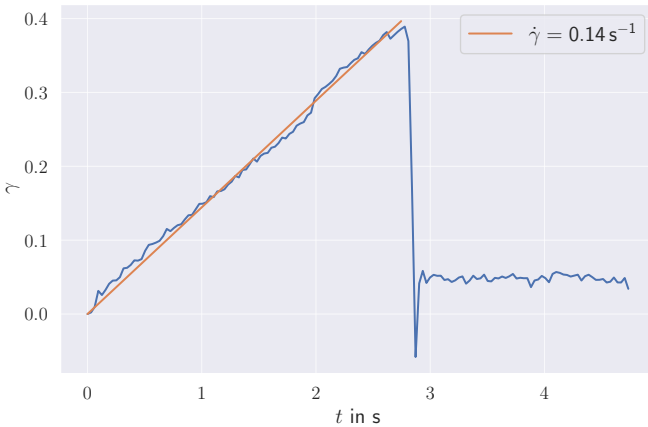


Figure 5.16: Determination of the strain rate $\dot{\gamma}$. The adhesion force depends on the pulling speed of the RBC. To obtain comparable results with the experiments, the velocity is chosen in such a way that the strain rate is about $\dot{\gamma} \sim 0.1 \text{ s}^{-1}$.

The pulling velocity \mathbf{v} is chosen carefully, as the measurement of the adhesion force depends on it. To approximate the original exper-

iments, the strain rate of the RBC

$$\dot{\gamma} = (D - D_0)/D_0T \quad (5.18)$$

is set to be on the order of $\dot{\gamma} \sim 0.1 \text{ s}^{-1}$. D_0 is the initial RBC length in pulling direction, D is the instantaneous length and T is the duration of the experiment. The value of $\dot{\gamma}$ is calculated by fitting the strain as a linear function of time within the part where the merozoite is adhered to the membrane, as shown in fig. 5.16.

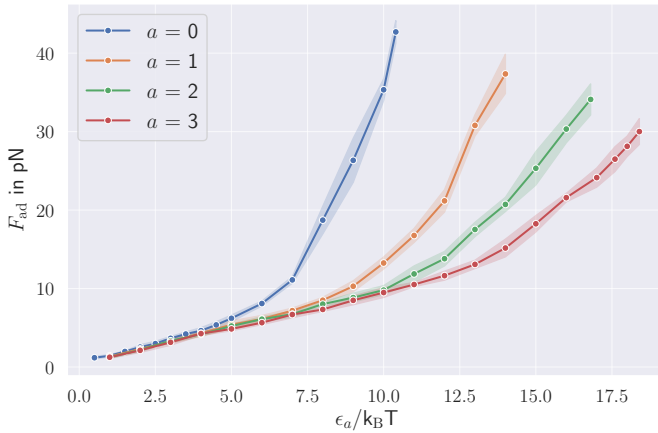


Figure 5.17: Adhesion force as a function of the interaction strength for the different interaction models. The adhesion force depends strongly on the interaction strength and can be tuned to be within the experimental range of 10 pN to 40 pN. For all models, first a linear growth in the adhesion force is observed, while for stronger deformations, the force grows non-linearly. The non-linear part is a result of the deformations, as they increase the interaction area between parasite and membrane.

With this setup, the adhesion force is measured for different interaction strengths and values of a . To exclude the effect of different

points of initial contact and thermal fluctuations, the results shown in fig. 5.17 correspond to the averaged values from multiple simulations. For all interaction models, the measured forces are within the range of 10 pN to 40 pN, which can be tuned by the interaction strength. Similar to the deformation energy, for higher values of a , the adhesion force grows slower with increasing the adhesion strength. In contrast to the deformation energy, the force curve is only linear for small values of ϵ_a . For higher values of ϵ_a , the force grows non-linearly as the induced deformations increase the wrapped area of the parasite.

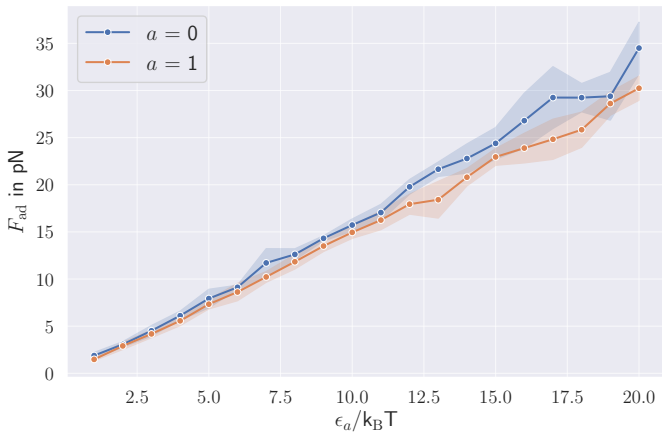


Figure 5.18: Adhesion force as a function of the interaction strength for stiffened RBCs. The membrane stiffness is chosen to be so high that the parasite cannot deform the RBC for the used interaction strengths. As a result, the adhesion force has a linear dependence on ϵ_a .

A positive effect of the RBC deformation in connection to parasite adhesion is verified by introducing a rigid RBC. The shape of the cell stays biconcave and the membrane stiffness is increased by two orders of magnitude. As a result, the parasite does not induce any kind of deformation independent of the interaction strength ϵ_a . The pulling

tests are performed for $a = 0$ and $a = 1$, and the resulting forces are shown in fig. 5.18. For rigid RBCs, the force grows linearly with ϵ_a and no positive feedback for adhesion can be observed, as only a small difference between the interaction models is visible.

5.4.3 Discussion of the Potential Interaction Model

The key aspect studied in this section is the ability of a parasite to induce deformations only through mechanical interactions. We show that this is possible for all investigated interaction models. Furthermore, we show that the levels of deformation can be tuned by the interaction strength and all levels of the experimentally observed deformations can be reproduced. By performing pulling tests, we quantify the strength of the adhesion for different conditions. The resulting forces are within the experimentally measured range of 10 pN to 40 pN, thus the observed behavior is realistic.

A second aspect is whether the passive compliance hypothesis accounts for a positive effect of cell deformation for the parasite adhesion. By probing the adhesion force for both healthy and rigid RBCs, we show that the adhesion strength is enhanced due to cell deformations. The parasite would therefore less likely lose its contact to a RBC due to external perturbations, thanks to the deformability of RBCs.

While the employed interaction gradient models produce similar deformations and adhesion forces as the model for $a = 0$, the resulting visible configurations do not resemble those in the experiments well. As a result, any considerable gradient leads to the alignment of the parasite with the head oriented towards the RBC membrane. The experiment by Crick et al. [77] would be problematic in this case, as the parasite would not be able to adhere to two RBCs at the same time. Therefore we conclude that a (permanent) interaction gradient is likely not a suitable explanation for the alignment behavior of the parasite.

Lastly, we observe that the average alignment respectively reorientation times for all simulated configurations are with $t \ll 0.1$ s much faster than the measured range between 2s and 50s. This observation shows that the potential is too effective in adhering and orientating the parasite to the membrane and is not able to reproduce the correct parasite dynamics.

In summary, the potential interaction model represents some key aspects of the passive compliance hypothesis, but the results do not fully approximate the behavior of parasites observed experimentally.

5.5 Results of the Dynamic Bond Model

In this section, we employ the bond-based interaction model for the parasite-RBC adhesion. We focus mainly on the dynamics of the parasite and its alignment ability. The latter is assessed by three observables: head distance, alignment angle, and alignment time. Furthermore, the effects of the parasite shape and the interaction parameters on the alignment efficiency are studied. Lastly, the effects of membrane fluctuations are considered in this context.

The simulation setup is the same as before such that a parasite and a RBC are brought into interaction range at the beginning of the simulations, leading to the adhesion of the parasite. The main simulation parameters are summarized in table 5.2, while in table 5.4, the additional interaction parameters are listed. The selection of these parameters is not a straightforward task, as no information is available about the kinetics of the agonists that coat the merozoite surface. As a starting point, existing biologically feasible rates are used in this study. The parameters ϵ_0 and σ are used for the repulsive part of the LJ potential. To ensure a hard shell of the parasite, the interaction strength is chosen as high as possible, such that the simulations remain stable. Preliminary tests have shown that the value of the interaction strength does not play an important role for the results discussed in this section. The value of σ is chosen slightly longer than in the previous section to prevent any effect of the discretization.

| Parameter | Simulation Value | Physical Value |
|--------------------------------|------------------|--------------------------------------|
| ϵ_0 | 1000 $k_B T$ | $4.282 \times 10^{-18} \text{ J}$ |
| σ | 0.2 | 0.2 μm |
| $k_{\text{on}}^{\text{long}}$ | 0.05 | 39.6 s^{-1} |
| $k_{\text{on}}^{\text{short}}$ | 0.5 | 396.0 s^{-1} |
| k_{off} | 0.1 | 79.2 s^{-1} |
| λ_{ad} | 100 | $42.82 \text{ pN } \mu\text{m}^{-1}$ |

Table 5.4: Interaction parameters for the bond adhesion model. The parameters are used as a reference configuration and any changes are specified in text.

The on- and off-rates are determined by trial and error. From the first observations of agonists by Bannister et al. [79], the existence of longer and shorter bonds was reported. We choose the on-rates so that $k_{\text{on}}^{\text{short}} = 10k_{\text{on}}^{\text{long}}$, as the number of short bonds is much larger than that of the long ones. The off-rate is important for the observed dynamics. We will discuss its effect later in this section. Lastly, the strength of the bonds is chosen such that the observed deformations are on the same level as for the first model with potential interaction. This is due to the result of the previous section, that the observed levels of deformations are achieved by reasonable binding strengths.

Figure 5.19 shows snapshots of a simulation performed with the parameters from table 5.4. The RBC orientation is adjusted by rotating its main axes in order to obtain an impression of the parasite movement relative to the RBC. In contrast to the simulations performed in section 5.4, the parasite moves dynamically on the membrane and changes its orientation.

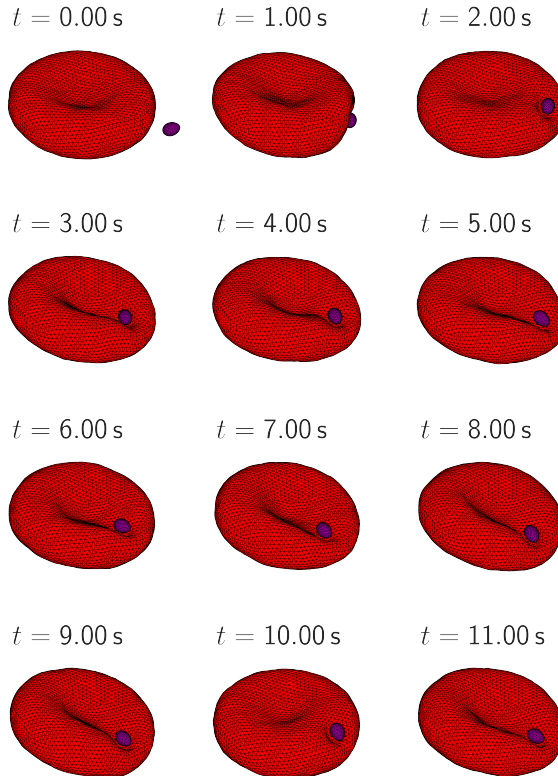


Figure 5.19: Snapshots from one simulation with dynamic bond model. The parasite is brought into contact with the RBC at the beginning of the simulation and interacts with the membrane through long and short bonds. The resulting dynamics is much more vivid than the results shown in section 5.4, as the parasite moves at the surface of the membrane and changes its orientation.

5.5.1 Surface Velocity of an Adhered Parasite

We quantify the dynamics of a parasite by its surface velocity both in experiments and simulations. The velocity is measured by tracking the position of the parasite at fixed time intervals. As the movement process is diffusive, the obtained velocity depends on the time interval. The available experimental videos allow a resolution of $\Delta t = 1$ s. TrackPy in connection with Python3.7 is used to obtain the parasite positions in the videos from Weiss et al. [85]. A number of snapshots with a tracked parasite are shown in fig. 5.20. The data points are obtained only for parasites that are visible over a time of about 10 s and when the corresponding RBC is not moving too much. From the positions, the velocity is calculated as $v = \Delta d / \Delta t$, where Δd is the traveled distance during one time interval.

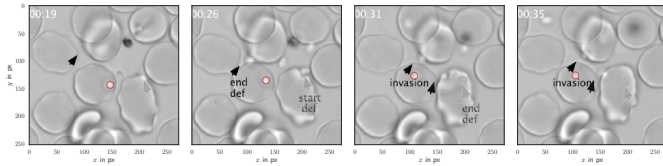


Figure 5.20: Surface velocity of the parasite computed by frame by frame analysis of *in vitro* experiments. The position of the parasite is tracked in 1 s intervals to average out thermal noise. The parasite is tracked using Trackpy with Python3.7. Original video taken from [85] (open access).

In simulations, the required data points are taken from simulated three-dimensional parasite trajectories. To compare the experimental and simulation results, the same time interval is chosen and the measurement is only performed for adhered parasites. To obtain the relative parasite movement in regard to the RBC, the membrane orientation is kept constant for this measurement. As the parasite shows a highly stochastic behavior in experiments and simulations, a range of velocities is measured and their distributions are compared by a

boxplot representation in fig. 5.21, where the median is marked by the central line, the colored area shows the range between the lower and upper quartiles, and the whiskers give the range of the distributions. The plots show a good agreement between the experimental and simulation values, indicating that the model can reproduce the observed experimental behavior.

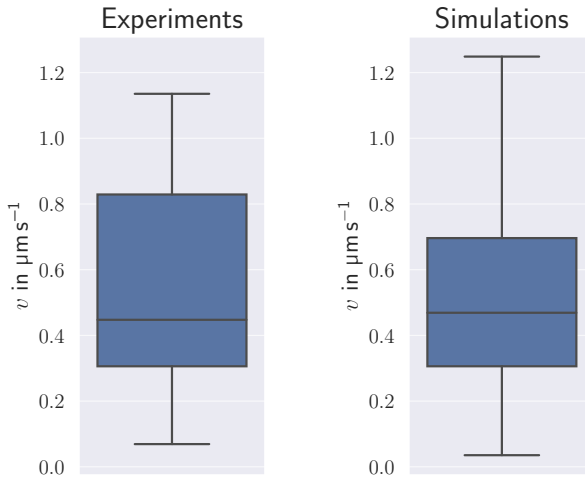


Figure 5.21: Distributions of the surface velocities from experiments and simulations. The distributions are represented by their boxplots, where the line represents the median, the colored area the range between the upper and lower quartiles and the whiskers show the total range of the distribution. A good agreement between experiments and simulations is obtained.

The chosen simulation parameters are a result of trial and error adjustments and therefore the influence of the interaction parameters on the adhesive behavior of the parasite is studied thoroughly in this

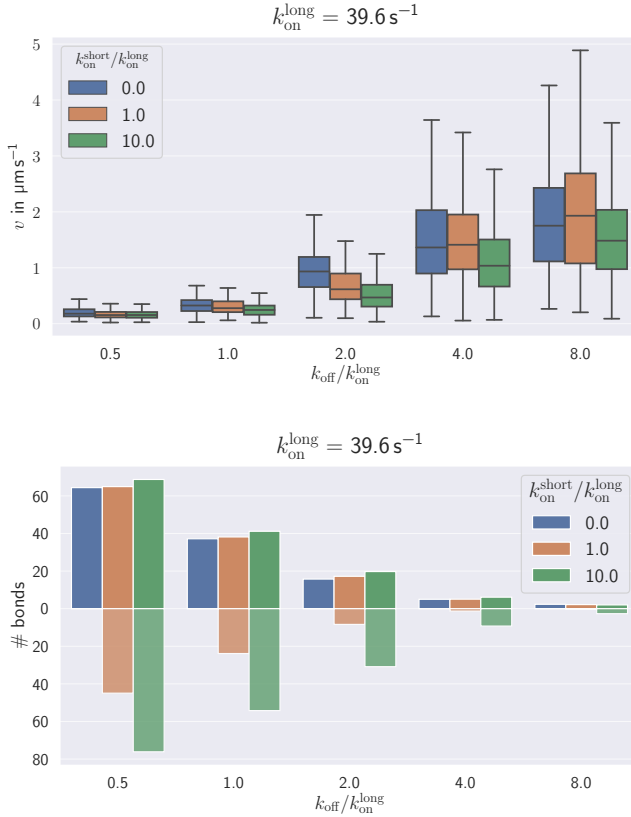


Figure 5.22: Surface velocity and average number of bonds for different cases, where the k_{off} rate is altered for different ratios of $k_{\text{on}}^{\text{short}}/k_{\text{on}}^{\text{long}}$. The average surface velocity decreases with an increased number of bonds. This effect is visible for both bond populations.

section. The parameters in table 5.4 are taken as a reference configuration, since the observed velocities correspond well to the experiments.

The parasite trajectory is dominated by stochastic effects of the interaction and is mainly dependent on the rates $k_{\text{on}}^{\text{long}}$, $k_{\text{on}}^{\text{short}}$, and k_{off} . To study the effect of the bond rates on the surface velocity, the value of $k_{\text{on}}^{\text{long}}$ is kept constant while three parameter sets are tested: only long bonds ($k_{\text{on}}^{\text{short}} = 0$), $k_{\text{on}}^{\text{short}}/k_{\text{on}}^{\text{long}} = 1$, and $k_{\text{on}}^{\text{short}}/k_{\text{on}}^{\text{long}} = 10$. Additionally, k_{off} is altered. For all cases, the surface velocity is measured and the number of bonds is compared in fig. 5.22.

The surface velocity decreases for smaller off-rate values, which can be explained by a larger number of bonds. The number of bonds is shown in the lower part of fig. 5.22, where the upper bars represent the number of long bonds and the bottom bars correspond to the short bonds. In general, a larger number of bonds stabilize the parasite-

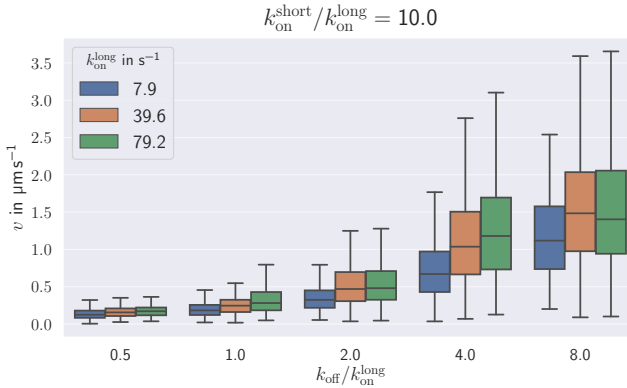


Figure 5.23: Surface velocity for different parameter sets. The color marks different values of $k_{\text{on}}^{\text{long}}$, while the ratio $k_{\text{on}}^{\text{short}}/k_{\text{on}}^{\text{long}} = 10$ is kept constant. In contrast to the measurements in fig. 5.22, a larger number of bonds still lead to a slight increase in the surface velocity. This effect is a result of the crawling motion of the parasite that is affected by the average lifetime of bonds of the two-state interaction model.

membrane connection, thus reducing the surface velocity. For a large

number of bonds, the surface velocity is nearly reduced to zero, reproducing the behavior of the potential interaction model. The stabilizing effect exists for both bond populations and additionally, a small increase in the number of long bonds is observed when more short bonds are formed. Later in this chapter, we will see that a large number of bonds correlates with a higher level of deformation, leading to a larger effective interaction area, similar to the observations in section 5.4.

In fig. 5.23 and fig. 5.24, the ratio $k_{\text{on}}^{\text{short}}/k_{\text{on}}^{\text{long}}$ is kept constant and the absolute values of $k_{\text{on}}^{\text{long}}$ and k_{off} are varied. When the ratio

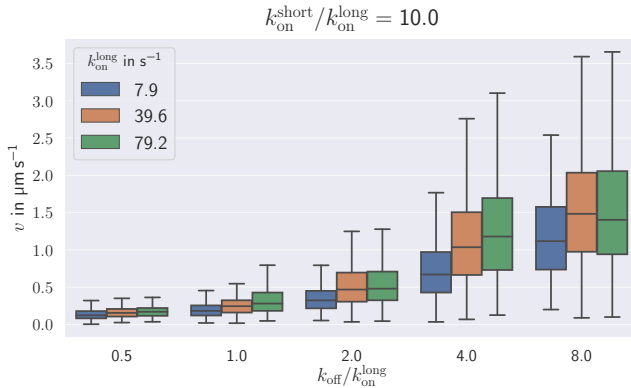


Figure 5.24: Average number of bonds for different parameter sets. The color marks different values of $k_{\text{on}}^{\text{long}}$, while the ratio $k_{\text{on}}^{\text{short}}/k_{\text{on}}^{\text{long}} = 10$ is kept constant. In contrast to the measurements in fig. 5.22, a larger number of bonds still lead to a slight increase in the surface velocity. This effect is a result of the crawling motion of the parasite that is affected by the average lifetime of bonds of the two-state interaction model.

$k_{\text{on}}^{\text{long}}/k_{\text{off}}$ is kept the same, the average number of bonds remains similar for each column. A small increase in the number of bonds for higher values of the on-rate is again a result of stronger deformation.

In contrast to the first measurements in fig. 5.22, the surface velocity can even increase when the number of bonds increases. This is due to the crawling type of motion that is induced by the bond interaction model. At every given time, the parasite may stochastically form new bonds, which pull the parasite away from its current attachment point. When the lifetime of each bond becomes short, this effect gets more pronounced, leading to a larger surface velocity. We refer to this effect in the rest of this chapter as a high turn-over kinetics, since the number of association and dissociation events is increased.

In summary, an increase in the number of bonds has a stabilizing effect onto the surface velocity as the parasite is bound strongly to the membrane. In contrast, when we decrease the average lifetime of the bonds, the surface velocity may increase. The resulting surface velocities compare well to the experimental results, but the introduced reference configuration provides best agreement. Therefore we use it as a starting point for the further analysis.

5.5.2 Parasite Alignment Characteristics

Experimental observations suggest that the alignment of the parasite with its head toward the RBC membrane is a crucial step for a successful invasion. From early experiments, the interaction range of the agonists at the parasite head, which guide the invasion process, is known to be around 8 nm [79]. Recent studies also suggest that the parasite needs to align strictly perpendicular to the membrane surface to achieve successful invasion [84]. We translate these observations into two properties: the head distance d and alignment angle θ . The head distance is defined as the shortest distance between the head of the parasite \mathbf{r}_{head} and the membrane vertices \mathbf{r}_i :

$$d = \min (|\mathbf{r}_{\text{head}} - \mathbf{r}_i|). \quad (5.19)$$

The alignment angle θ is defined as the angle between the directional vector of the parasite (a vector from the center of mass to the head)

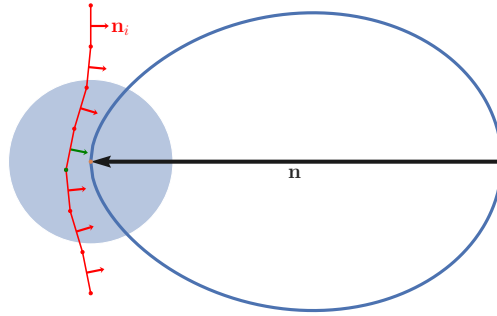


Figure 5.25: Visualization of the head distance and angle measurements. The head distance d is measured between the head of the parasite, marked in orange, and the closest vertex of the membrane surface (green vertex). The alignment angle θ is measured between the directional vector of the parasite (a vector through its head and the center of mass) and the normal vector of a triangle that is closest to the head (green membrane normal vector). Only membrane triangles, which are within the blue circle, corresponding to the cutoff range of long bonds, are considered for the angle measurement. While the sketch is two dimensional, this definition works also in three dimensions.

and the normal vector \mathbf{n}_i of a membrane triangle closest to the parasite head:

$$\theta = \arccos(\mathbf{n}, \mathbf{n}_{\min}). \quad (5.20)$$

The alignment angle cannot be uniquely defined when the head of the parasite is not in close proximity to the membrane, so that only membrane triangles within the interaction range of the head are considered. The interaction range is defined by the maximum length of long bonds. A sketch illustrating the calculation of these two properties is shown in fig. 5.25.

Similar to the surface velocity, both d and θ are well represented by

a distribution. In figs. 5.26 and 5.27, these properties are shown for the reference configuration. These measurements include a number of simulations with the same parameters but varying starting positions.

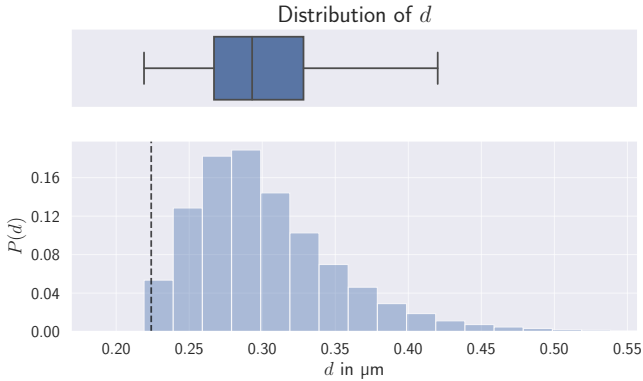


Figure 5.26: Distribution of the head distance d for the reference setup. The histogram shows the full distribution of the distance. The dashed line marks the effective range of the parasite, below which the repulsive part of the LJ potential is applied. The distribution shows that the head of the parasite is within the interaction range of long bonds most of the time. The upper plot shows the corresponding boxplot that will be used for comparison of different parameter sets.

The parasite head distance has a distribution, which spreads from being close to the membrane to being aligned sideways. This stochastic behavior of the head distance d suggests a possible alignment process described by the two-state interaction model: the parasite moves and rotates stochastically at the membrane, allowing a finite probability for the head to get close to the membrane surface. This observation is also confirmed by the alignment angle distribution in fig. 5.27. By definition, a perfect alignment is obtained for $\theta = \pi$. As the angle measurement is performed by considering the orientation of one

membrane triangle, which may not necessarily be positioned centrally in front of the parasite, all values of $\theta \geq 0.8\pi$ are assumed as aligned configurations. Similar to the head distance, the alignment angle distribution yields a finite probability for parasite alignment.

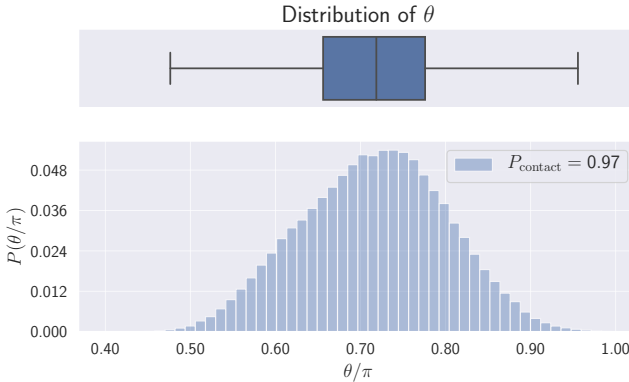


Figure 5.27: Distribution of the alignment angle θ for the reference setup. The histogram shows the total distribution, while the boxplot summarizes the important information that will be used to compare different configurations. Perfect perpendicular alignment is given by $\theta = \pi$, but because of the way the angle is measured, we assume that every angle above 0.8π represents parasite alignment. P_{contact} quantifies how often the parasite head is close enough to the membrane to obtain the alignment angle θ .

The information obtained by the measurements of d and θ is useful to quantify the ability of the parasite to align, but another key aspect is the alignment time. The alignment time is measured as the time interval between the first contact of the two cells and the time, when the parasite first becomes aligned. To achieve successful alignment in

the simulations, two criteria are introduced

$$d \leq 8 \text{ nm}, \quad (5.21)$$

$$\theta \geq 0.8\pi. \quad (5.22)$$

For a number of independent simulations with the reference setup, the alignment time distribution is shown in fig. 5.28.

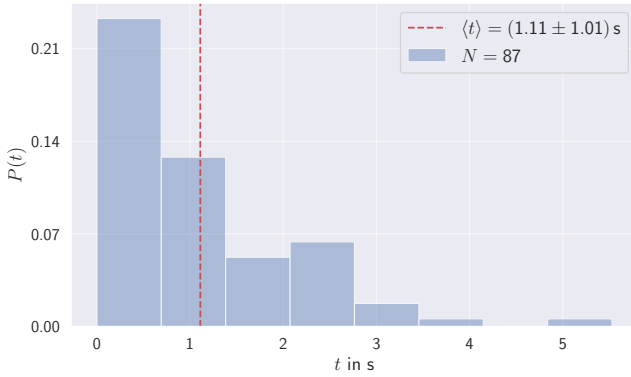


Figure 5.28: Alignment time for the reference configuration. The alignment time is measured by considering the time interval between the first contact of the parasite with the membrane and when the parasite becomes successfully aligned first. The data show that this time is distributed over a broad range, as a result of the stochastic nature of the alignment process.

The alignment time is distributed over a wide range between 0s and 5s. This range is within the experimental range of alignment times. The main limitation of measurement is the computational cost to obtain the distribution. The number of performed simulations is close to 100 and each simulation represent roughly the total time of

$T = 12$ s. The employed fluid model and the RBC require an average simulation time of 3 node hours (or 72 core hours) using JURECA, the supercomputer at Juelich Supercomputing Center. The number of simulations is feasible for one parameter set, but a number of setups are analyzed in the rest of this chapter. Especially, when the average alignment times exceeds $T = 12$ s, the computational cost becomes prohibitive. Therefore, we use an MC simulation approach to obtain relative timescales for different simulation setups.

To perform MC simulations, the phase-space of the two observables d and θ is discretized into a number of states (d_i, θ_j) . The probabilities for each of these states are obtained from long enough simulations of parasite adhesion. Hereby, the angle is measured at every timestep, even when the value becomes difficult to determine uniquely. In fig. 5.29, the resulting two-dimensional probability distribution $P(d_i, \theta_j)$ for the reference configuration is shown. The gray area marks those states, which the parasite never reaches in any simulation.

Using this distribution, a number of MC simulations are performed as follows:

1. To model random first contact, a random point (d_i, θ_j) with $P(d_i, \theta_j) > 0$ of the phase space is chosen as an initial state.
2. The phase space is sampled by allowing jumps between near neighbors. This sampling is done using the Metropolis algorithm and the probability distribution map.
3. The simulation is integrated until a configuration that fulfills the alignment criteria (green area in fig. 5.29) is reached. The number of steps for parasite alignment directly represents the alignment time.

The key part of these simulations is the sampling step. For each MC step, the current state can be switched to a neighboring state. Assuming that the current state is a , the next step can be selected by

1. Proposing one of the neighboring states as the new state. Each

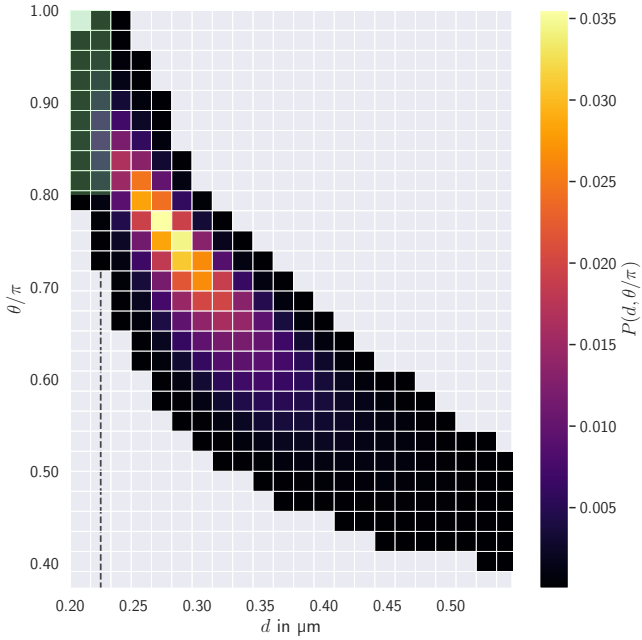


Figure 5.29: Two dimensional probability distribution of (d_i, θ_j) . Each bin represents one state and the color indicates the probability to find the parasite in this configuration. To perform MC simulations, this distribution is used to perform next-neighbor jumps. The green area marks the alignment condition.

direction can be proposed with the same probability. The proposed state is b .

2. Checking if the move is accepted. If $P(b) \geq P(a)$, the move is always accepted. Otherwise, a random number Ξ is drawn and compared against $P(b)/P(a)$. The move is accepted when $\Xi < P(b)/P(a)$ and rejected otherwise.

3. Repeat until the termination condition for alignment is reached.

The described steps correspond to the Metropolis algorithm. It fulfills detailed balance and is an efficient way to sample a given distribution.

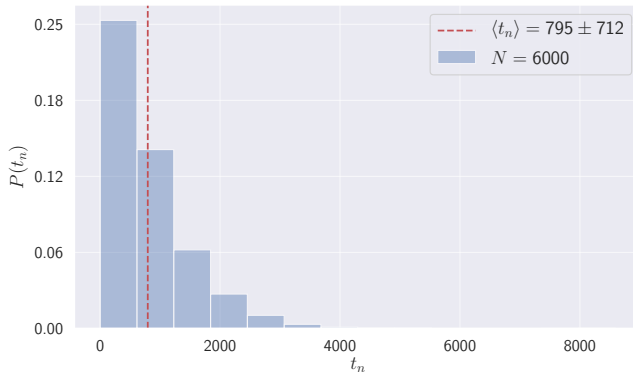


Figure 5.30: Distribution of the alignment times using MC simulations for the reference configuration. The shape of the distribution is similar to that shown in fig. 5.28, but it is much smoother as more samples are used. Since there is no inherent timescale in the MC simulations, the resulting alignment time is represented by the number of steps instead of real times.

The MC simulations are used to sample a larger number of alignment events and the distribution of alignment times for the reference configuration is shown in fig. 5.30. The shape of the distribution is the same as that in fig. 5.28 but it becomes much smoother as more samples are used to create it. As the MC simulations do not have an intrinsic timescale, the resulting times are given by the number of MC steps which are proportional to real alignment time. This is indicated by the subscript n to show the discrete nature of MC results. We study relative differences between different parameter configurations by comparing average alignment times $\langle t_n \rangle$ to the value for the

reference configuration $\langle t_{n,\text{ref}} \rangle$. Thereby, the value $\langle t_n \rangle / \langle t_{n,\text{ref}} \rangle = 1$ corresponds to an alignment time of 1.11 s as shown in fig. 5.28.

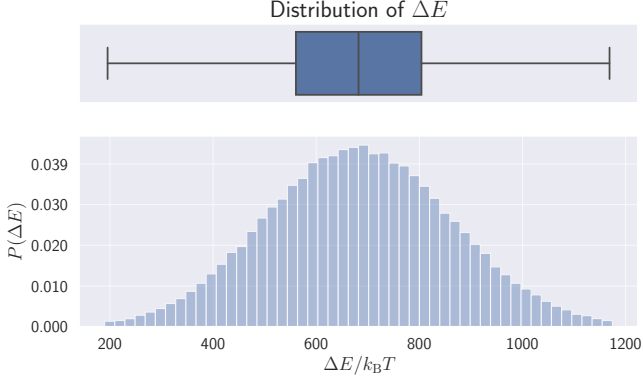


Figure 5.31: Distribution of the deformation energy for the reference configuration. As a result of the dynamic interaction, a broad distribution of energies is observed. Instead of assigning a discrete deformation index to these data, the boxplot will be used to compare deformations for different configurations. In the previous section we identified that $\Delta E \geq 800 \text{ k}_B T$ leads to strong deformations, which are clearly visible at the surface of the membrane.

The parameters d and θ quantify the quality of the parasite alignment. A key question in this chapter is how membrane deformations effect the alignment efficiency. As shown in the previous section, the deformation energy given by eq. (5.16) can be used to measure the levels of deformation. Similar to the other parameters, the energy distribution is measured for each parameter set, as shown in fig. 5.31. The introduced deformation index is not assigned here, as this discrete score cannot capture the energy distribution properly. Instead, such distributions will be used to compare the levels of deformation for different configurations. In section 5.4, we found that a deforma-

tion energy $\Delta E \geq 800 k_B T$ indicates that the deformations start to influence the shape of the membrane. For the distribution shown in fig. 5.31, the parasite induces small deformations most of the time, but as a result of the stochasticity of the two-state interaction model, higher levels of deformation are also observed.

The discussed alignment parameters and distributions show that the employed interaction model represents the alignment of the parasite well. This is mainly a result of the stochasticity of the interaction model, which allows the parasite to reorient constantly while interacting with the RBC. This alignment mechanism agrees well with the experimental observation that alignment is a game of chance [84]. In the rest of this chapter, we study the alignment parameters for different configurations in order to understand the effect of various aspects of the parasite-RBC interaction on to the alignment efficiency.

5.5.3 Effect of the Parasite Shape

The shape of the parasite is pear- or egg-like with a distinctly formed apex structure. Under the assumption that the parasite shape is the result of an evolutionary development, its alignment abilities should be superior in comparison to other shapes such as spheres or ellipsoids.

We introduce four different shapes: a pear-like parasite shape (PA), a spherical parasite shape (SP), a short-ellipsoid parasite shape (ES), and a long-ellipsoid parasite shape (EL) as shown in fig. 5.6 and table 5.1. PA is characterized by a distinct head structure, breaking the symmetry along its long axis. To test the effect of this broken symmetry, ES is chosen to have a similar overall design but head and back are identical. SP has no distinct features and the head is a randomly assigned vertex on its surface. The last tested shape, EL, has the structure of a long rod with the long axis that is double as long as for the original PA. All used shapes have nearly (up to 1%) the same surface area and number of vertices.

The simulations in this section employ the interaction parameters of the reference configuration (see table 5.4) and only k_{off} is varied.

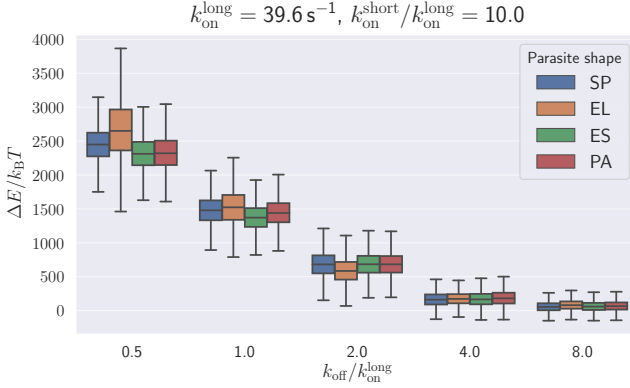


Figure 5.32: Deformation energies for different shapes and different values of k_{off} . As the off-rate controls the average lifetime of the bonds, a smaller value leads to more bonds, stabilizing adhesion. A small k_{off} also leads to stronger deformations, as indicated by the shown energies. Note that the membrane deformation energy appears to be nearly independent of the shape of the parasite.

Generally, less than 30 simulations are performed for each parameter set to obtain smooth enough distributions as illustrated in the previous section. However, for setups with long alignment times, the number of simulations can be larger than 30.

Figure 5.32 shows the deformation energies for all shapes marked by different colors. No significant differences in the deformation energy between the shapes are observed, but the deformations are stronger for lower values of k_{off} . From the discussion about the surface velocity above, we know that smaller values of the off-rate lead to a larger number of formed bonds. This stronger interaction with the membrane leads to more pronounced deformations. Therefore we use the variation of k_{off} to compare setups that show significant deformations with configurations that reproduce the deformation behavior

of the potential-interaction parasite model in order to analyze their effect for the alignment. On average, the head distances shown in

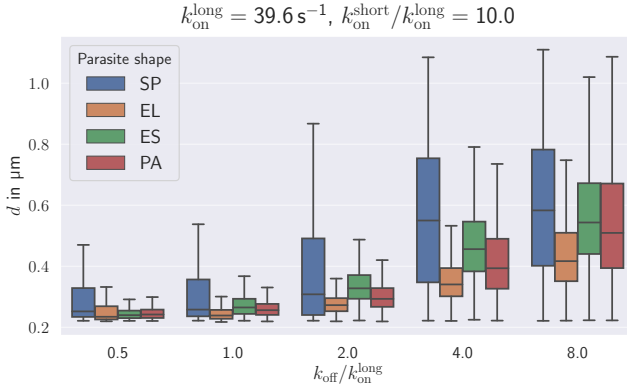


Figure 5.33: Head distance distributions for different shapes (marked by various colors) and different values of k_{off} . For all shapes, the general trend shows a smaller distance for lower values of k_{off} , as the adhesion is more stable, leading to stronger deformations. SP corresponds to the largest distance, as the head is not clearly defined by the shape, leading to a rotation of the parasite throughout the alignment process. EL is found to be frequently attached sideways to the membrane. As the shape is very thin, the head distance d is still small. The ES and PA values for d are in between, with slightly better values of d for the original parasite shape.

fig. 5.33 are smaller for stronger levels of deformation, as a result of the stable adhesion. This positive correlation is a strong indicator that the RBC deformation is indeed very useful for the parasite alignment. The various shapes show different behavior. Since SP does not have any distinct surface features, it rotates arbitrarily while adhered to the membrane. The resulting distribution of the head distance d is therefore very broad and on average the worst of all shapes. The rod-like EL is on the other side of the spectrum. It aligns with its

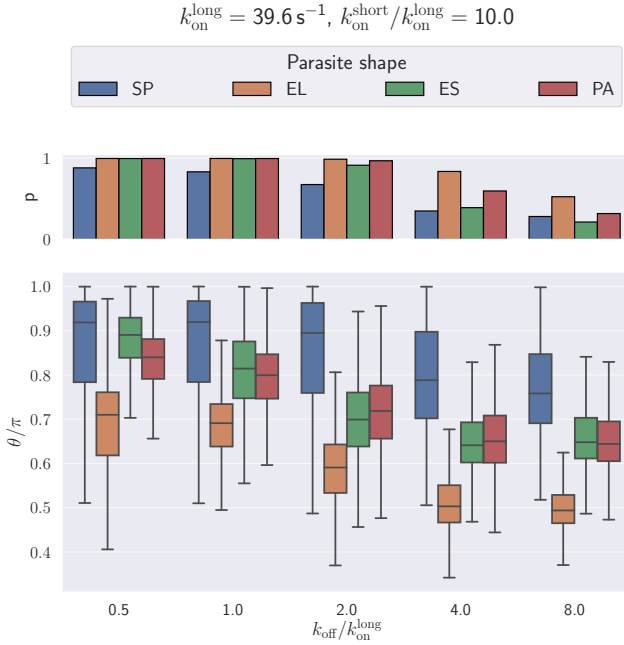


Figure 5.34: Distributions of the alignment angle for the different shapes. The lower part of the plot compares values of the alignment angle θ . The upper part shows the fraction of time when the alignment angle was measured in comparison to the total time of the parasite being bound to the membrane. While SP has the highest values of θ , the head of the parasite is not within the interaction range very frequently in comparison to the other shapes. EL has the highest rate of θ measurements, but the lowest value of the alignment angle. For both shapes, this indicates a poor alignment behavior. ES and PA show similar values for the alignment angle, but a small advantage is noticeable for the parasite shape, indicating that the asymmetric structure aids the alignment.

long-axis parallel to the membrane surface and the head is closest to the membrane because the shape is very thin. The other shapes show a behavior between these two extremes, as they can partly rotate and move, leading to broader distributions than for EL, but profiting from their distinct head structures to obtain on average better d values than SP. A small advantage of the asymmetric PA is observed as ES alternates between an aligned head and back.

To better discuss the alignment angle distributions in fig. 5.34, another measurement is introduced. The values P_{contact} , shown as bars at the top part of the plot, provide the fraction of time that the parasite head is within the interaction range and the alignment angle θ is measured. The results for θ show the same general behavior as the head distance. Whenever the parasite is bound stably to the membrane and induces strong deformations, the quality of the alignment is better, but the results differ for the various shapes. EL, that was best before, has the worst alignment angle, as the parasite adheres with its long axis parallel to the membrane surface and is not able to rotate. In contrast, SP shows the best alignment angle, but it is measured only during a small fraction of the simulation time due to the free rotation of the parasite. PA and ES show a better behavior, as the average alignment angle is close to the targeted value of $\theta = 0.8 \pi$ and the measured fraction of time is reasonably high.

Taking into account both d and θ , the different shapes behave quite distinctly and PA exhibits the best alignment behavior. These results further emphasize that both characteristics are needed to quantify the parasite alignment, such that judging the efficiency by only one of them would miss important aspects for successful alignment.

To finish the shape discussion, the alignment times obtained by MC simulations for all parameter sets are shown in fig. 5.35. The alignment times are compared by the ratio $\langle t_n \rangle / \langle t_{n,\text{ref}} \rangle$, where the reference time is measured for PA. Note that missing bars correspond to configurations that do not lead to the parasite alignment in the original simulations and therefore no pathways into the alignment area exist within the probability distributions. These configurations might still

result in the parasite alignment, but due to the mentioned computational restrictions, the average alignment timescales are too long and cannot be resolved. The absolute values, which significantly exceed the reference time, should also be considered carefully. To obtain reliable distributions, more simulations are performed for such configurations, however the phase-space may still be poorly resolved in comparison to the reference configuration. Therefore, we interpret these times as being quite long for the parasite alignment, but we do not discuss their absolute values.

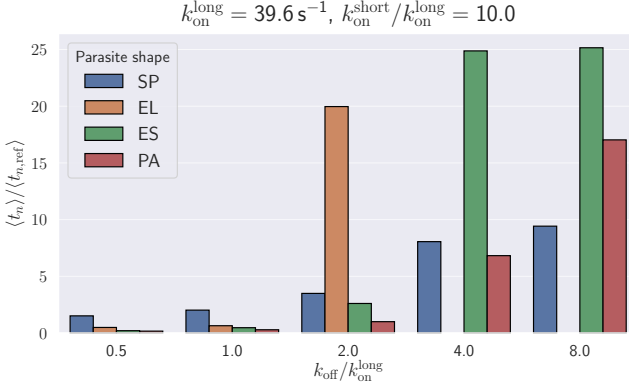


Figure 5.35: Average relative alignment time for different shapes. The missing bars indicate that the parasite is not able to get aligned during simulations. In general, a lower alignment time is found for stronger deformations, since the parasite has a larger contact area with the membrane due to partial wrapping. SP often shows the worst alignment time, but is still successful when there are no deformations, while PA exhibits generally the best alignment time.

The presented results are consistent with the previous discussions such that the alignment probability decreases strongly when the value of k_{off} is increased and the level of deformations decreases. How-

ever, different shapes profit differently from membrane deformations. PA has the shortest alignment times as long as membrane deformations are induced. Only when the parasite is bound loosely to the membrane, SP surpasses PA, as it can rotate more easily around all axes. This free rotation is the reason that the alignment times of the sphere are influenced least by the level of deformations. The other two shapes show reliable alignment only when the induced deformations are strong enough, as this allows to overcome the shape restrictions by strong wrapping of the parasite surface by the membrane.

All studied characteristics lead to the conclusion that membrane deformation is a key aspect for the parasite alignment and the different shapes profit differently from these deformations. From the results for the surface velocity, we know that the configurations for small k_{off} values show nearly no surface movement, reproducing the stable behavior of the potential interaction model. Therefore, the most realistic configurations are found for $k_{\text{off}}/k_{\text{on}}^{\text{long}} \approx 2$, as these show both the parasite dynamics and the membrane deformations similar to experimental observations. For this parameter set, PA exhibits the most efficient alignment behavior, supporting the passive compliance hypothesis as a fundamental mechanism for the parasite-RBC interaction.

5.5.4 Are Different Bond Types Required?

In section 5.5.1, we discussed the effect of different bond populations on the surface velocity and concluded that both, short and long bonds, stabilize the adhesion. Here, we investigate the effect of bonds on the alignment efficiency by considering the various alignment characteristics.

The alignment times and deformation energies shown in fig. 5.36 confirm the general observation that a higher level of deformations leads to a better and faster alignment. Again, this trend is true for both bond populations, as the alignment time is always lower for the configurations marked green.

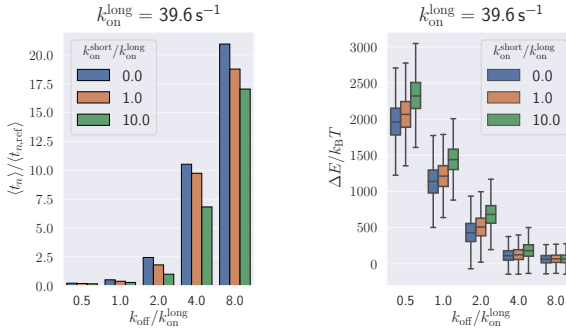


Figure 5.36: Alignment times and deformation energies for different ratios $k_{\text{on}}^{\text{short}} / k_{\text{on}}^{\text{long}}$ for short and long bonds. For all tested values of k_{off} , a higher value of $k_{\text{on}}^{\text{short}}$ leads to shorter alignment times. This observation correlates well with higher deformation energies, as the short bonds exert more force on the RBC membrane.

To test the importance of long bonds, a new setting is studied where $k_{\text{on}}^{\text{long}} = 0 \text{ s}^{-1}$ (no long bonds), while the on-rate for the short bonds is set to the maximum level considered before. To ensure that the parasite is able to interact with the membrane, it is brought into close contact with the membrane at the beginning of the simulation. The resulting alignment times are compared to those for the reference configuration in fig. 5.37 and indicate that only short bonds do not lead to reliable parasite alignment. The parasite cannot be rotated efficiently by the short bonds and the potential energy per bond is small as a result of short bond length. Both effects lead to a significant decrease in the alignment times.

In conclusion, the role of short bonds is purely supportive as they stabilize parasite adhesion, increasing the deformation level and the alignment efficiency, but cannot align the parasite on their own. This observation is consistent with the experimental assumption that the short bonds are damaged longer agonists, which are still attached to

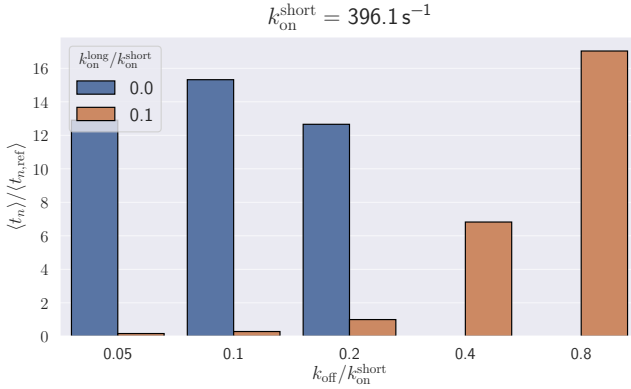


Figure 5.37: Alignment time for a configuration with and without long bonds. When only short bonds interact with the RBC, the parasite is not able to align properly for low k_{off} rates, as the short bonds are not able to dynamically rotate the parasite in the same way the longer bonds do.

the parasite surface [79].

5.5.5 Influence of the Average Bond Lifetime

The absolute values of the different on- and off-rates have a significant effect on the dynamics as we have demonstrated in the first part of this section. The measured alignment time and deformation energies in fig. 5.38 are also influenced by these parameters.

The dependence of the alignment times on k_{off} is consistent with the previous results explained by an increased deformation level. In the case of higher rates or a higher turn-over kinetics of the bonds, the average length of each existing bond is longer. As each bond will relax over its lifetime to exert less amount of force, shorter lifetimes

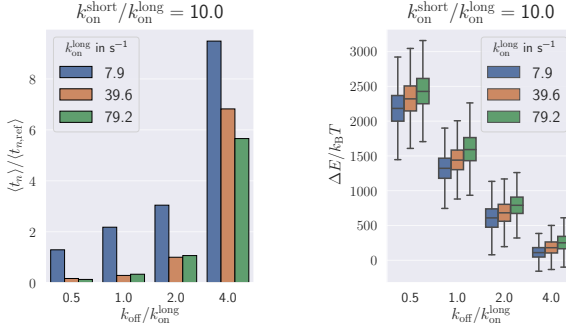


Figure 5.38: Alignment times for different values of $k_{\text{on}}^{\text{long}}$. On average, a higher on-rate leads to smaller alignment times for the same ratios of $k_{\text{off}} / k_{\text{on}}^{\text{long}}$.

allow less relaxation, leading to the elongated springs. As a result, the stress induced at the membrane surface increases with a decrease in bond lifetime, leading to stronger deformations and an improved alignment efficiency.

5.5.6 Rigid RBC Membrane

So far, we focused on the influence of the parasite shape and the interaction parameters on the alignment efficiency. The parasite properties are important for its alignment, but changes in RBC rigidity should also have an effect. In simulations, the membrane does not have any active response to the parasite and is deforming purely through the applied stress. We therefore focus on the effect of RBC rigidity by increasing membrane stiffness by two orders of magnitude. This case mimics rigid RBC, since the parasite is not able to induce any deformations at the cell surface.

The simulations are performed using the interaction parameters

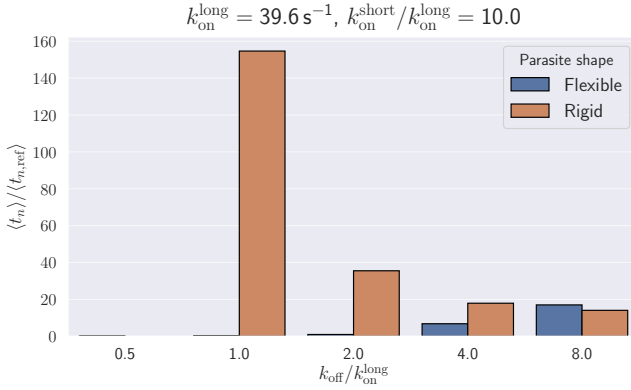


Figure 5.39: Comparison of the alignment times between rigid and flexible RBCs. While for a healthy RBC, an increase in the off-rate leads to longer alignment times, this behavior is opposite for a rigid RBC. It emphasizes the importance of membrane deformations for a successful alignment.

summarized in table 5.4. The alignment times for a rigid RBC are compared to the results for a healthy RBC in fig. 5.39. A clear difference to the previous results is that the alignment time becomes smaller with an increased value of k_{off} instead of larger. As the parasite cannot deform the RBC, it relies on the rotational motion to align itself correctly at the membrane and cannot profit from its shape. Bond interactions support and intensify this motion, but the effect depends on the relation between on- and off-rates, as discussed in the previous sections. The results show that a higher turn-over kinetics without membrane deformations might lead to a slightly more efficient alignment than in case of a stable adhesion between parasite and membrane. However, even in a best case scenario, the average alignment time is more than ten times larger than the alignment time obtained for the reference configuration.

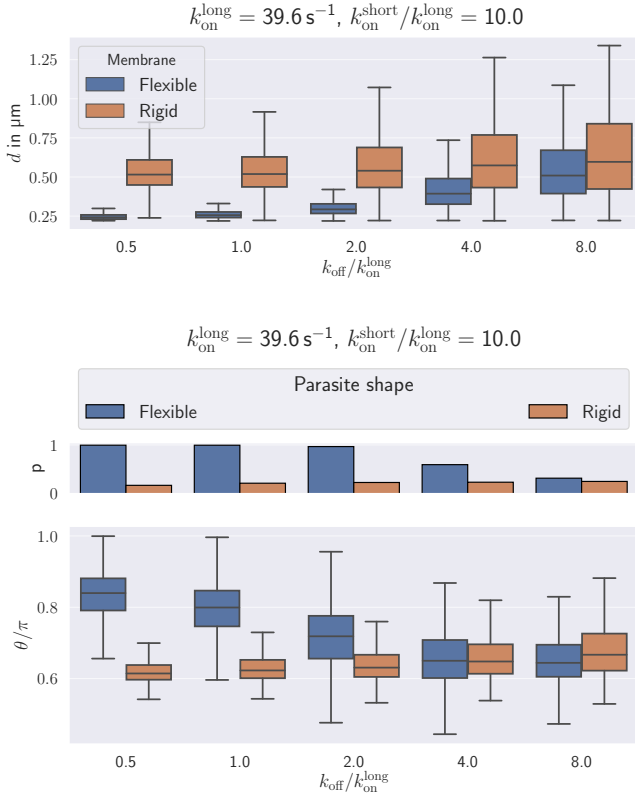


Figure 5.40: Head distance and alignment angle for rigid and flexible RBCs. While the flexible RBC shows a strong dependence on the off-rate, the results for the rigid membrane are on average independent of k_{off} . Only the width of the measured distributions depends on k_{off} , leading to different alignment times for rigid RBCs.

The data in fig. 5.40 supports the hypothesis that membrane de-

formations induced by the parasite are useful and even mandatory for its alignment. The head distance and the alignment angle for healthy and rigid RBCs are very different. While the flexible membrane shows a strong dependence on the value k_{off} and thus on the level of induced deformations, the results for the rigid membrane are on average independent of k_{off} . The similarity in the alignment times for $k_{\text{off}}/k_{\text{on}}^{\text{long}} = 8.0$ are due to the fact that even the flexible RBC is not deforming much for such fast kinetic rates. In conclusion, a rigid RBC significantly suppresses successful parasite alignment.

5.5.7 Discussion of the Dynamic Bond Model

We show in this section that the introduced two-state interaction model for the parasite-RBC adhesion is able to properly reproduce the behavior a merozoite during the pre-alignment stage. Using the surface velocity, we are able to match the general dynamics of the parasite such that visible deformations resemble those in the experiments well.

We introduce the head distance, the alignment angle, and the subsequent alignment time to study the ability of the parasite to align perpendicular to the RBC membrane. We observe that a good alignment is possible, because the mechanism relies on the stochasticity of the model and the resulting alignment times are within the range of experimental observations.

We test the alignment ability for different shapes and find that the experimentally measured egg- or pear-like shape of a parasite exhibits the highest efficiency in aligning the parasite. We also show that both short and long bond populations, which have been observed experimentally [79], have a positive effect on the alignment efficiency. Interestingly a population made of only short bonds is not able to reliably align the parasite.

All performed simulations show a strong, positive correlation between the level of membrane deformation and the ability of the parasite to align. In particular, tests with a rigid RBC indicate that

the deformations are mandatory for an efficient alignment, as without such membrane undulations, the parasite relies on its rotational motion alone and the resulting alignment times are much longer than those measured in the experiments.

5.6 Conclusions

The aim of this chapter is to test the passive compliance hypothesis for the merozoite and RBC interaction. To this end, two *in silico* models are introduced to model the interaction based on this hypothesis. The first focuses on a potential interaction between parasite and membrane, while the second model utilizes two-state, stochastic bonds for the interaction. We performed various simulations using these models to answer three fundamental questions:

1. Can a parasite induce deformations at the level observed in the experiments? If yes, are the interaction strengths required for such deformations realistic?
2. Is an interaction model based on the passive compliance hypothesis able to align the parasite, which is needed for a successful invasion event?
3. Do the observed deformations aid the alignment process of the parasite?

To answer the first question, we focus on the potential interaction model and show that it is able to induce deformations up to very high levels, such that the membrane shape is changed dramatically. We measure the adhesion force between the parasite and RBC and find that it corresponds well to the observed range of 10 pN to 40 pN. Both results support the passive compliance hypothesis in explaining experimental observations. Additionally, tests with a rigid RBC without any deformations show a positive effect on the stability of parasite adhesion.

To discuss the effect of a possible agonist gradient at the surface of the parasite on its alignment, we introduce such a gradient for the interaction potential. While these types of models are still able to reproduce the deformations and adhesion forces, the resulting configurations do not correspond well to the experimental observations. The alignment with such a gradient is too fast in comparison to the experimental observation. Therefore, we conclude that a significant interaction gradient is not realistic.

We tackle the second and third questions using the two-state interaction model. We introduce several characteristics to measure the dynamics and the alignment of the parasite and show that the model is able to successfully and reliably represent the parasite alignment. The alignment time is measured for a configuration, whose parasite dynamics matches the experiments best. The time is established to be about 1 s, which compares well with the experimental value. The mechanism, which leads to the alignment, utilizes the stochasticity of the interaction model, which is in agreement with the assumption that alignment is a game of chance [84]. We discuss the shape of the parasite and find that the egg-like shape, that is measured for merozoites [153], leads to the highest alignment efficiency. This is a strong supporting argument for the passive compliance hypothesis, as we expect the merozoite to have evolved evolutionary into the best possible shape to guarantee alignment.

For all performed simulation setups, we are able to identify a positive correlation between the level of induced deformations and the alignment efficiency. Again, using rigid RBCs, we are able to show that such deformations are indeed mandatory to obtain a reliable alignment, as otherwise the parasite needs to rely on rotational motion alone to align. The resulting alignment times are generally an order of magnitude slower than those with deformations.

In summary, the three key questions are successfully answered using the *in silico* models and support the passive compliance hypothesis as an explanation for the parasite alignment during the pre-invasion stage.

The studied systems have focused so far on the interaction between a single RBC and merozoite. In many *in vitro* and *in vivo* systems, there is a larger number of cells and parasites and a correlation between the cell density and the alignment efficiency is found [86]. The introduced models can be used to study this correlation and elucidate the mechanism that leads to this observation.

For single cell simulations, a more advanced alignment study can be performed. The head, that consists of a single point in the current study, can be modeled more realistically, and the agonists that form a tight junction can be introduced. Additionally, if experiments would provide more data about the nature of the agonist interaction, more precise results can be obtained for the influence of different interaction parameters on parasite alignment.

In contrast to the mentioned *in vitro* experiments, the parasite invasion occurs *in vivo* in a flowing environment. This induces further challenges for the parasite, as the flow changes the behavior of the RBCs and leads to additional forces acting on the parasite-membrane connection. Simulations in this type of environments can be performed to study these effects in more detail.

6 Summary, Conclusions, and Outlook

We study various aspects of cell mechanics and adhesion for different biological processes, such as cell blebbing and the invasion of RBCs by malaria parasites. To this end, we use computer simulations and introduce various coarse-grained cell models that incorporate a number of cell elements, such as a lipid-bilayer membrane and cell cytoskeleton. The models are used within different fluid frameworks and allow us to study cells under realistic conditions.

In chapter 3, we introduce a cell model consisting of a cell membrane and a bulk cytoskeleton. Both are characterized by separate elastic properties and we analyze the elastic response of the cell using microplate compression tests. We systematically study the effect of various membrane and cytoskeletal parameters and show that the total elastic response can be described as a superposition of the individual contributions. This total response is mostly affected by the bulk Young's modulus and the membrane area compression modulus, while other parameters, e.g. the membrane bending rigidity and volume constraint, are negligible.

A further improvement of the studied cell model can be the incorporation of different cell inhomogeneities. These can include structural differences between the area close to the cell membrane and the inside of the cell, e.g. the introduction of a separate cell cortex. Another possibility is to add details about cytoskeletal filaments, for example the different stiffnesses of microtubules, intermediate filaments, and actin filaments. Finally, the addition of a cell core may change the elastic response as well, since a cell nucleus is generally much stiffer than the

surrounding network. The addition of these parts should increase the precision of the model, but will lead to more model parameters and will therefore require a large number of simulations.

The introduced cell model is extended to study stress-induced cell blebbing in chapter 4. By adding network contraction of the bulk cytoskeleton and a dynamic, bond-based adhesion between cell membrane and inner network, this model can produce blebs. Blebs are formed by patches of cell membrane, which detach from the inner network and form a protrusion. By combining theoretical calculations and simulations, we are able to determine parameter ranges in which cell blebbing exists. We find that this process is primarily dominated by the properties of the adhesion model and the membrane stiffness, characterized by the area compression modulus. The relation between the contraction strength of the inner network and the area compression modulus plays a key role in determining the cell shapes and effects the onset of blebbing. Other membrane properties, such as the bending rigidity and volume constraint, are negligible.

By studying the analytical solution, we show that the main aspects of stress-induced blebbing are the number of binding sites within the cell membrane and the kinetic parameters of the adhesive bonds, making blebbing sensitive to the contraction force and average binding rates. A limitation of the introduced model is that a larger number of parameters is needed to describe the adhesion. To verify the model, the results should be combined with future experimental observations to determine a number of these parameters. This model can then be used to study various cell characteristics, such as cell membrane properties.

The used cell-blebbing model is designed to mimic contracting synthetic cells with a volume-spanning actin network. To study blebbing in other contexts, such as cell-motility or cell-division, different types of linker molecules may be needed. One example is catch-bonds, for which the lifetime increases with applied stress. Mixtures of different types of linkers should lead to locally different blebbing behavior and can be important for modeling directed cell motility. The mentioned

inhomogeneities of the cytoskeleton, such as the introduction of a cell nucleus, will also lead to inhomogeneous contraction behavior, affecting the blebbing onset.

In chapter 5, we investigate RBC-membrane deformations due to the interaction with a parasite during a malaria infection. In the blood stage of a human malaria infection, the parasite needs to invade healthy RBCs to reproduce. This invasion process is accompanied by various levels of deformation of the target cell membrane. To test the passive compliance hypothesis, which attributes the deformation to the adhesive interaction between malaria parasite and RBC membrane, we introduce coarse-grained RBC and parasite models.

In the first part of chapter 5, the adhesion is modeled through an attractive potential. We show that the parasite is able to induce deformations of a similar amplitude as observed *in vitro*. By performing parasite pulling tests, we show that the interaction strength required for these deformations leads to realistic detachment forces in the range between 10 pN and 40 pN. We conclude that the passive compliance hypothesis is a feasible explanation for the observed membrane deformations.

In the second part of chapter 5, the adhesion between RBC membrane and the parasite is represented by a dynamic, bond based model. It is a more realistic representation of the parasite-RBC interaction, which is governed by agonists at the parasite surface. The model leads to a realistic dynamics, which includes membrane deformation and parasite movement on the membrane surface.

For successful parasite invasion of RBCs, the parasite head needs to be aligned toward the cell membrane. We quantify the alignment by a number of characteristics such as head distance, alignment angle, and alignment time, and study its dependence on various model aspects. We show that the alignment is a stochastic process and the best alignment behavior is obtained for bonds with a length of approximately 200 nm, since shorter bonds do not induce the parasite motion efficiently. Furthermore, the lifetime of the bonds should be long enough to induce membrane deformations but not too long, so

that the parasite is not permanently adhered to the RBC. This optimized attachment behavior leads to sufficient movement of the parasite, while profiting from the RBC membrane deformations. Additionally, the symmetry-breaking pear-like shape of the parasite leads to the best alignment results. By comparing the alignment behavior for rigid and flexible RBC membranes, we show that the induced deformations are a key aspect for successful parasite alignment, since it allows an effective reorientation of the parasite head.

We conclude from our results, that the passive compliance hypothesis is a plausible explanation for the membrane deformations observed in experiments and that it leads to an effective parasite alignment mechanism. Performed simulations highlight the importance of RBC membrane deformations for successful parasite alignment. The parasite alignment effect needs to be studied *in vitro* and *in vivo* in more detail to explore the possibility of finding a target for the treatment of malaria.

Future studies using such *in silico* models may explore different aspects of adhesion, e.g the number of binding sites at the RBC membrane, the length of the different bonds, and the strength of the interaction bonds. All properties will have an effect on the alignment behavior and testing may identify new ways of future malaria treatment. Additionally, simulations should be performed in a flow environment to study the stability of the adhesion. An important aspect may be the RBC shape, which differs for different confinements and flow speeds. The resulting shapes differ in their surface stresses and are therefore different in their deformation behavior. As a result, the point of first contact might play a more vital role in comparison to the relaxed discocyte shape. Further, experiments show a correlation between the RBC density and the parasite invasion efficiency. This may be explained by an effective stiffening of the RBCs thanks to the increased density. Another possibility is that the malaria parasites interact with more than one RBC at the same time, reducing the effectiveness of the alignment mechanism. Simulations with a larger number of cells and parasites need to be performed for stationary and flowing environments to test this hypotheses.

Bibliography

- ¹H. Gest, *The discovery of microorganisms by Robert Hooke and Antoni van Leeuwenhoek, fellows of the Royal Society*, 2004.
- ²Nobelprize.org, *The Nobel Prize in Physics 2018*, 2018, <https://www.nobelprize.org/prizes/physics/2018/summary/> (visited on 12/19/2018).
- ³A. Hatano et al., “CELLPEDIA: A repository for human cell information for cell studies and differentiation analyses”, Database **2011** (2011).
- ⁴R. Sender, S. Fuchs, and R. Milo, “Revised Estimates for the Number of Human and Bacteria Cells in the Body”, PLOS Biology **14**, e1002533 (2016).
- ⁵B. Alberts et al., *Molecular Biology of the Cell*, 6th editio (2014).
- ⁶M. Ruiz, *Cell membrane detailed diagram en.svg - Wikimedia Commons*, 2007, https://commons.wikimedia.org/wiki/File:Cell%7B%5C_%7Dmembrane%7B%5C_%7Ddetailed%7B%5C_%7Ddiagram%7B%5C_%7Den.svg (visited on 12/19/2018).
- ⁷A. Pohorille, K. Schweighofer, and M. A. Wilson, “The Origin and Early Evolution of Membrane Channels”, *Astrobiology* **5**, 1–17 (2005).
- ⁸E. Wallin and G. von Heijne, “Genome-wide analysis of integral membrane proteins from eubacterial, archaean, and eukaryotic organisms.”, *Protein science : a publication of the Protein Society* **7**, 1029–1038 (1998).
- ⁹J. Iwasa, W. F. Marshall, and G. Karp, *Karp’s cell and molecular biology : concepts and experiments*, 8th editio (Wiley, 2015), p. 832.
- ¹⁰W. Helfrich, “Elastic Properties of Lipid Bilayers: Theory and Possible Experiments”, *Zeitschrift für Naturforschung C* **28**, 693–703 (1973).
- ¹¹L. Bo and R. E. Waugh, “Determination of bilayer membrane bending stiffness by tether formation from giant, thin-walled vesicles”, *Biophysical Journal* (1989).

- ¹²J. Hardin et al., *Becker's world of the cell*, 8th editio (Benjamin Cummings, 2012).
- ¹³W. Rasband, *ImageJ*, <https://imagej.nih.gov/ij/images/FluorescentCells.jpg> (visited on 12/19/2018).
- ¹⁴C. A. Schneider, W. S. Rasband, and K. W. Eliceiri, "NIH Image to ImageJ: 25 years of image analysis", *Nature Methods* (2012).
- ¹⁵D. A. Fletcher and R. D. Mullins, *Cell mechanics and the cytoskeleton*, 2010.
- ¹⁶R. De, A. Zemel, and S. A. Safran, *Theoretical Concepts and Models of Cellular Mechanosensing* (2010).
- ¹⁷H. De Forges, A. Bouissou, and F. Perez, "Interplay between microtubule dynamics and intracellular organization", *International Journal of Biochemistry and Cell Biology* (2012).
- ¹⁸H. F. Lodish, *Molecular Cell Biology* (W.H. Freeman and Co., 2013).
- ¹⁹D. Kristofferson, T. Mitchison, and M. Kirschner, "Direct observation of steady-state microtubule dynamics", *Journal of Cell Biology* (1986).
- ²⁰N. Hirokawa, *Kinesin and dynein superfamily proteins and the mechanism of organelle transport*, 1998.
- ²¹D. J. Sharp, G. C. Rogers, and J. M. Scholey, *Microtubule motors in mitosis*, 2000.
- ²²H. Herrmann et al., *Intermediate filaments: From cell architecture to nanomechanics*, 2007.
- ²³S. Pellegrin and H. Mellor, "Actin stress fibres", *Journal of Cell Science* (2007).
- ²⁴J. T. Finer, R. M. Simmons, and J. A. Spudich, "Single myosin molecule mechanics: Piconewton forces and nanometre steps", *Nature* (1994).
- ²⁵U. S. Schwarz and S. A. Safran, "Physics of adherent cells", *Reviews of Modern Physics* **85**, 1327–1381 (2013).
- ²⁶M. Mak et al., "Interplay of active processes modulates tension and drives phase transition in self-renewing, motor-driven cytoskeletal networks", *Nature Communications* (2016).
- ²⁷E. Gladilin, P. Gonzalez, and R. Eils, "Dissecting the contribution of actin and vimentin intermediate filaments to mechanical phenotype of suspended cells using high-throughput deformability measurements and computational modeling", *Journal of Biomechanics* (2014).

-
- ²⁸N. Guz et al., “If Cell Mechanics Can Be Described by Elastic Modulus: Study of Different Models and Probes Used in Indentation Experiments”, *Biophysical Journal* **107**, 564–575 (2014).
- ²⁹F. Yoshida, T. Uemori, and K. Fujiwara, “Elastic-plastic behavior of steel sheets under in-plane cyclic tension-compression at large strain”, *International journal of plasticity* (2002).
- ³⁰T. W. Secomb, “Mechanics and computational simulation of blood flow in microvessels”, *Medical Engineering and Physics* **33**, 800–804 (2011).
- ³¹G. J. Bosman, F. L. Willekens, and J. M. Werre, *Erythrocyte aging: A more than superficial resemblance to apoptosis?*, 2005.
- ³²M. L. Rodriguez, P. J. McGarry, and N. J. Sniadecki, “Review on Cell Mechanics: Experimental and Modeling Approaches”, *Applied Mechanics Reviews* **65**, 060801 (2013).
- ³³S. E. Cross et al., “Nanomechanical analysis of cells from cancer patients”, *Nature Nanotechnology* (2007).
- ³⁴T. G. Kuznetsova et al., “Atomic force microscopy probing of cell elasticity”, *Micron* (2007).
- ³⁵S. Hiratsuka et al., “The number distribution of complex shear modulus of single cells measured by atomic force microscopy”, *Ultramicroscopy* (2009).
- ³⁶J. M. Maloney et al., “Mesenchymal stem cell mechanics from the attached to the suspended state”, *Biophysical Journal* (2010).
- ³⁷M. Lekka et al., “Elasticity of normal and cancerous human bladder cells studied by scanning force microscopy”, *European Biophysics Journal* (1999).
- ³⁸A. Ashkin, “Acceleration and Trapping of Particles by Radiation Pressure”, *Physical Review Letters* (1970).
- ³⁹A. Ashkin, *Applications of laser radiation pressure*, 1980.
- ⁴⁰S. Hénon et al., “A new determination of the shear modulus of the human erythrocyte membrane using optical tweezers”, *Biophysical Journal* **76**, 1145–1151 (1999).
- ⁴¹G. Lenormand et al., “Direct Measurement of the Area Expansion and Shear Moduli of the Human Red Blood Cell Membrane Skeleton”, *Biophysical Journal* **81**, 43–56 (2001).

- ⁴²M. Dao, C. T. Lim, and S. Suresh, “Mechanics of the human red blood cell deformed by optical tweezers”, *Journal of the mechanics and physics of solids* (2003).
- ⁴³J. Guck et al., “Optical deformability as an inherent cell marker for testing malignant transformation and metastatic competence”, *Biophysical Journal* (2005).
- ⁴⁴B. Lincoln et al., *High-Throughput Rheological Measurements with an Optical Stretcher*, 2007.
- ⁴⁵M. K. Kreysing et al., “The optical cell rotator”, *Optics Express* (2008).
- ⁴⁶I. Sraj et al., “Cell deformation cytometry using diode-bar optical stretchers”, *Journal of Biomedical Optics* (2010).
- ⁴⁷T. R. Strick et al., “The elasticity of a single supercoiled DNA molecule”, *Science* (1996).
- ⁴⁸V. Heinrich and R. E. Waugh, “A piconewton force transducer and its application to measurement of the bending stiffness of phospholipid membranes”, *Annals of Biomedical Engineering* (1996).
- ⁴⁹R. J. Mannix et al., “Nanomagnetic actuation of receptor-mediated signal transduction”, *Nature Nanotechnology* (2008).
- ⁵⁰P. Tseng, J. W. Judy, and D. Di Carlo, “Magnetic nanoparticle-mediated massively parallel mechanical modulation of single-cell behavior”, *Nature Methods* (2012).
- ⁵¹C. D. McCaig, “Controlling Cell Behavior Electrically: Current Views and Future Potential”, *Physiological Reviews* (2005).
- ⁵²M. Hronik-Tupaj and D. L. Kaplan, “A Review of the Responses of Two- and Three-Dimensional Engineered Tissues to Electric Fields”, *Tissue Engineering Part B: Reviews* (2012).
- ⁵³C. Campbell and J. C. Burgess, “Surface Acoustic Wave Devices and Their Signal Processing Applications”, *The Journal of the Acoustical Society of America* (1991).
- ⁵⁴J. Shi et al., “Acoustic tweezers: Patterning cells and microparticles using standing surface acoustic waves (SSAW)”, *Lab on a Chip* (2009).
- ⁵⁵X. Ding et al., “On-chip manipulation of single microparticles, cells, and organisms using surface acoustic waves”, *Proceedings of the National Academy of Sciences* (2012).

- ⁵⁶P. F. Davies, “Flow-mediated endothelial mechanotransduction”, *Physiological Reviews* (1995).
- ⁵⁷G. G. Galbraith, R. Skalak, and S. Chien, “Shear stress induces spatial reorganization of the endothelial cell cytoskeleton”, *Cell Motility and the Cytoskeleton* (1998).
- ⁵⁸S. Li et al., “Distinct roles for the small GTPases Cdc42 and Rho in endothelial responses to shear stress”, *Journal of Clinical Investigation* (1999).
- ⁵⁹J. P. Shelby et al., “A microfluidic model for single-cell capillary obstruction by *Plasmodium falciparum*-infected erythrocytes”, *Proceedings of the National Academy of Sciences* (2003).
- ⁶⁰M. Abkarian, M. Faivre, and H. A. Stone, “High-speed microfluidic differential manometer for cellular-scale hydrodynamics”, *Proceedings of the National Academy of Sciences* (2006).
- ⁶¹M. J. Rosenbluth, W. A. Lam, and D. A. Fletcher, “Analyzing cell mechanics in hematologic diseases with microfluidic biophysical flow cytometry”, *Lab on a Chip* (2008).
- ⁶²J. C. del Alamo et al., “Anisotropic rheology and directional mechanotransduction in vascular endothelial cells”, *Proceedings of the National Academy of Sciences* (2008).
- ⁶³H. Bow et al., “A microfabricated deformability-based flow cytometer with application to malaria”, *Lab on a chip* (2011).
- ⁶⁴P. Pereira et al., “Microfluidic tools to investigate pathologies in the blood microcirculation”, *International Journal of Nanotechnology* (2012).
- ⁶⁵P. Español, “Fluid particle model”, *Physical Review E* **57**, 2930–2948 (1998).
- ⁶⁶V. Lulevich et al., “Cell Mechanics Using Atomic Force Microscopy-Based Single-Cell Compression”, *Langmuir* **22**, 8151–8155 (2006).
- ⁶⁷S. R. Mulay et al., “Membrane blebbing during apoptosis results from caspase-mediated activation of ROCK I”, *Nature Cell Biology* **3**, 339–345 (2001).
- ⁶⁸J. C. Mills et al., “Apoptotic membrane blebbing is regulated by myosin light chain phosphorylation”, *Journal of Cell Biology* **140**, 627–636 (1998).

- ⁶⁹L. L. Norman et al., “Cell blebbing and membrane area homeostasis in spreading and retracting cells”, *Biophysical Journal* **99**, 1726–1733 (2010).
- ⁷⁰J. Sedzinski et al., “Polar actomyosin contractility destabilizes the position of the cytokinetic furrow”, *Nature* **476**, 462–468 (2011).
- ⁷¹G. Charras and E. Paluch, “Blebs lead the way: How to migrate without lamellipodia”, *Nature Reviews Molecular Cell Biology* **9**, 730–736 (2008).
- ⁷²O. T. Fackler and R. Grosse, “Cell motility through plasma membrane blebbing”, *Journal of Cell Biology* **181**, 879–884 (2008).
- ⁷³E. K. Paluch and E. Raz, “The role and regulation of blebs in cell migration”, *Current Opinion in Cell Biology* **25**, 582–590 (2013).
- ⁷⁴E. Loiseau et al., “Shape remodeling and blebbing of active cytoskeletal vesicles”, *Science Advances* **2**, e1500465 (2016).
- ⁷⁵G. I. Bell, “Models for the specific adhesion of cells to cells”, *Science* **200**, 618–627 (1978).
- ⁷⁶L. H. Miller et al., “The pathogenic basis of malaria”, *Nature* **415**, 673–679 (2002).
- ⁷⁷A. J. Crick et al., “Quantitation of malaria parasite-erythrocyte cell-cell interactions using optical tweezers”, *Biophysical Journal* **107**, 846–853 (2014).
- ⁷⁸J. A. Dvorak et al., “Invasion of erythrocytes by malaria merozoites”, *Science* **187**, 748–750 (1975).
- ⁷⁹L. H. Bannister et al., “Structure and development of the surface coat of erythrocytic merozoites of *Plasmodium knowlesi*”, *Cell and Tissue Research* **245**, 281–290 (1986).
- ⁸⁰S. Glushakova et al., “Membrane transformation during malaria parasite release from human red blood cells”, *Current Biology* **15**, 1645–1650 (2005).
- ⁸¹V. L. Lew and T. Tiffert, “Is invasion efficiency in malaria controlled by pre-invasion events?”, *Trends in Parasitology* **23**, 481–484 (2007).
- ⁸²P. R. Gilson and B. S. Crabb, “Morphology and kinetics of the three distinct phases of red blood cell invasion by *Plasmodium falciparum* merozoites”, *International Journal for Parasitology* **39**, 91–96 (2009).

-
- ⁸³A. J. Crick et al., “An Automated Live Imaging Platform for Studying Merozoite Egress-Invasion in Malaria Cultures”, *Biophysical Journal* **104**, 997–1005 (2013).
- ⁸⁴M. Koch and J. Baum, “The mechanics of malaria parasite invasion of the human erythrocyte - towards a reassessment of the host cell contribution”, *Cellular Microbiology* **18**, 319–329 (2016).
- ⁸⁵G. E. Weiss et al., “Revealing the Sequence and Resulting Cellular Morphology of Receptor-Ligand Interactions during *Plasmodium falciparum* Invasion of Erythrocytes”, *PLoS Pathogens* **11**, edited by M. J. Blackman, e1004670 (2015).
- ⁸⁶V. Introini et al., “Evidence against a Role of Elevated Intracellular Ca^{2+} during *Plasmodium falciparum* Preinvasion”, *Biophysical Journal* **114**, 1695–1706 (2018).
- ⁸⁷M. Matsui and M. Akaogi, “Molecular dynamics simulation of the structural and physical properties of the four polymorphs of tio_2 ”, *Molecular Simulation* (1991).
- ⁸⁸M. Matsui, S. C. Parker, and M. Leslie, “The MD simulation of the equation of state of MgO : Application as a pressure calibration standard at high temperature and high pressure”, *American Mineralogist* (2000).
- ⁸⁹R. Komanduri, N. Chandrasekaran, and L. M. Raff, “M.D. simulation of nanometric cutting of single crystal aluminum-effect of crystal orientation and direction of cutting”, *Wear* (2000).
- ⁹⁰R. Komanduri, N. Chandrasekaran, and L. M. Raff, “Molecular Dynamics (MD) simulation of uniaxial tension of some single-crystal cubic metals at nanolevel”, *International Journal of Mechanical Sciences* (2001).
- ⁹¹D. Idrees et al., “Spectroscopic and MD simulation studies on unfolding processes of mitochondrial carbonic anhydrase VA induced by urea”, *Journal of Biomolecular Structure and Dynamics* (2016).
- ⁹²J. Šponer et al., “Folding of guanine quadruplex molecules—funnel-like mechanism or kinetic partitioning? An overview from MD simulation studies”, *Biochimica et Biophysica Acta - General Subjects* (2017).
- ⁹³F. Meng et al., “Highly Disordered Amyloid- β Monomer Probed by Single-Molecule FRET and MD Simulation”, *Biophysical Journal* (2018).
- ⁹⁴L. P. Franca and S. L. Frey, “Stabilized finite element methods: II. The incompressible Navier-Stokes equations”, *Computer Methods in Applied Mechanics and Engineering* (1992).

- ⁹⁵R. Rannacher, “Finite Element Methods for the Incompressible Navier-Stokes Equations”, *Fundamental directions in mathematical fluid mechanics* (2000).
- ⁹⁶T. A. Oliver, “A High-Order, Adaptive, Discontinuous Galerkin Finite Element Method for the Reynolds-Averaged Navier-Stokes Equations”, *Massachusetts Institute of Technology S.B. Massachusetts Institute of Technology* (2004).
- ⁹⁷J. Camaño and R. Oyarzúa, “Analysis of an augmented mixed-FEM for the Navier-Stokes”, *Mathematics of Computation* (2017).
- ⁹⁸T. P. Fries, “Higher-order surface FEM for incompressible Navier-Stokes flows on manifolds”, *International Journal for Numerical Methods in Fluids* (2018).
- ⁹⁹H. Noguchi and G. Gompper, “Fluid vesicles with viscous membranes in shear flow”, *Physical Review Letters* (2004).
- ¹⁰⁰J. L. McWhirter, H. Noguchi, and G. Gompper, “Flow-induced clustering and alignment of vesicles and red blood cells in microcapillaries”, *Proceedings of the National Academy of Sciences* (2009).
- ¹⁰¹H. Takeda, S. M. Miyama, and M. Sekiya, “Numerical Simulation of Viscous Flow by Smoothed Particle Hydrodynamics”, *Progress of Theoretical Physics* (1994).
- ¹⁰²K.-i. TSUBOTA, S. WADA, and T. YAMAGUCHI, “Simulation Study on Effects of Hematocrit on Blood Flow Properties Using Particle Method”, *Journal of Biomechanical Science and Engineering* (2006).
- ¹⁰³P. Van Liedekerke et al., “Solving microscopic flow problems using Stokes equations in SPH”, *Computer Physics Communications* (2013).
- ¹⁰⁴S. M. Hosseini and J. J. Feng, “How malaria parasites reduce the deformability of infected red blood cells”, *Biophysical Journal* (2012).
- ¹⁰⁵G. R. McNamara and G. Zanetti, “Use of the boltzmann equation to simulate lattice-gas automata”, *Physical Review Letters* (1988).
- ¹⁰⁶E. J. Ding and C. K. Aidun, “Extension of the Lattice-Boltzmann Method for Direct Simulation of Suspended Particles Near Contact”, *Journal of Statistical Physics* (2003).
- ¹⁰⁷C. K. Aidun and J. R. Clausen, “Lattice-Boltzmann Method for Complex Flows”, *Annual Review of Fluid Mechanics* (2010).

-
- ¹⁰⁸F. Janoschek et al., “Rotational behaviour of red blood cells in suspension: A mesoscale simulation study”, *Philosophical transactions of the royal society a: mathematical, physical and engineering sciences* (2011).
- ¹⁰⁹R. D. Groot and P. B. Warren, “Dissipative particle dynamics: Bridging the gap between atomistic and mesoscopic simulation”, *Journal of Chemical Physics* **107**, 4423–4435 (1997).
- ¹¹⁰D. A. Fedosov, B. Caswell, and G. E. Karniadakis, “A multiscale red blood cell model with accurate mechanics, rheology, dynamics”, *Biophysical Journal* **98**, 2215–2225 (2010).
- ¹¹¹D. A. Fedosov, B. Caswell, and G. E. Karniadakis, “Reverse poiseuille flow: the numerical viscometer”, *Aip conference proceedings*, Vol. 1027 (2008), pp. 1432–1434.
- ¹¹²R. L. Satcher and C. F. Dewey, “Theoretical estimates of mechanical properties of the endothelial cell cytoskeleton”, *Biophysical Journal* (1996).
- ¹¹³D. Stamenović et al., “A microstructural approach to cytoskeletal mechanics based on tensegrity”, *Journal of Theoretical Biology* (1996).
- ¹¹⁴S. K. Boey, D. H. Boal, and D. E. Discher, “Simulations of the erythrocyte cytoskeleton at large deformation. I. Microscopic models”, *Biophysical Journal* **75**, 1573–1583 (1998).
- ¹¹⁵D. Stamenović and D. E. Ingber, “Models of cytoskeletal mechanics of adherent cells”, *Biomechanics and Modeling in Mechanobiology* (2002).
- ¹¹⁶M. F. Coughlin and D. Stamenović, “A prestressed cable network model of the adherent cell cytoskeleton”, *Biophysical Journal* (2003).
- ¹¹⁷J. Li et al., “Spectrin-level modeling of the cytoskeleton and optical tweezers stretching of the erythrocyte”, *Biophysical Journal* (2005).
- ¹¹⁸C. Lim, E. Zhou, and S. Quek, “Mechanical models for living cells—a review”, *Journal of Biomechanics* **39**, 195–216 (2006).
- ¹¹⁹H. Si, “TetGen, a Delaunay-Based Quality Tetrahedral Mesh Generator”, *ACM Transactions on Mathematical Software* (2015).
- ¹²⁰M. Kot, H. Nagahashi, and P. Szymczak, “Elastic moduli of simple mass spring models”, *Visual Computer* **31**, 1339–1350 (2015).
- ¹²¹L. D. Landau and E. M. Lifshitz, *Theory of Elasticity* (Butterworth-Heinemann, 1970), p. 187.

- ¹²²B. P. Chan et al., “A microplate compression method for elastic modulus measurement of soft and viscoelastic collagen microspheres”, *Annals of Biomedical Engineering* **36**, 1254–1267 (2008).
- ¹²³H. Noguchi and G. Gompper, “Dynamics of fluid vesicles in shear flow: Effect of membrane viscosity and thermal fluctuations”, *Physical Review E - Statistical, Nonlinear, and Soft Matter Physics* **72** (2005).
- ¹²⁴D. A. Fedosov, M. Peltomäki, and G. Gompper, “Deformation and dynamics of red blood cells in flow through cylindrical microchannels”, *Soft Matter* **10**, 4258–4267 (2014).
- ¹²⁵V. V. Lulevich, D. Andrienko, and O. I. Vinogradova, “Elasticity of polyelectrolyte multilayer microcapsules”, *Journal of Chemical Physics* **120**, 3822–3826 (2004).
- ¹²⁶M. Dogterom and G. Koenderink, “Cell-membrane mechanics: Vesicles in and tubes out”, *Nature Materials* **10**, 561–562 (2011).
- ¹²⁷M. P. Sheetz, “Cell control by membrane-cytoskeleton adhesion”, *Nature Reviews Molecular Cell Biology* **2**, 392–396 (2001).
- ¹²⁸R. Alert and J. Casademunt, “Bleb nucleation through membrane peeling”, *Physical Review Letters* **116**, 068101 (2016).
- ¹²⁹R. Merkel et al., “Energy landscapes of receptor-ligand bonds explored with dynamic force spectroscopy”, *Nature* **397**, 50–53 (1999).
- ¹³⁰C. Verbelen, H. J. Gruber, and Y. F. Dufre ne, “The NTA-His6 bond is strong enough for AFM single-molecular recognition studies”, *Journal of Molecular Recognition* **20**, 490–494 (2007).
- ¹³¹P. Hanggi, P. Talkner, and M. Borkovec, “Reaction-rate theory: Fifty years after Kramers”, *Reviews of Modern Physics* **62**, 251–341 (1990).
- ¹³²E. Evans and K. Ritchie, “Dynamic strength of molecular adhesion bonds”, *Biophysical Journal* **72**, 1541–1555 (1997).
- ¹³³E. A. Evans and D. A. Calderwood, “Forces and bond dynamics in cell adhesion”, *Science* **316**, 1148–1153 (2007).
- ¹³⁴T. Erdmann and U. S. Schwarz, “Stochastic dynamics of adhesion clusters under shared constant force and with rebinding”, *Journal of Chemical Physics* **121**, 8997–9017 (2004).
- ¹³⁵A. Meurer et al., “SymPy: symbolic computing in Python”, *PeerJ Computer Science* **3**, e103 (2017).

- ¹³⁶R. Alert et al., “Model for Probing Membrane-Cortex Adhesion by Micropipette Aspiration and Fluctuation Spectroscopy”, *Biophysical Journal* **108**, 1878–1886 (2015).
- ¹³⁷World Health Organisation, *WHO | Number of Malaria Deaths*, 2013.
- ¹³⁸S. Suresh et al., “Reprint of: Connections between single-cell biomechanics and human disease states: Gastrointestinal cancer and malaria”, *Acta Biomaterialia* **23**, S3–S15 (2015).
- ¹³⁹G. Y. H. Lee and C. T. Lim, “Biomechanics approaches to studying human diseases”, *Trends in Biotechnology* (2007).
- ¹⁴⁰D. A. Fedosov, “In silico modeling of malaria and sickle-cell disease”, *Drug Discovery Today: Disease Models* (2015).
- ¹⁴¹R. Amino et al., “Quantitative imaging of Plasmodium transmission from mosquito to mammal”, *Nature Medicine* (2006).
- ¹⁴²T. Rodrigues et al., “Targeting the liver stage of malaria parasites: A yet unmet goal”, *Journal of Medicinal Chemistry* (2012).
- ¹⁴³M. Prudêncio, M. M. Mota, and A. M. Mendes, *A toolbox to study liver stage malaria*, 2011.
- ¹⁴⁴A. F. Cowman and B. S. Crabb, “Invasion of red blood cells by malaria parasites”, *Cell* **124**, 755–766 (2006).
- ¹⁴⁵A. Battista, F. Frischknecht, and U. S. Schwarz, “Geometrical model for malaria parasite migration in structured environments”, *Physical Review E - Statistical, Nonlinear, and Soft Matter Physics* (2014).
- ¹⁴⁶J. K. Hellmann et al., “Environmental constraints guide migration of malaria parasites during transmission”, *PLoS Pathogens* (2011).
- ¹⁴⁷M. J. Muthinja et al., “Microstructured Blood Vessel Surrogates Reveal Structural Tropism of Motile Malaria Parasites”, *Advanced Healthcare Materials* (2017).
- ¹⁴⁸K. Keren et al., “Mechanism of shape determination in motile cells”, *Nature* (2008).
- ¹⁴⁹M. Dembo and Y. L. Wang, “Stresses at the cell-to-substrate interface during locomotion of fibroblasts”, *Biophysical Journal* (1999).
- ¹⁵⁰H. Caraballo and K. King, “Emergency department management of mosquito-borne illness: malaria, dengue, and West Nile virus.”, *Emergency medicine practice* **16**, 1–23, quiz 23–4 (2014).

- ¹⁵¹A. F. Cowman, D. Berry, and J. Baum, “The cellular and molecular basis for malaria parasite invasion of the human red blood cell”, *Journal of Cell Biology* (2012).
- ¹⁵²I. Tardieux and J. Baum, *Reassessing the mechanics of parasite motility and host-cell invasion*, 2016.
- ¹⁵³S. Dasgupta et al., “Membrane-wrapping contributions to malaria parasite invasion of the human erythrocyte”, *Biophysical Journal* **107**, 43–54 (2014).
- ¹⁵⁴S. Dasgupta, T. Auth, and G. Gompper, “Shape and orientation matter for the cellular uptake of nonspherical particles”, *Nano Letters* **14**, 687–693 (2014).

Selbstständigkeitserklärung

Ich versichere, dass ich die von mir vorgelegte Dissertation selbstständig angefertigt, die benutzten Quellen und Hilfsmittel vollständig angegeben und die Stellen der Arbeit – einschließlich Tabellen, Karten und Abbildungen –, die anderen Werken im Wortlaut oder dem Sinn nach entnommen sind, in jedem Einzelfall als Entlehnung kenntlich gemacht habe; dass diese Dissertation noch keiner anderen Fakultät oder Universität zur Prüfung vorgelegen hat; dass sie – abgesehen von unten angegebenen Teilpublikationen – noch nicht veröffentlicht worden ist, sowie, dass ich eine solche Veröffentlichung vor Abschluss des Promotionsverfahrens nicht vornehmen werde. Die Bestimmungen der Promotionsordnung sind mir bekannt. Die von mir vorgelegte Dissertation ist von PD. Dr. Dmitry A. Fedosov betreut worden.

Mönchengladbach, am 4.5.2019